UNIVERSITÉ DE STRASBOURG

ÉCOLE DOCTORALE de Physique et Chimie-Physique (ED182)

Institut Charles Sadron

THÈSE présentée par :

Nava Schulmann

soutenue le : 18 **juin 2012**

pour obtenir le grade de : **Docteur de l'université de Strasbourg**

Discipline/ Spécialité : Physique

Elastic and Conformational Properties of Strictly Two-Dimensional Chains

THÈSE dirigée par :

Mr WITTMER Joachim	Directeur de Recherche, Université de Strasbourg

RAPPORTEURS :

Mr BLUMEN Alexander	Professeur, Université de Freiburg
Mr WINKLER Roland	Professeur, Université de Aachen, Julich

AUTRES MEMBRES DU JURY :

Mr MAALOUM Mounir	Président, Professeur, Université de Strasbourg
Mr CHARITAT Thierry	Professeur, Université de Strasbourg
Mme XU Hong	Professeur, Université de Lorraine/Metz

Abstract. This PhD thesis is devoted to a theoretical study of polymer and 'polymer like' systems in strictly two dimensions.

Polymer systems in reduced dimensions are of high experimental and technological interest and present theoretical challenges due to their strong non-mean-field-like behavior manifested by various non-trivial universal power law exponents. We focus on the *strictly* 2D limit where chain crossing is forbidden and study as function of density and of chain rigidity conformational and elastic properties of three system classes: flexible and semiflexible polymers at finite temperature and macroscopic athermal polymers (fibers) with imposed quenched curvature.

For flexible polymers it is shown that although dense self-avoiding polymers are segregated with Flory exponent $\nu = 1/2$, they do not behave as Gaussian chains. In particular a non-zero contact exponent $\theta_2 = 3/4$ implies a fractal perimeter dimension of $d_p = 5/4$. As a consequence and in agreement with the generalized Porod law, the intramolecular structure factor $F(q)$ reveals a non-Gaussian behavior and the demixing temperature of 2D polymer blends is expected to be reduced.

We also investigate the effects of chain rigidity on 2D polymer systems and found that universal behavior is not changed when the persistence length is not too large compared to the semidilute blob size. The nature of the nematic phase transition at higher rigidities, which is in the 2D case the subject of a long standing debate, is also briefly explored. Preliminary results seem to indicate a first order transition.

Finally, motivated by recent theoretical work on elastic moduli of fiber bundles, we study the effects of spontaneous curvature at zero temperature. We show that by playing on the disorder of the Fourier mode amplitudes of the ground state, it is possible to tune the compression modulus, in qualitative agreement with theory.

Résumé. Cette thèse de doctorat est consacrée à l'étude analytique et numérique de systèmes de polymères et de fibres à deux dimensions.

Des systèmes de polymères confinés en films ultra-minces présentent un très grand intérêt technologique et expérimentale et posent de nombreux défis théoriques en raison de leur fort comportement non-champ moyen qui se manifeste par divers exposants critiques non triviaux. Nous nous concentrons sur la limite *strictement* 2D où le croisement des chaînes est interdit et nous étudions, en fonction de la densité et de la rigidité des chaînes, les propriétés élastiques et conformationnelles de trois classes de systèmes: polymères flexibles et semiflexibles à température finie et polymères macroscopiques athermiques (fibres) à courbure spontanée imposée.

Pour les polymères flexibles, il est démontré que bien que les polymères auto-évitants denses adoptent des configurations compactes avec un exposant de Flory $\nu = 1/2$, ils ne se comportent pas comme des chaînes gaussiennes. En particulier un exposant de contact non-nul $\theta_2 = 3/4$ implique une dimension fractale de périmètre $d_p = 5/4$. Par conséquence, en accord avec la loi généralisée de Porod, le facteur de structure intramoléculaire $F(q)$ révèle un comportement non-gaussien et la température de démixion des mélanges de polymères 2D devrait être réduite.

Nous étudions également les effets de la rigidité des chaînes sur les systèmes de polymères à 2D et constatons que le comportement universel n'est pas modifié lorsque la longueur de persistance est beaucoup plus petite que la longueur de confinement. La nature de la transition de phase nématique à haute rigidité, qui est dans le cas 2D l'objet d'un débat de longue date, est également explorée. Des résultats préliminaires semblent indiquer une transition du premier ordre.

Enfin, motivés par un travail théorique récent sur les modules élastiques de faisceaux de fibres, nous étudions les effets de la courbure spontanée sur l'élasticité d'ensembles de fibres. Nous montrons que en jouant sur le désordre des amplitudes des modes de Fourier de l'état fondamental il est possible de régler le module de compression, en accord qualitatif avec la théorie.

Contents

Own Publications

- H. Meyer, **N. Schulmann**, J.E. Zabel, and J.P. Wittmer.

  The structure factor of dense two-dimensional polymer solutions.

  Computer Physics Communications, 182(9):1949 – 1953, 2011.

- J.P. Wittmer, A. Cavallo, H. Xu, J. Zabel, P. Polińska, **N. Schulmann**, H. Meyer, J. Farago, A. Johner, S.P. Obukhov, and J. Baschnagel.

  Scale-free static and dynamical correlations in melts of monodisperse and flory distributed homopolymers: A review of recent bond-fluctuation model studies.

  J. Stat. Phys., 145:1017–1126, 2011.

- J. P. Wittmer, **N. Schulmann**, P. Polińska, and J. Baschnagel.

  Note: Scale-free center-of-mass displacement correlations in polymer films without topological constraints and momentum conservation.

  J. Chem. Phys., 135:186101, 2011.

- **N. Schulmann**, H. Meyer, J.P. Wittmer, A. Johner, and J. Baschnagel.

  Interchain monomer contact probability in two-dimensional polymer solutions.

  Macromolecules, 45:1646–1651, 2012.

- **N. Schulmann**, H. Xu, H. Meyer, P. Polińska, J. Baschnagel, and J. .P. Wittmer.

  Strictly two-dimensional self-avoiding walks: Thermodynamic properties revisited.

  submitted, June 2012.

- **N. Schulmann**, H. Meyer, A. Cavallo, T. Kreer, A. Johner, J. Baschnagel, and J. .P. Wittmer.

  Strictly two-dimensional self-avoiding walks: Density crossover scaling.

  in preparation, June 2012.

Notations

General

V, S, L	volume, surface, perimeter length
d, d_s,d_p	spatial dimension, surface dimension, perimeter dimension
ν	inverse fractal dimension
ρ	monomer density

Thermodynamics

T	temperature .
P	pressure
e, e_{int}	energie, interchain interaction energy per monomer
K	compression modulus
B	bending rigidity
g_T	dimensionless compressibility ($\sim$ monomers per blob) $\quad g_T = k_{\mathrm{B}}T\rho/K$

Polymers

N	monomers per chain
$\vec{R_e}$	end-to-end vector
R_g	radius of gyration
b	effective bond length
ℓ_p	persistence length
ξ	blob size

Computational symbols

ε, k_{b},k_θ	energy parameteres for LJ, bonding and angular potentials.
n_{mon}	total number of monomers in simulation box.
L_{box}	box length

In this thesis k_{B} is set to unity and we use Lennard-Jones units for representing our computational results.

Chapter 1

Introduction

1.1 Technological and experimental interest.

Polymer scientists have been exposed to the challenge of understanding polymer interfaces and polymers at interfaces from the very beginning of polymer science.[1] Indeed, plastics and polymer solutions are often exposed to, or used at, solid, liquid or air interfaces. Such exposure induces noticeable changes in material or solution behavior and the high affinity of polymers to solid interfaces, the relatively low perturbation of the air-water interfacial tension[2] or the intricate questions associated with the reduction of polymer flow in sintered capillaries[3] due to polymer adsorption, have been discussed from earlier times. Importantly, scientific questions related to polymers and interfaces have often emerged from the different fields where polymer technological applications developed.

Plastic surfaces and surfaces exposed to or coated by polymer solutions or polymer dense films are of great relevance in the polymer industry.[4–7] Thin films of polymers are used as adhesives, as a protection against corrosion and as lubricants to name only a few. Polymers can also be found in different applications at the liquid-air, the liquid-liquid or the liquid-solid interfaces where they play, amongst others, an important role as stabilizers for droplets in emulsions, for suspensions of colloidal particles or in liposomal stealth technology.[8] Additionally, challenges in the plastic industry such as those posed by plastic coloring or gloss preservation are related to the properties of solid polymer surfaces. In the biological realm, polymers play a key role at the membranes interfaces by preventing for instance bio-recognition phenomena from non-specific adhesion.[9]

The scientific and technological importance of this field has lead to its impressive development over the last decades. The conjugated effort of experiments, numerical simulations and theory resulted in a comprehensive understanding of many aspects of polymers at interfaces. However, the recent trends in the nanosciences have pushed polymer confinement and polymer-surface interactions to new levels of reduced dimensionality.[10] In many situations the polymers are effectively in a two-dimensional geometry, where the width of the polymer layer is much smaller than the bulk polymer size or even comparable to the monomer dimension. In such geometries, scarcely addressed in the polymer adsorption and polymer confinement literature, a number of new questions arise, related for instance to the non-crossability of strictly two dimensional chains.[11]

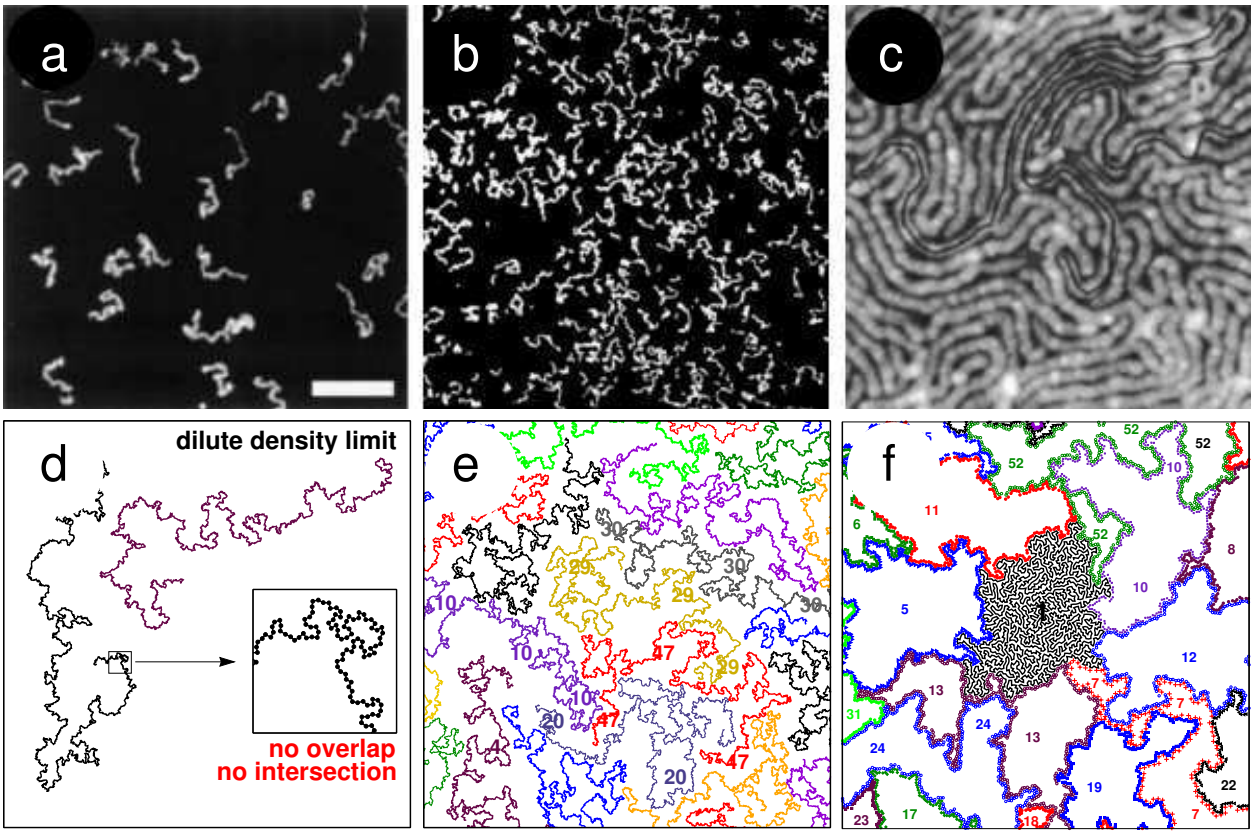

Figure 1.1: Experimental images (a-c) and numerical simulation snapshots (d-f) of 2D polymer chains, from the dilute regime in the left to the dense regime on the right. a) and b) Conformations of strongly adsorbed DNAs imaged by optical fluorescence.[12] c) AFM images of cross-linked wormlike micelles of diblock copolymers.[13] d) to f) Our simulation results on strictly 2D flexible chains by MD simulations with a bead-spring model. The non-overlapping, non-intersecting swollen polymer conformations can be seen in d). The numbers in e) and f) refer to a chain index used for computational purposes. Some chains are still rather elongated (e.g., chain 10 or 30) and the swollen chain statistics remains relevant on small scales. On larger scales the chains adopt (on average) compact configurations with power-law exponents $\nu = 1/d$ and $\theta_2 = 3/4$ as discussed in details in Chap. 3. The chain segregation and the fractal nature of the chain perimeter in the melt is well revealed in panel f). Only "chain 1" in the middle is fully drawn while for the other chains only the perimeter monomers interacting with other chains are indicated.

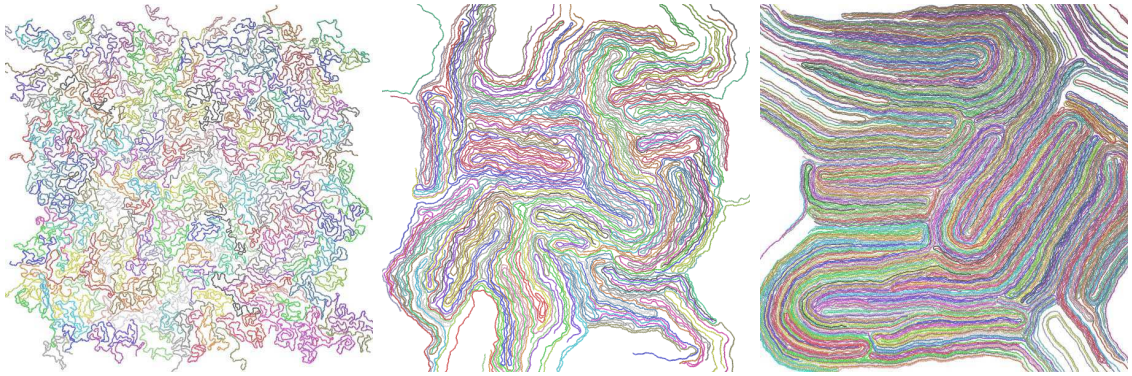

Figure 1.2: Snapshots of 2D semiflexible polymer systems from our simulations discussed in Chap. 4. Both density and rigidity increase from left to right. Hairpins in dense configuration slow down the equilibration dynamics and lead to strong hysteresis effects during the isotropic-nematic transition.

On the experimental side, recent efforts have provided new information on the static and dynamic properties of ultra-confined chains.[14–23] By the end of last century, Shuto and co-workers[24,25] have reported measurements of chain conformation in thin polystyrene films by stacking multiple films on a single planar substrate by a Langmuir-Blodgett film deposition technique. Using small angle neutron and x-ray scattering, they found that the radius of gyration increased significantly along the direction parallel to the surface when the film thickness becomes much smaller than the polymer Flory radius. Shortly after, Maier and Rädler[12] investigated the conformations and self diffusion of single DNA molecules electrostatically bounded to lipid bilayers using fluorescence microscopy – see Fig. 1.1a and 1.1b. They showed that the power law scaling of the lateral chain extension agrees with predictions for self-avoiding walks in two dimensions, and that the center-of-mass diffusion follows Rouse dynamics.

Thermodynamic properties of the 2D polymer layers have also been studied in conjunction with individual chain conformations. Gavranovic *et al*[21] studied Langmuir monolayers of Poly(tert-butyl methacrylate) at the air-water interface. At low surface densities, the behavior of the lateral pressure and of the surface viscosity suggests that the chains behave as non interacting collapsed disks, while higher pressure eventually saturates the surfaces driving into a multilayer state.

When the bending rigidity is large, as for instance for thick self-assembled polymers, the chains display a finite semiflexibility, an intrinsic parameter which role has not yet been fully elucidated for strictly two-dimensional systems. During the last decade, Wang and Foltz[13] studied strictly 2D nanoropes obtained by crosslinking micelles of copolymer diblocks – see Fig. 1.1c. Surprisingly, they observed that the chain conformations studied by atomic force microscopy obey Gaussian statistics in the 2D dispersed state and that in the dense state chains are strongly interpenetrated. The parameter space separating semi-flexible polymers from fully rigid 2D systems remains largely unexplored. In this limit of very stiff molecules, one recovers the typical phenomenology of phase transitions for rod-like molecules, albeit with 2D specificities.[26]

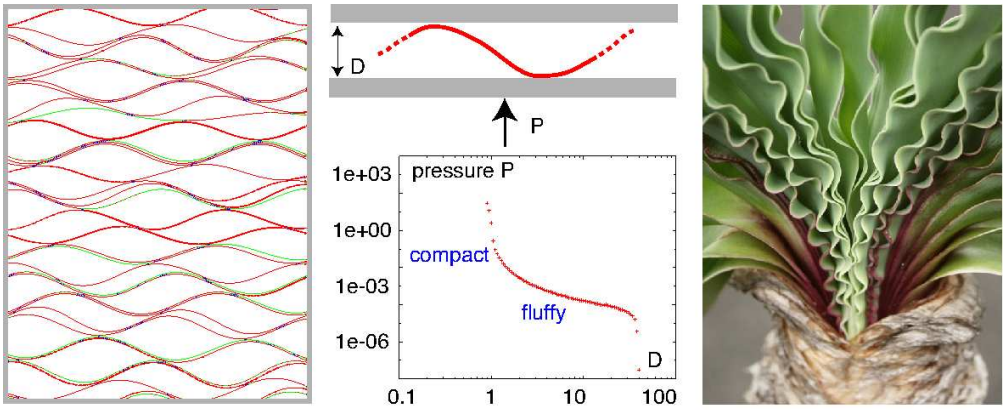

Figure 1.3: A 2D stack of fibers with finite spontaneous curvatures resists to compression under a normal force. Each fiber is on average confined within a distance D. The constitutive pressure curve, as D is reduced from a contact value to maximum compression at $D = 0$, is a function of the nature of the disorder associated with the spontaneous curvature distribution.

Questions intimately related to the organization and ordering of semi-flexible or rigid chains also arise in athermal granular media. For long straight macroscopic rods, Philipse[27] has for instance studied packings of needles, matches or toothpicks and showed that the experimentally observed laws for random packing volume fractions can be understood from a simple hypothesis about uncorrelated rod orientations. In quasi two-dimensional containers, Galanis and collaborators[28] investigated the organization of vibrated anisotropic granular media. Vibration acts to create a random velocity distribution of the rods to which can be associated an effective temperature. This experimental system allows thus to explore a "temperature"-density phase space and to observe phenomena reminiscent of two-dimensional thermal behavior. Interestingly, the concept of effective temperature arises also in macroscopic static fiber systems with non-straight shapes. In this emerging field,[29] the degree of disorder introduced by the random distribution of spontaneous fiber curvatures reduces the fiber stack density and allows for a finite bundle compressibility, as recently evidenced in studies of the ponytails,[30] and as first suggested by Beckrich *et al.*[31]

In the experiments discussed above, the conformational and thermodynamic properties of two-dimensional polymer systems, as well as the added effects of chain stiffness and spontaneous shape reveal a growing area of polymer science where many questions still remain to be addressed. In the next paragraph we review the current theoretical understanding of such systems.

1.2 Summary of relevant theoretical work.

It is well known[32] that the phase behavior and the measurable properties of strongly confined systems may drastically differ from those observed in the bulk. In the case of dense polymers, where the bulk properties can be well described by mean-field theories,[33] the strong reduction of one of the space dimensions leads to a significant decrease of the number of interchain interactions and, consequently, to logarithmic corrections to the mean-field behavior. For extreme confinements, polymers live effectively in two dimensions. In this limit two principal theoretical classes of polymer systems may be considered: i) strictly 2D "self-avoiding walks" (SAW) where chains do not cross and ii) partially "self-avoiding trails" (SAT) where chains can cross each other with minimal vertical displacement and energy penalty. Semenov and Johner[11] have theoretically shown that these two classes should exhibit very different static and dynamical behavior.

The strictly 2D dilute limit was first considered theoretically by Flory,[34] who predicted that the exponent ν that describes the growth of polymer dimensions with polymer mass and determines the thermodynamic properties of the polymer solutions, is significantly larger for single self-avoiding polymers in 2D than in 3D ($\nu_{2D} = 3/4, \nu_{3D} = 5/3$). For strictly 2D melts, de Gennes[35] proposed that chains segregate while displaying an exponent ν similar to that of polymers in 3D melts, $\nu = 1/2$. Using conformal map transformations, Duplantier[36,37] further investigated the conformations of strictly 2D chains, and predicted the critical exponents associated with polymer conformation and thermodynamics in the dilute and in the dense regimes.

Many polymers display a finite bending rigidity which considerably modifies the behavior of dilute and dense chain systems in two or three dimensions. For single macromolecules, changes in conformation are theoretically accounted for by introducing the persistence length ℓ_p, the distance over which tangent-tangent correlations decay. The semiflexible chain can thus be seen as a sequence of uncorrelated segments of length ℓ_p, its global behavior being well described by flexible chain models with a renormalized monomer length.[35] It is important to note that in three-dimensions the chain stiffness reduces considerably the probability of intrachain interactions at short distances, excluded volume effects are only displayed by long enough chains.[38,39] In two-dimensions, however, self-avoidance effects are much stronger resulting in full swollen chains for all polymer lengths. If the persistence length largely exceeds the blob size, one expects with increasing persistence length and density to observe a transition to an ordered nematic state. The nature of this transition, well established in the bulk case is a matter of a long standing debate for 2D systems.[40–42]

The coupling between chain shape disorder, packing and conformation arises also in granular-like fiber systems as discussed above. Here, statistical thermodynamics, that describes the effect of thermal disorder, does not strictly apply. Instead, new statistical mechanics approaches need to be developed. Within this context, Beckrich *et al*[31] pointed to a useful formal analogy between two-dimensional stacks of macroscopic fibers with non-zero spontaneous curvature and the related thermal systems of smectic chains and membranes. The analogy allows to compute experimentally relevant quantities as a function of the parameters that describe the distribution of the fiber spontaneous shapes. For instance, these authors computed the compression modulus of the fiber stack that determines the ponytail[30] or rope cone shapes.[31]

1.3 Summary of previous numerical work.

Monte Carlo (MC), Molecular Dynamics (MD) and other numerical methods are well-established tools for understanding the static and dynamic properties of polymer chains.[32,43,44] An extensive literature has been devoted to settle key questions in polymer science, pertaining either to dilute or dense systems. For single (dilute) polymers, accurate predictions now exist for quantities such as the exponents associated with the dependence of chain size with polymerization index, both in two and three dimensions, for flexible or semiflexible chains with or without excluded volume interactions. For dense polymer systems numerical simulations are more demanding, and the current push to new and more accurate simulations has been driven by the need of equilibrated systems large enough to capture experimentally relevant behavior or to eventually settle important theoretical questions.[45–49]

The question of the typical conformation of polymer chains in the two dimensional melt has been dealt with by numerical simulations over the last three decades. Bäumgartner[50] has measured the end-to-end

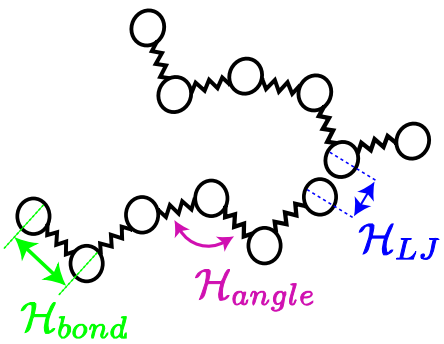

Figure 1.4: Schematic representation of the interactions accounted for by our numerical simulation model. $\mathcal{H}_{LJ}$ represents the Lennard-Jones repulsive interaction between non-neighboring monomers, $\mathcal{H}_{bond}$ is the connectivity potential between two adjacent monomers and $\mathcal{H}_{angle}$ is the angular potential that penalizes bending modes and encodes the ground-state shape.

distance and the radius of gyration of chains simulated by MC methods. He found that the chains strongly segregate and follow a Gaussian-like behavior with $\nu_{2D} = 1/2$ as predicted by de-Gennes. A few years later Carmesin and Kremer[51] obtained similar results using the Bond-Fluctuation Model (BFM), a lattice MC algorithm for linear connected chains. Contrary to these authors, Ostrovsky *et al*[52] and Yethiraj,[53] using respectively different MC algorithms, reported that polymer chains in the melt do not completely segregate and show significant interpenetration. Recent studies by Meyer *et al*[54] using MD simulations of a bead-spring model, have revisited this problem and provided an extensive description for many of the conformational properties of 2D polymer melts, that we will further discuss in Chap. 3. The behavior of thin polymer films of finite width was also discussed recently by Cavallo and co-workers.[55] It was shown that, in contrast to Flory's and Silberberg's hypotheses and in agreement with Semenov and Johner,[11] ultra-thin films where the thickness H is smaller than the excluded volume screening length exhibit logarithmic deviations from Gaussian predictions.

Semiflexibility adds an extra burden to the computing facilities, due to the very long relaxation times of dense semiflexible systems. The nature of the 2D isotropic-nematic transition in dense semiflexible polymer solutions and melts, for instance, has not yet been completely established. Baumgärtner[56] and others[57,58] simulated semiflexible polymers on square lattices. In contrast to theoretical predictions, they did not find a phase transition between an isotropic and a long-range, orientationally ordered state, only transitions to ordered domains being observed. Dijkstra and Frenkel[26] proposed that these controversial results stem from the lattice structure of the previously simulated systems. Using an off-lattice model consisting of infinitesimally thin hard segments connected by joints of variable flexibility they did observe a Kosterlitz-Thouless type transition from the isotropic phase to a 'nematic' phase with quasi-long-range orientational order.[32]

1.4 Our approach & main results

As we have seen above, semiflexibility, chain spontaneous shape, excluded volume and density play a role in two-dimensional polymer systems that is neither fully explored in experiments and in numerical simulations, nor completely understood from a theoretical perspective.

Pursuing extensive numerical work[45–49] carried out in the ICS Theory and Simulation Group, we aim at systematically characterizing the density crossover scaling of various thermodynamic and conformational properties of flexible polymers in strictly two dimensions. Using the same computational tools, we also investigate the effects of small persistence lengths on chain conformations in dilute solutions where local stiffness is predicted to change prefactors only,[59] and study the isotropic-nematic transition at higher densities and rigidities. Finally, motivated by recent theoretical work[31] of the ICS Membrane and Microforces Group, we investigate the effects of non-zero spontaneous curvature on athermal chain bundles (fibers).

Being interested by universal power-law scaling and focusing on the limit of long chains, where the specific physics and chemistry at the monomer level is non-relevant, we use a generic coarse-grained bead-spring model[60,61] which is simple enough for efficiently simulate dense large-chain systems. Interactions

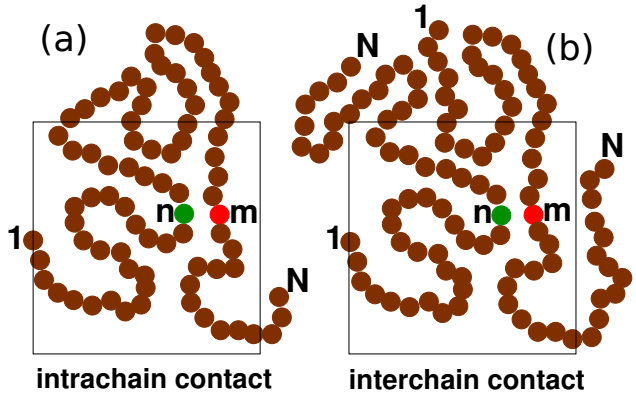

Figure 1.5: Key scaling argument relating the intrachain size distribution $G_2(r, s \approx N)$ to the interchain pair distribution function $g_{\rm int}(r)$. It states that it is irrelevant of whether the compactly filled neighborhood at $r \ll R$ around the reference monomer n is penetrated by a long loop of the same chain as in panel (a) or by another chain with a center of mass at a typical distance R as shown in panel (b).

between beads are modeled by an effective Hamiltonian containing three terms:

$$\mathcal{H} = \mathcal{H}_{LJ} + \mathcal{H}_{bond} + \mathcal{H}_{angle} \tag{1.1}$$

with $\mathcal{H}_{LJ} = 4\epsilon\left[(\sigma/r)^{12} - (\sigma/r)^{6}\right] + \epsilon$ for $r/\sigma \leq 2^{1/6}$ the (truncated and shifted) Lennard-Jones (LJ) potential[44] representing the repulsive interaction between non-neighboring monomers. $\mathcal{H}_{bond} = k_b(r - r_0)^2$ is the connectivity potential between two adjacent monomers and $\mathcal{H}_{angle} = k_\theta(\theta - \theta_0)^2$ is the angular potential that penalizes bending modes and encodes the ground-state shape.

By exploring the parameters space of this general model, we simulated three main classes of strictly two-dimensional chain systems: i) flexible polymers, ii) semiflexible polymers and iii) athermal polymers or macroscopic fibers. The two first thermalized classes were sampled using standard Molecular Dynamics (MD).[62] The third class of athermal chains was simulated by energy minimization methods.[63]

Flexible polymers. The first class of chain systems, obtained by omitting the angular term in the general Hamiltonian, allows to investigate the impact of the non-crossability constraint on strictly 2D polymer conformations. In this case, fully discussed in Chap. 3, the only free parameters at fixed temperature are chain length and chain density.

In the limit of asymptotically long chains, a swollen typical conformation is progressively transformed into a compact one, as the density increases from the dilute regime to the melt, an evolution illustrated by the simulation snapshots d-f in Fig. 1.1. In the intermediate semi-dilute regime, chains can be seen as a compact packing of blobs with g monomers, g decreasing as the density is incremented. We found that the chain size scales with the reduced chain length N/g as predicted theoretically by classical density crossover scaling *à la* de Gennes.[34,35]

More importantly, our simulations reveal the central role of the contact exponent θ_2 in determining the chain conformations in strictly 2D polymer systems. The values of θ_2 extracted from our simulations agree very well with Duplantier's theoretical predictions for the dilute and the melt limits.[36,37] θ_2, defined as the power-law exponent of the subchains size distribution, was also shown[11] to be related to the fractal dimension of the chains perimeter (The theoretical argument given by Semenov and Johner is sketched in Fig. 1.5). This fractal character can be hinted from Figs. 1.1c and 1.1f, where the segregated polymers clearly exhibit a non disk-like shape. The fractal nature of the chains perimeter can be shown to determine two experimentally relevant properties: i) the form factor $F(q)$ in the intermediate wave-vector regime, which can be probed by scattering experiments, clearly displays a non-Gaussian behavior and ii) the probability for interchain monomer-monomer contact is reduced with respect to its 3D counterpart, which is expected to lead to improved mixing of polymers blends in 2D.

Semiflexible polymers. In Chap. 4 we present our results for the second class of systems, namely semiflexible polymers, simulated by considering the full Hamiltonian Eq. 1.1, with vanishing spontaneous angles θ_0 corresponding to chains with straight ground-state shapes.

We investigate the stiffness effects on systems of semiflexible chains with polymerization index ranging up to $N = 1024$. For these chains, much longer than those probed in previous numerical work,[26,56,58,64] we found that scaling observed for fully flexible chains holds as long as the persistence length remains smaller then the blob size.[59] The equilibration dynamics at higher rigidities slows down rapidly, introducing strong hysteresis effects as can be seen when different dynamical pathways are compared. The precise characterization of the order and the location of the isotropic-nematic phase transition is thus difficult to be obtained. Preliminary results, however, point to a first order transition.

Athermal fibers. Finally, by imposing a given distribution of θ_0 values, we force finite spontaneous curvature in our coarse-grained polymer Hamiltonian of Eq. (1.1), and study its effect on the mechanical properties and on the conformations of macroscopic fiber stacks.

We report in Chap. 5 simulations of several fiber systems with different imposed quenched curvatures, ranging from Gaussian distributed wavelengths at fixed amplitude to q-dependent amplitudes. We show that the compressibility of the fiber bundles strongly depend on the degree of disorder of the ground state of the individual fibers. We compare our results to recent theoretical work on the elastic moduli of fiber bundles,[31] and show that they can be qualitatively understood by the statistical physics concepts developed in the context of thermal polymers and membranes.

Chapter 2

Concepts and methods

Having introduced the motivations and the general context of our work in the previous chapter, we discuss here the principal concepts and methods used to obtain our later results. We first review in details our simulation coarsed-grained model and present the numerical methods that allow to compute the system evolution as a function of time. We describe then how the configurations ensembles obtained by the simulations process are treated in order to extract the relevant thermodynamic and conformational quantities.

2.1 Numerical tools

Coarse-grained polymer models. Theoretical and computational model building is an important step in making scientific progress.[32,43,44] Understanding the limiting cases of pure systems of long chains, as they can currently only be realized in simulations of generic models, is a guideline for interpreting experimental work.[1,59] The aim of this work is to clarify universal power-law scaling predictions in the limit of large chain length N and low wavevector q where the specific physics and chemistry on the monomeric level (such as the local chain stiffness) is only relevant for prefactor effects.[59] This calls for the use of a generic coarse-grained polymer model Hamiltonian which is sufficiently simple to allow the efficient computation of dense large-chain systems which are consistent with the central assumptions of the theoretical studies by Duplantier[65] and Semenov and Johner:[66] the chains must be strictly 2D SAW without chain intersections.

Effective Hamiltonian used. As in previous studies of the ICS Theory and Simulation Group[45–49] our numerical results are obtained by molecular dynamics simulations of monodisperse, linear and highly flexible chains using (essentially) the well-known Kremer-Grest bead-spring model which has been successfully used for a broad range of polymer physics problems.[60,61,67] The non-bonded excluded volume interactions between the effective monomers are represented by a purely repulsive (truncated and shifted) Lennard-Jones (LJ) potential[44]

$$u_{\rm nb}(r) = 4\epsilon\left[(\sigma/r)^{12} - (\sigma/r)^{6}\right] + \epsilon \quad \text{for } r/\sigma \leq 2^{1/6} \tag{2.1}$$

and $u_{\rm nb}(r) = 0$ elsewhere. The Lennard-Jones potential does *not* act between adjacent monomers of a chain which are topologically connected by a simple harmonic spring potential

$$u_{\rm b}(r) = \frac{1}{2}k_{\rm b}(r - l_{\rm b})^2 \tag{2.2}$$

with a (rather strong) spring constant $k_{\rm b} = 676\epsilon$ and a bond reference length $l_{\rm b} = 0.967\sigma$. Both constants $k_{\rm b}$ and $l_{\rm b}$ have been calibrated to the "finite extendible nonlinear elastic" (FENE) springs of the original KG model.[60] Semiflexibility is included in our modelling approach by adding a stiffness potential

$$u_{\theta}(r) = k_{\theta}(\theta - \theta_0)^2 \tag{2.3}$$

with θ being the angle between adjacent bonds and θ_0 the equilibrium angle in the ground state configuration. The monomer mass m, the temperature T and Boltzmann's constant $k_{\rm B}$ are all set to unity, i.e. $\beta \equiv 1/k_{\rm B}T = 1$ for the inverse temperature, and Lennard-Jones units ($\epsilon = \sigma = m = 1$) are used throughout this PhD report. The parameters of the model Hamiltonian make monomer overlap and chain intersections impossible, as can be seen from the snapshots of chains presented in Fig. 2.1. (We have explicitly checked that such a violation never occurs.) We simulate thus strictly 2D self-avoiding walks as required.

Sampling of configurations. Taking advantage of the public domain LAMMPS implementation (Version 21May2008)[67] the presented results for the flexible and semiflexible polymer systems (Chap. 3 and 4, have been obtained by sampling the classical equations of motion by MD simulation using the Velocity-Verlet algorithm with a time increment $\delta t = 0.01$. The constant (mean) temperature $T = 1$ was imposed by means of a Langevin thermostat with a friction constant $\gamma = 0.5$.[43,44] Note that the strong harmonic bonding potential (used to avoid chain intersections) corresponds to a tiny oscillation time $\tau_{\rm b} = 2\pi\sqrt{m/k} \approx 0.2$. Unfortunately, this is only about a factor 10 larger then our standard time increment δt. Obviously, this begs the question of whether configurations with the correct statistical weight have been sampled. In order to crosscheck our results we have in addition performed MC simulations which (by construction) obey detailed balance,[68] i.e. produce configuration ensemble with correct weights. The comparison of ensembles generated with both methods shows that all configurational properties are (within the error bars) essentially identical. The only difference is that at lower densities ($\rho < 0.25$) the MD method yields mean bond lengths which are slightly too large for $\delta t = 0.01$. While this effect is irrelevant for the configurational properties, it matters for the pressure P as further discussed in Sec. 3.2.2.

The results for the systems of athermal chains, in which energy rather than free-energy needs to be minimized, were obtained by the standard quasi-static steepest-descent method.[63] This energy minimisation method consists of iteratively adjusting the monomer coordinates by moving along the direction of the total force. The process is stopped if the energy difference between two succesive configurations is smaller then $\varepsilon_e = 10^{-8}$ or if the norm of the global force vector is less than $\varepsilon_f = 10^{-8}$ or if the number of iterations is greater then 10^7.

Parameter range. Some thermodynamic and conformational properties for flexible chains discussed below are summarized in Table 2.1. While most of previous studies of the ICS Theory and Simulation Group[45–47] have focused on one melt density, $\rho = 0.875$, we scanned over a broad range of densities ρ. Note that our largest chain length $N = 2048$ is about an order of magnitude larger than in previous computational studies of dense 2D polymers: $N = 59$ by Baumgärtner in 1982,[50] $N = 100$ by Carmesin and Kremer in their seminal work in 1990,[51] $N = 100$ by Nelson *et al.* in 1997,[69] $N = 32$ by Polanowski and Pakula in 2002,[70] $N = 60$ by Balabaev *et al.* in 2002,[71] $N = 256$ by Yethiraj in 2003[72] and $N = 256$ by Cavallo *et al.* in 2005.[73,74] To avoid finite system size effects the periodic simulation boxes contain at least $M = 96$ chains for the higher densities, e.g. for $N = 2048$ and $\rho = 0.875$ we have 196608 monomers in a box of linear length $L_{\rm box} \approx 474$ and for $N = 1024$ and $\rho = 0.03125$ we have 98304 monomers in a box of $L_{\rm box} \approx 1774$. Even more chains are sampled for shorter chains.

2.2 Some thermodynamic and mechanical properties of polymer systems

We discuss briefly in this paragraph how various ensemble average properties have been computed.

Energy. The total mean interaction energy per monomer $e_{\rm tot}$, discussed in Sec. 3.2.1 is directly calculated for each configuration from the BSM Hamiltonian $\mathcal{H} = \mathcal{H}_{LJ} + \mathcal{H}_{bond} + \mathcal{H}_{ang}$ described in Sec. 1.

Pressure. The isotropic pressure at a given density ρ for systems without periodic boundary conditions can be obtained using

ρ	M	$e_{\rm nb}$	$e_{\rm int}$	P	$g_{\rm T,N}$	l	$R_{\rm e}$	$\left(\frac{R_{\rm e}}{R_{\rm g}}\right)^2$	Δ_2	$n_{\rm int}$	$g_{\rm T}$	ξ	$b_{\rm N}$
0	1	1.6E-02	-	0	1024	0.970	179	7.1	0.62	0	∞	∞	∞
1/128	24	1.6E-02	2.5E-07	6.1E-06	811*	0.970	179	7.1	0.62	1.5E-05	3900*	1955*	13*
1/64	48	1.6E-02	9.6E-07	1.4E-05	500*	0.970	177	6.8	0.61	0.4E-04	975*	691*	9.1*
1/32	96	1.6E-02	2.2E-06	7.7E-05	197*	0.970	162	6.9	0.60	1.0E-04	244*	244*	6.5*
1/16	48	1.6E-02	3.7E-06	3.4E-04	67	0.970	150	6.5	0.58	3.8E-04	67	86	4.68
0.125	48	1.8E-02	3.0E-05	2.2E-03	17	0.969	120	5.9	0.54	0.2E-02	18.1	31	3.75
0.250	96	1.8E-02	1.9E-04	2.0E-02	3.7	0.969	88	5.5	0.53	1.2E-02	3.7	11	2.74
0.375	96	2.2E-02	6.5E-04	0.081	1.38	0.969	74	5.5	0.57	4.5E-02	1.7	5.9	2.21
0.500	192	2.9E-02	0.0018	0.23	0.50	0.969	63	5.3	0.54	9.8E-02	0.50	3.8*	1.96
0.625	96	4.6E-02	0.0059	0.64	0.203	0.968	60	5.4	0.56	0.21	0.19	2.7*	1.89
0.750	96	8.4E-02	0.0105	1.61	0.083	0.966	51	5.3	0.50	0.35	0.083	2.0*	1.61
0.875	96	1.8E-01	0.0261	4.74	0.032	0.963	48	5.3	0.48	0.51	0.032	1.6*	1.51

Table 2.1: Various properties as a function of monomer density ρ for flexible chains. The columns 2 - 11 refer to chains of length $N = 1024$: the number of chains per box M, the total non-bonded interaction energy $e_{\rm nb}$ per monomer, the interaction energy $e_{\rm int}$ per monomer between monomers of different chains (Sec. 3.2.1), the pressure P (Sec. 3.2.2), the dimensionless compressibility $g_{\rm T,N} = k_{\rm B}T\rho/K$ discussed in Sec. 3.2.3, the root-mean-squared bond length l, the root-mean-squared chain end-to-end distance $R_{\rm e}$ (Sec. 3.3.1), the ratio $(R_{\rm e}/R_{\rm g})^2$ discussed in Sec. 3.3.2, the aspherity moment Δ_2 obtained from the eigenvalues of the inertia tensor (Sec. 3.3.4) and the fraction of interchain monomer contacts $n_{\rm int}$ for a cut-off parameter $a = 1.56$. The bonding potential being very stiff, the bond length l is found to depend very little on density. The last three columns summarize results for asymptotically long chains in the compact chain limit: the dimensionless excess compressibility $g_{\rm T} \equiv \lim_{N\to\infty} g_{\rm T,N}$, the blob size ξ characterizing the density fluctuations obtained assuming Eq. (3.16) to hold for all densities and the effective segment size $b_{\rm N} \equiv \lim_{N\to\infty} R_{\rm e}(N)/N^{1/d}$ where we have used that for the smallest densities $b_{\rm N} \approx 1.41/\rho^{1/2}$ holds (Fig. 3.6). Extrapolated values are indicated by stars ($\star$).

$$P = \frac{1}{V}\left[N_t k_{\rm B}T + \sum_i^{N_t} r_i \bullet f_i\right]. \tag{2.4}$$

where V stands for the d-dimensional volume, i.e. the surface $L_{\rm box}^2$ of our periodic simulation boxes, N_t is the total number of atoms in the system, r_i is the absolute position of the monomer i in space and f_i the total force acting on the monomer i. This form is of course not convenient for periodic boundary conditions where the virial equation $P = k_{\rm B}T\rho + \langle \mathcal{W} \rangle / V$ with relative particles distances r_{ij} and interaction forces f_{ij} between particles i and j should be used.[43] For pairwise additive interactions, as is the case for our flexible chain systems, the pair virial function $\mathcal{W}$ is associated to the bonded and/or to the non-bonded pair potential $u(r)$:

$$\mathcal{W} = -\frac{1}{d}\sum_{i<j} w(r_{ij}) \text{ with } w(r) = r\frac{{\rm d}u(r)}{{\rm d}r} \tag{2.5}$$

The density crossover scaling for our flexible systems is presented in figure Fig. 3.4 of Sec. 3.2.2. It can be shown that in the case of semiflexible and rigid chains where the stiffness adds a three-body angular potential Eq. 2.5 still holds.[75]

For anisotropic systems such as the pre-aligned rigid chains discussed in Chap. 5, the different components of the stress tensor $\sigma_{\alpha\beta}$, with $\alpha, \beta = x, y, z$, were computed by[76]

$$\langle \hat{\sigma}_{\alpha\beta} \rangle = \left\langle \frac{1}{V}\left[\sum_{i<j}\left(\frac{\partial U}{\partial r_{ij}}\right)\frac{r_{ij}^\alpha r_{ij}^\beta}{r_{ij}} - \sum_{i=1}^{M} m_i v_i^\alpha v_i^\beta\right]\right\rangle \tag{2.6}$$

Here m_i and v_i^α are respectively the mass and the α velocity component of monomer i.

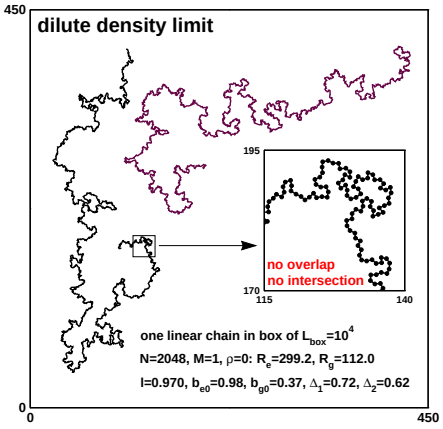

Figure 2.1: Snapshots of two chains of length $N = 2048$. As expected from theory,[59] the chains are shown to reveal swollen chain statistics with power-law exponents $\nu = \nu_0 \equiv 3/4$ and $\theta_2 = \theta_{2,0} \equiv 19/12$. Dilute chains are rather elongated as also seen from the given asphericity parameters Δ_i further discussed in Sec. 3.3.4. Inset: Short subchain showing that the monomers do not (or only barely) overlap and that the chains do not intersect.

Compression modulus. Being an isotropic liquid the polymer solution is described by only one elastic modulus, the bulk compression modulus

$$K \equiv 1/\kappa_{\mathrm{T}} = \rho \frac{\partial P}{\partial \rho}, \tag{2.7}$$

with κ_{T} being the standard isothermal compressibility.[77] The bulk modulus and/or the dimensionless compressibility can be directly obtained numerically by fitting the pressure isotherms discussed in the previous subsection. This is best done by fitting a spline to $y \equiv \log(\beta P)$ as a function of $x \equiv \log(\rho)$. Alternatively, the compression modulus for a given density can be directly computed using the Rowlinson formula[78] or from the plateau of the structure factor in the low-q limit.[32,33] These two methods will be discussed in details in Sec. 3.2.3.

2.3 Conformational properties of polymer chains

2.3.1 Real space properties

Unlike global properties such as the pressure or the compression modulus discussed above, conformational properties are primarily defined through the particles microscopic positions. The conformational characterization of a system is thus directly obtained by time averaging of the per-configuration values computed by applying the conformational properties definitions. We review here the definitions of several conformational properties related to chains typical size and shape. These definition were used to obtain the results discussed in Sec. 3.3.

Chain size. The end-to-end vector R_e is the simplest measure for the chains typical size. It is the vector that points from one end of a polymer to the other end.

$$R_e \equiv r_N - r_1 \tag{2.8}$$

where r_1 and r_N are the position vectors of the first and the last monomers of the chain. The norm of the end-to-end vector is called the end-to-end distance.

The radius of gyration R_g measures the size of an object taking into account the position of all its particles. It is calculated as the root mean square distance of the objects' parts from its center of mass. For a N monomer chain with its center of mass at r_{cm}

$$R_g^2 \equiv \frac{1}{N} \sum_{i=1}^{N} (r_i - r_{cm})^2 \tag{2.9}$$

The dependence of the chains typical size on the chain length N is caracterized by a power law exponent ν often called "Flory's exponent"

$$R \sim N^{\nu}. \tag{2.10}$$

This exponent, being equal to the inverse fractal dimension, plays a crucial role in determining various conformational and thermodynamic properties of the polymer systems.

The calculation of the values of R_e and R_g can be applied not only over the entire chains but also over 'chain segments' or 'subchains' containing $s = m - n + 1$ monomers. Quite generally the radius of gyration $R_{\rm g}(s)$ of a subchain of arc-length $s \leq N$ is given by[79]

$$R_{\rm g}^2(s) = \frac{1}{s^2} \int_0^s ds' \ (s - s') \times R_{\rm e}^2(s') \tag{2.11}$$

if the mean-squared subchain size $R_{\rm e}^2(s')$ is known. Let us assume that $R_{\rm e}(s') = b_{\rm e} s'^{\nu}$ holds rigorously for all $s' \leq s$. This implies

$$(R_{\rm e}(s)/R_{\rm g}(s))^2 = (2\nu + 1)(2\nu + 2), \tag{2.12}$$

i.e. the ratio is set alone by the inverse fractal dimension ν and not by the spatial dimension d or the local monomer properties. A ratio 6 must thus be observed if $\nu = 1/2$ holds rigorously, a ratio $35/4 = 8.75$ for $\nu = 3/4$. Please note that corrections to the assumed power-law behavior at the *lower* integration cut-off should not alter these values if s is sufficiently large.

In addition to the averaged values of R_e and R_g it is of interest to characterize the probability distribution $G_i(r, s)$ of the intrachain vectors $\underline{r} = \underline{r}_m - \underline{r}_n$ between the monomers n and $m = n + s - 1$. The power law exponents θ_0, θ_1 and θ_2 describing the small-x limit of these distibutions are known as the 'contact exponents'. These exponents play an important role in determining both intrachain and interchain properties of two-dimensional chains and will be discussed in details in Chap. 3.

Angular correlations. The chain configuration may further be characterized by means of intrachain angular correlations. The first Legendre polynomial $P_1(s) \equiv \langle \underline{e}_n \cdot \underline{e}_m \rangle$ with $\underline{e}_i$ denoting the normalized tangent bond vector connecting the monomers i and $i + 1$ of a chain has been shown to be of particular interest for characterizing the deviations from Gaussianity in dense 3D polymer solutions.[33] (The average is taken as before over all possible pairs of monomers n and $m = n + s - 1$.) The reason for this is that[33]

$$P_1(s) \sim -\frac{\partial^2 R_{\rm e}^2(s)}{\partial s^2} \tag{2.13}$$

and that thus small deviations from the asymptotic exponent $2\nu = 1$ are emphasized. The second Legendre polynomial $P_2 \equiv \langle (\underline{e}_n \cdot \underline{e}_m)^2 \rangle - 1/2$ probes essentially the return probability $p_{\rm r}(s)$ of the chain after s curvilinear steps, as will be explained in detail in Sec. 3.3.

Chain shape. The gyration tensor $\underline{\underline{M}}$ may be defined as

$$M_{\alpha\beta} = \frac{1}{N} \sum_{n=1}^{N} (r_{n,\alpha} - R_{{\rm cm},\alpha})(r_{n,\beta} - R_{{\rm cm},\beta}) \tag{2.14}$$

with $R_{{\rm cm},\alpha}$ being the α-component of the chains's center of mass. We remind that the radius of gyration $R_{\rm g}^2$ is given by the trace ${\rm tr}(\underline{\underline{M}}) = M_{xx} + M_{yy} = \lambda_1 + \lambda_2$ (averaged over all chains) with eigenvalues λ_1 and λ_2 obtained from

$$\lambda_{1,2} = \frac{1}{2} \left({\rm tr}(\underline{\underline{M}}) \pm \sqrt{{\rm tr}(\underline{\underline{M}})^2 - 4{\rm det}(\underline{\underline{M}})} \right). \tag{2.15}$$

Similary one may define the gyration tensor and corresponding eigenvalues for subchains.[46] The chain asphericity may be characterized by computing the aspect ratio $\langle \lambda_1 \rangle / \langle \lambda_2 \rangle$. Another characterization of the chain's shape is given by the moments:

$$\Delta_1 = \frac{\langle \lambda_1 - \lambda_2 \rangle}{\langle \lambda_1 + \lambda_2 \rangle}, \Delta_2 = \frac{\langle (\lambda_1 - \lambda_2)^2 \rangle}{\langle (\lambda_1 + \lambda_2)^2 \rangle} \tag{2.16}$$

We remind that $\Delta_1 = 2\langle \lambda_1 \rangle / R_g^2 - 1$ describes the mean ellipticity and Δ_2 the normalized variance of λ_1 and λ_2.[80,81] Obviously, $\Delta_1 = \Delta_2 = 1$ for rods and $\Delta_1 = \Delta_2 = 0$ for spheres.

2.3.2 Reciprocal space properties

Although direct real-space visualizations of the 2D polymer systems we focus on in this thesis is experimentally feasible,[16,17,22] allowing thus a direct computation of various conformational properties, it is important to note that these properties are more commonly probed in reciprocal space by means of light, small angle X-ray or neutron scattering experiments.[82] Using appropriate labeling techniques this allows to extract the coherent intramolecular structure factor $F(q)$ and the total monomer structure factor $S(q)$. In this section we review some theoretical concepts related to these quantities. The simulation results concerning the form and structure factor will be discussed in details in Sec. 3.4.

Form and structure factors. The coherent intramolecular structure factor $F(q)$ more briefly called "structure factor" or "form factor"[59,82] is computed by:

$$F(q) = \frac{1}{N} \sum_{n,m=1}^{N} \langle \exp\left[i\underline{q} \cdot (\underline{r}_n - \underline{r}_m) \right] \rangle \tag{2.17}$$

$$= \frac{1}{N} \langle || \sum_{n=1}^{N} \exp\left(i\underline{q} \cdot \underline{r}_n \right) ||^2 \rangle, \tag{2.18}$$

The average $\langle \ldots \rangle$ is taken over all labeled chains of the system and (at least in computational studies) over several wave vectors $\underline{q}$ of same modulus q. The second representation of the form factor given above being an operation linear in N has obvious compuational advantages for large chain lengths.

A second experimentally important reciprocal space characterization of a polymer solution is given by the "total monomer structure factor"[79]

$$S(q) = \frac{1}{n_{\mathrm{mon}}} \sum_{n,m=1}^{n_{\mathrm{mon}}} \langle \exp\left[i\underline{q} \cdot (\underline{r}_n - \underline{r}_m) \right] \rangle \tag{2.19}$$

measuring the fluctuations of the total monomer density at a given wavevector $\underline{q}$. All n_{mon} monomers of the simulation box are assumed to be labeled and the average $\langle \ldots \rangle$ is performed over all configurations of the ensemble and all possible wavevectors of length $q = |\underline{q}|$.

Theoretical predictions for the intramolecular form factor We remind that for small wavevectors, in the so-called Guinier regime, the structure factor scales as[59,82]

$$F(q)/N = 1 - Q^2/d \text{ for } Q \ll 1 \tag{2.20}$$

with $Q \equiv qR_g$ being the reduced wavevector. If sufficiently small q-vectors are available the gyration radius R_g can thus in principle be determined experimentally from the form factor. We also remind that the Flory exponent ν, i.e. the inverse fractal dimension of a chain, is defined by the chain length dependence of the typical chain size, $R(N) \approx R_g(N) \sim N^{\nu}$, in the limit of asymptotically long chains.[83] For "open" chains with $1/\nu < d$ the fractal dimension determines the structure factor in the intermediate wavevector regime[82]

$$F(q) \sim N^0 q^{-1/\nu} \text{ for } 1/R_g(N) \ll q \ll 1/\sigma \tag{2.21}$$

with σ characterizing either the monomer scale or the blob size ξ for semidilute solutions.[59] The so-called "Kratky representation" of the structure factor, $q^2F(q)$ *vs.* q, thus corresponds to a plateau for strictly Gaussian chains with $1/\nu = 2$.[82]

Obviously, Eq. (2.21) does not hold any more if the chain becomes *compact* ($1/\nu = d$), i.e., if Porod-like scattering due to the composition fluctuation at a well-defined "surface" $S(N)$ becomes possible. We remind that a surface may be characterized by its surface dimension d_s which is defined by the asymptotic scaling,[83]

$$S(N) \sim R_\mathrm{g}(N)^{d_\mathrm{s}} \sim N^{d_\mathrm{s}\nu} = N^{1-\nu\theta}. \tag{2.22}$$

We have introduced here the exponent $\theta \equiv 1/\nu - d_\mathrm{s} \geq 0$ to mark the difference between the fractal dimension of the object and its surface dimension. Obviously, for open chains $S(N) \sim N$, hence $\theta = 0$ and $d_\mathrm{s} = 1/\nu$. Since the scattering intensity $NF(q)$ of compact objects is known to be proportional to their surface $S(N)$ and since $F(q)$ must match the Guinier limit, Eq. (2.20), for $Q \approx 1$ it follows for asymptotically long chains that $NF(q) = N^2 f(Q) \sim S(N)$ with $f(Q)$ being a universal function. Using standard power-law scaling[59] this implies the "generalized Porod law"[82,84,85]

$$F(q)/N = f(Q) \approx 1/Q^{2/\nu - d_\mathrm{s}} = 1/Q^{1/\nu+\theta} \tag{2.23}$$

for the intermediate wavevector regime. As one expects, Eq. (2.23) yields for a smooth surface ($1/\nu = d$, $d_\mathrm{s} = d-1$, $\theta = 1$) the classical Porod scattering

$$F(q) \sim N/(N^{1/2}q)^3 \tag{2.24}$$

in $d = 2$ dimensions.[82] Note that Eq. (2.23) implies that $F(q)$ depends in general on the chain length.

As we shal show in Sec. 3.3.6, we have $d_\mathrm{p} = d - \theta_2 = 5/4$ in the compact chain limit, i.e. the difference θ between the fractal dimension of the object and its surface dimension is set by

$$\theta \stackrel{!}{=} \theta_2 = 3/4. \tag{2.25}$$

We present here an alternative derivation of this important identification using the fact that the form factor quite generally may be written as[33,46]

$$F(q) = \frac{1}{N}\int_0^N ds\ 2(N-s) \times G_\mathrm{e}(q,s) \tag{2.26}$$

using the Fourier transform $G_\mathrm{e}(q,s)$ of the normalized two-point intramolecular correlation function $G_\mathrm{e}(r,s)$ averaging over all pairs of monomers $(n, m = n+s-1)$. The factor $2(N-s)$ counts the number of equivalent monomer pairs separated by an arc-length s. As we have seen in Sec. 3.3.2, $G_\mathrm{e}(r,s)$ is well approximated by the distribution $G_2(r,s)$ for $s \ll N$ and $N \to \infty$. For asymptotically long chains it is justified to neglect chain-end effects ($s \to N$), i.e. physics described by the contact exponents θ_0 and θ_1. Focusing in addition on sufficiently large subchains ($g \ll s$) the Redner-des Cloizeaux approximation, Eq. (3.18), for $i = 2$ is assumed to be rigorously valid for all s. We compute first the 2D Fourier transform

$$G_2(q,s) = \int_0^\infty c_2 x^{\theta_2} e^{-k_2 x^2}\ 2\pi x dx J_0(qx) \tag{2.27}$$

with $2\pi J_0(z) = 2\int_0^\infty \cos(z\cos(\theta))d\theta$ being an integer Bessel function[86] and $x = r/R_2(s) = r/bs^{1/2}$, $\theta_2 = 3/4$, $k_2 = 1+\theta_2/2$, $c_2 = k_2^{k_2}/\pi\Gamma(k_2)$ as already defined in Sec. 3.3.2. As can be seen from Eq. (11.4.28) of Ref.,[86] this integral is given by a standard confluent hypergeometric function, the Kummer function $M(a,b,-z)$,

$$G_2(q,s) = M(1+\theta_2/2, 1, -z) \tag{2.28}$$

with $z = (qb)^2 s/4k_2$. According to Eq. (13.1.2) and Eq. (13.1.5) of [86] the Kummer function can be expanded as

$$M(a,b,-z) \approx 1 - \frac{az}{b} \text{ for } |z| \ll 1, \tag{2.29}$$

$$M(a,b,-z) \approx \frac{\Gamma(b)}{\Gamma(b-a)} z^{-a} \text{ for } z \gg 1. \tag{2.30}$$

Using Eq. (2.28) this yields, respectively, the small and the large wavevector asymptotic behavior of the Fourier transform of $G_2(r,s)$

$$G_2(q,s) \approx 1-(1+\theta_2/2)z \text{ for } z \ll 1, \tag{2.31}$$

$$G_2(q,s) \approx \frac{z^{-1-\theta_2/2}}{\Gamma(-\theta_2/2)} \sim q^{-2-\theta_2} \text{ for } z \gg 1. \tag{2.32}$$

Note that Eq. (2.31) implies $G_2(q=0,s)=1$ as one expects due to the normalization of $G_2(r,s)$.

After integrating over s following Eq. (2.26) and defining $Z=(qb)^2N/4k_2$ one obtains for the Guinier regime of the form factor

$$F(q) \approx N\left(1-\frac{1+\theta_2/2}{3}Z\right) \text{ for } Z \ll 1, \tag{2.33}$$

i.e. according to Eq. (2.20) we have, as one expects,

$$R_{\mathrm{g}}^2(N)=\frac{1}{6}b^2N\frac{1+\theta_2/2}{k_2}=\frac{b^2N}{6}. \tag{2.34}$$

Eq. (2.34) is of course slightly at variance with the measured ratio $(R_{\mathrm{e}}(N)/R_{\mathrm{g}}(N))^2<6$ due the chain end effects discussed in Sec. 3.3.2. These effects are neglected here. We show now that the form factor becomes a power law in agreement with the scaling relation Eq. (2.23). This is done by integrating Eq. (2.23) with respect to s. This gives

$$\begin{aligned} F(q) &\approx \frac{2N}{\Gamma(2-\theta_2/2)}Z^{-(1+\theta_2/2)} \\ &\sim N^{-\theta_2/2}q^{-(2+\theta_2)} \text{ for } Z \gg 1. \end{aligned} \tag{2.35}$$

Obviously, it is also possible to directly integrate Eq. (2.28) with respect to s as suggested by Eq. (2.26). This yields the complete Redner-des Cloizeaux approximation of the form factor

$$\begin{aligned} \frac{F(q)}{N} &\approx 2M\left(1+\frac{\theta_2}{2},2,-Z\right) \\ &- M\left(1+\frac{\theta_2}{2},3,-Z\right) \\ &+ \frac{1}{3}\left(1+\frac{\theta_2}{2}\right)Z\ M\left(2+\frac{\theta_2}{2},4,-Z\right) \end{aligned} \tag{2.36}$$

which can be computed numerically. Using again the expansions of the Kummer function, Eq. (2.29) and Eq. (2.30), one verifies readily that Eq. (2.36) yields the asymptotics for small and large wavevectors already given above. It is convenient from the scaling point of view to replace the variable Z used above by the reduced wavevector $Q=qR_{\mathrm{g}}(N)$ substituting

$$Z \Longrightarrow \frac{6}{4}Q^2(1+\Theta_2/2)=\frac{12}{11}Q^2, \tag{2.37}$$

as suggested by Eq. (2.34). Defining the reduced form factor $y(Q)\equiv(F(q)/N)Q^2$ and reexpressing Eq. (2.35) in these terms this implies

$$\begin{aligned} y(Q) &\approx \frac{2}{\Gamma(2-\Theta_2/2)}\left(\frac{3}{2+\Theta_2}\right)^{-(1+\Theta_2/2)}Q^{-\Theta_2} \\ &\approx \frac{1.98}{Q^{3/4}}, \end{aligned} \tag{2.38}$$

in agreement with Eq. (2.23). Note that due to this substitution the Guinier limit of the Redner-des Cloizeaux approximation of the form factor is correct by construction. We emphasize that the presented derivation does *not* depend explicitly on the density or the persistence length of the solution. It should apply equally to melts ($\rho \to 1$) and to melts of blobs ($N \gg g$).

Chapter 3

Flexible Polymers

3.1 Introduction

Background and motivation. Three-dimensional (3D) bulk phases of dense homopolymer solutions and blends are known to be well-described by standard mean-field perturbation calculations.[1,33,59,79,87] Provided that the length N of the (both linear and monodisperse) polymer chains and the monomer number density ρ are sufficiently large, the polymers adopt thus (to leading order) Gaussian chain statistics, i.e. the typical chain size R scales as

$$R \sim N^{\nu} \text{ for } \rho \gg \rho^* \approx N/R^{d\nu} \tag{3.1}$$

with $d = 3$ being the spatial dimension, $\nu = 1/2$ the inverse fractal dimension of the chains,[83] often called "Flory's exponent", and ρ^* the so-called "overlap density" or "self-density".[1,33] Even the weak scale-free corrections with respect to the Gaussian reference implied by the interplay of chain connectivity and incompressibility of the solutions on large scales are neatly captured by one-loop perturbation calculations.[33,88] The success of the mean-field approach for dense systems in $d = 3$ is of course expected from the fact that large scale properties are dominated by the interactions of many polymers with each of these interactions only having a small (both static and dynamical) effect.[59]

Obviously, the number of chains a reference chain interacts with, and the success of a mean-field approach, depends on the spatial dimension d of the problem considered as implied by the strong-overlap condition[59]

$$\rho^*/\rho \approx N/\rho R^d \sim N^{1-d\nu} \ll 1, \tag{3.2}$$

i.e. for to leading order Gaussian chains ($\nu = 1/2$) the mean-field approach becomes questionable below $d = 3$. Due to the increasing experimental interest on mechanical and rheological properties of nanoscale systems in general[10] and on dense polymer solutions in reduced effective dimensions $d < 3$ in particular[14–23] one is naturally led to question theoretically[65,66,89–95] and computationally[45–49,51,69,72–74,96,97] the standard mean-field results. Especially polymer solutions and melts confined to effectively two-dimensional (2D) thin films and layers are of significant technological relevance with opportunities ranging from tribology to biology.[14,15,18,20] In this chapter we shall consider such ultrathin films focusing on numerical results[45–51,69,72] obtained on both self-avoiding and flexible homopolymers confined to strictly $d = 2$ dimensions where chain overlap and intersection are strictly forbidden.

Compactness of the chains. As first suggested by de Gennes,[59] it is now generally accepted that such 2D "self-avoiding walks" (SAW) adopt compact and segregated conformations at high densities,[16,17,45–47,50,51,65,66,69,72,91] i.e., the typical chain size R scales as

$$R \approx (N/\rho)^{\nu} \text{ where } \nu = 1/d = 1/2. \tag{3.3}$$

Interestingly, according to Eq. (3.3) the typical chain size is set alone by the density of chains ρ/N and does thus not depend on other local monomeric parameters such as the (effective) excluded volume or the

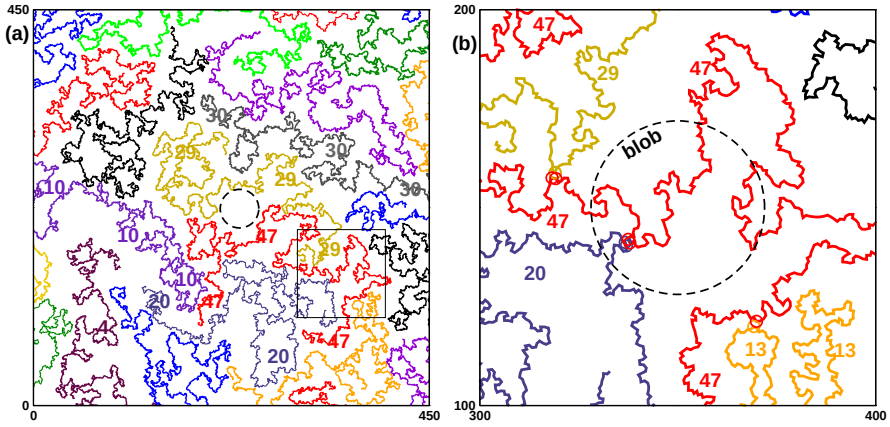

Figure 3.1: Semidilute regime for number density $\rho = 0.125$ and chain length $N = 2048$. The numbers refer to a chain index used for computational purposes. The dashed spheres represent a hard disk of uniform mass distribution having a radius of gyration R_g equal to the semidilute blob size $\xi \approx 31$ of the given density. As shown in panel **(a)** some chains are still rather elongated (e.g., chain 10 or 30) and the swollen chain statistics remains relevant on small scales ($r \ll \xi$). On larger scales the chains are shown to adopt (on average) compact configurations with power-law exponents $\nu = 1/d$ and $\theta_2 = 3/4$. The square in the first panel is redrawn with higher magnification in panel **(b)**. The spheres (not to scale) correspond to monomers interacting with monomers from other chains.

chain persistence length. As already stated we assume that chain intersections are strictly forbidden.[66] This must be distinguished from systems of so-called "self-avoiding trails" (SAT) which are characterized by a finite chain intersection probability. Relaxing thus the topological constraint SAT have been argued to belong to a different universality class revealing mean-field-type statistics with rather strong logarithmic N-corrections.[66,90] An experimentally relevant example for SAT is provided by polymer melts confined to thin films of finite width H allowing the overlap of the chains in the direction perpendicular to the walls. At variance to Eq. (3.3) such systems are predicted to reveal swollen chain statistics with

$$R^2 \sim N \log(N)/H\rho \tag{3.4}$$

as confirmed recently numerically by means of Monte Carlo (MC) simulation of the bond-fluctuation model[96] and by molecular dynamics (MD) simulation[43,44] of a standard bead-spring model[97] essentially identical to the one further discussed in the present study.

Non-Gaussianity and surface fractality. It is important to stress that the compactness of the strictly 2D chains, Eq. (3.3), does *not* imply Gaussian chain statistics since other critical exponents with non-Gaussian values have been shown to matter for various experimentally relevant properties.[45–47,65,66,91] It is thus incorrect to assume that excluded-volume effects are screened[73] as is approximately the case for 3D melts.[33] Also the segregation of the chains does by no means impose disklike shapes minimizing the contour perimeter of the (sub)chains. As may be seen from the snapshot presented in Fig. 3.2, the chains adopt instead rather fractal shapes of irregular contours.[45–48,72–74] Focusing on dense 2D melts it has been shown recently both theoretically[66] and numerically[45–48] that the irregular chain contours are characterized by a fractal perimeter of typical length

$$P \sim N n_{\rm int} \sim R^{d_{\rm p}} \sim N^{d_{\rm p}/d} \text{ with } d_{\rm p} = d - \theta_2 = 5/4 \tag{3.5}$$

where $n_{\rm int}$ stands for the fraction of monomers of a chain interacting with monomers of other chains. The fractal line dimension $d_{\rm p}$ is set by Duplantier's contact exponent $\theta_2 = 3/4$ characterizing the size distribution of inner chain segments.[65] We remind that Duplantier's theoretical predictions obtained using conformal

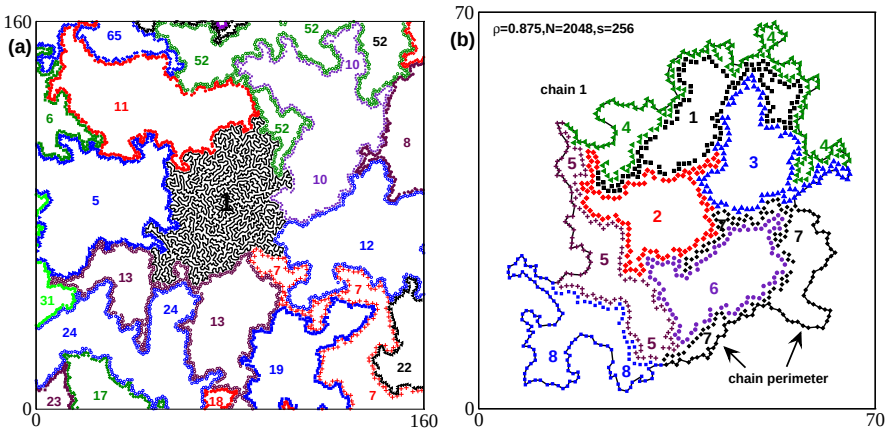

Figure 3.2: A dense melt for density $\rho = 0.875$ and chain length $N = 2048$: **(a)** Only "chain 1" in the middle is fully drawn while for the other chains only the perimeter monomers interacting with other chains are indicated. The chains are compact, i.e., they fill space densely, and interact typically with about 6 other chains. However, compactness does apparently still not imply a disk-like shape which would minimize the perimeter length P as may be seen, e.g., from the chain 7 or 52. **(b)** Self-similarity of compactness and perimeter fractality on all scales shown for chain 1. The solid line indicates the perimeter of this chain with respect to monomers of other chains. We consider 8 consecutive subchains of length $s = 256$ and compute their respective perimeter monomers being close to monomers from other chains or subchains. The subchains are compact and of irregular shape, just as the total chains ($s = N$)

invariance[65] rely both on the topological constraint (no chain intersections) and the space-filling property of the melt.

Focus of this Chapter. Obviously, high densities are experimentally difficult to realize for strictly 2D layers[16,17,21] since the chains tend either do detach from the surface or interface or to overlap increasing thus the number of polymer layers as clearly shown from the pressure isotherms studied in Ref.[21]. Elaborating a short comment made recently,[48] one aim of the presented study is to show that eqs. (3.3,3.5) hold more generally for all densities assuming that the chains are sufficiently long. Following de Gennes' classical density crossover scaling[59] this allows to view the polymer solutions as space-filling melts of "blobs" containing

$$g(\rho) \approx \rho\xi^d(\rho) \approx 1/(b_0^d\rho)^{1/(\nu_0 d-1)} \sim 1/\rho^2 \tag{3.6}$$

monomers with $\xi \approx b_0 g^{\nu_0} \sim 1/\rho^{3/2}$ being the size of the semidilute blob where $\nu_0 = 3/4$ stands for Flory's chain size exponent for dilute swollen chains in $d = 2$ dimensions[59] and $b_0 \equiv \lim_{N\to\infty} R_0(N)/N^{\nu_0}$ for the corresponding statistical segment size. Here as throughout this thesis report we shall often characterize by an index 0 the dilute limit of a property. Having received experimental attention recently,[16,17,21] we shall also discuss the density dependence of various thermodynamic properties such as the dimensionless compressibility

$$g_{\rm T}(\rho) \equiv \lim_{N\to\infty} T\rho/K = \lim_{N\to\infty} \left(\lim_{q\to 0} S(q)\right) \tag{3.7}$$

which may be either obtained from the compression modulus K of the solution[43,78] or from the low-wave vector limit of the total monomer structure factor $S(q)$.[32,33] As one expects according to a standard density crossover scaling *à la* de Gennes[59] we will demonstrate numerically that the dimensionless compressibility $g_{\rm T}(\rho)$ scales as the blob size $g(\rho)$. This is of some importance since due to the generalized Porod scattering of the compact chains the intrachain coherent structure factor $F(q)$ is shown to scale as[45–47]

$$NF(q) \approx N^2/(qR)^{2d-d_{\rm p}} \sim P \tag{3.8}$$

in the intermediate wave vector regime $1/R \ll q \ll 1/\xi$, as predicted theoretically by Eq. (2.36).[46] It is hence incorrect to determine the blob size by means of an Ornstein-Zernike fit to the intramolecular form factor $F(q)$ as done, e.g., in Ref.[17].

3.2 Thermodynamic properties

3.2.1 Energy

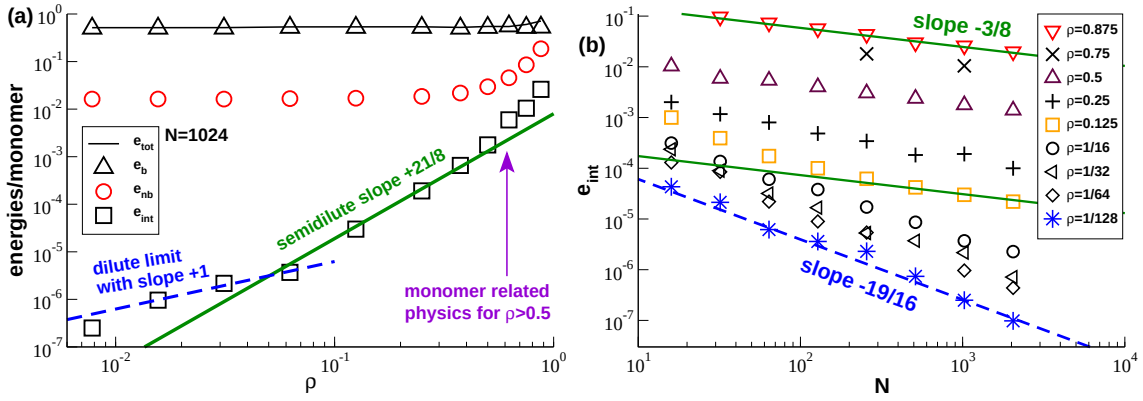

Figure 3.3: Various mean energy contributions per monomer: **(a)** Total energy $e_{\rm tot}$, bonding energy $e_{\rm b}$, excluded volume energy $e_{\rm nb}$ and interaction energy $e_{\rm int}$ between monomers of different chains as a function of density for $N = 1024$. **(b)** Interchain interaction energy $e_{\rm int}$ as a function of chain length N for different densities. The dashed and solid power-law slopes represent, respectively, the predicted asymptotic behavior for the dilute and dense density limits.[48]

From the numerical point of view the simplest thermodynamic property to be investigated here is the total mean interaction energy per monomer $e_{\rm tot}$ due to the Hamiltonian described in Sec. 2.1. As shown in panel (a) of Fig. 3.3, it is essentially density independent and always dominated by the bonding potential $e_{\rm b}$ (triangles). Due to the harmonic springs used we have $e_{\rm b} \approx k_{\rm B}T/2$ with a small positive correction due to the excluded volume repulsion which tends to increase the bond length. The total non-bonded excluded volume interaction per monomer $e_{\rm nb}$ (spheres) becomes constant at low densities where it is dominated by the excluded volume interaction of curvilinear neighbors on the same chain. The non-bonded energy $e_{\rm nb}$ increases of course for larger densities, but remains always smaller than the bonded energy $e_{\rm b}$. (Values of $e_{\rm nb}$ for $N = 1024$ are included in Table 2.1.) From the theoretical point of view more interesting is the contribution to the total excluded volume interaction due to the contact of monomers from different chains measured by $e_{\rm int}$ (squares). This interchain energy contribution is of course proportional to the density in the dilute regime (dashed line) due to the mean-field probability that two chains are in contact. At higher semidilute densities up to $\rho \approx 0.5$ a much stronger power-law exponent $\approx 21/8$ is seen. This apparent exponent will be traced back in Sec. 3.3.6 to the known values of the universal exponents ν and θ_2 of the dilute and dense limits. The interaction energy $e_{\rm int}$ increases even more strongly for our largest densities where the semidilute blob picture becomes inaccurate. At variance to the other mean energies $e_{\rm int}$ has a strong chain length effect as revealed in panel (b). The indicated power-law slopes correspond to the predicted exponents $\nu\theta_2 = 19/16$ and $3/8$ for, respectively, the dilute (dashed line) and dense (bold lines) density limits as further discussed below in Sec. 3.3.6.

3.2.2 Pressure

While the energy contributions discussed above cannot be probed in a real experiment, the osmotic pressure of the polymer solution can readily be accessed experimentally.[21] As described in Sect. 2.2, the mean pressure

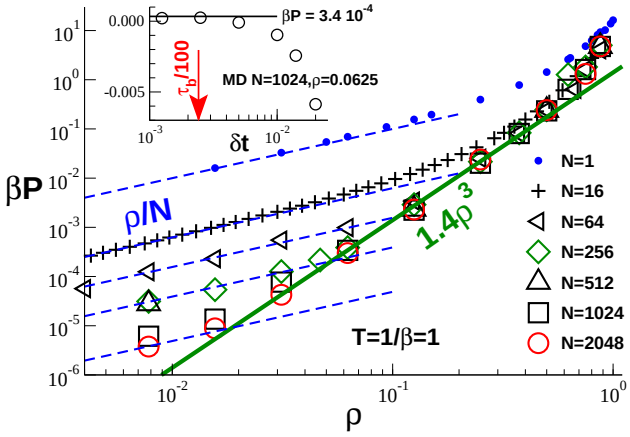

Figure 3.4: Pressure as a function of density ρ for different chain lengths N. Unconnected LJ beads are indicated by the small filled spheres. The data for $N \geq 256$ and $\rho \leq 0.125$ have been obtained using the slithering snake MC algorithm, all other data using MD with $\gamma = 0.5$ and $\delta t = 0.01$. The thin dashed lines give the osmotic pressure $\beta P = \rho/N$ in the dilute limit for $N = 1$, 16, 64, 256 and 2048. The pressure becomes rapidly chain length independent with increasing N and ρ. The bold line indicates the power-law exponent $d\nu_0/(d\nu_0 - 1) = 3$ expected in the semidilute regime according to Eq. (3.9). Inset: Pressure as a function of the MD time increment δt for $N = 1024$ and $\rho = 0.0625$. The horizontal line corresponds to our MC result. As indicated by the vertical arrow the Verlet algorithm yields the correct pressure in the dilute limit if $\delta t \ll \tau_b/100$.

P at a given density ρ has been obtained by means of the virial equation $P = k_B T\rho + \langle \mathcal{W} \rangle / V$.[43] The main panel of Fig. 3.4 shows the pressure for different chain lengths N. The pressure increases of course strongly with density ρ. For very large densities the LJ excluded volume dominates all interactions, i.e. the pressure of polymer chains approaches the pressure of unbonded LJ beads (filled spheres). The chain length only matters in the dilute limit for short chains and small densities.

Low-ρ limit. Let us focus first on the latter dilute limit where ultimately the translational entropy of the chains must dominate the free energy,[59] i.e. $\beta P \to \rho/N$ as indicated by the thin lines. Surprisingly, this (theoretically trivial) limit turns out to be numerically the most challenging regime, especially with increasing N. The main reason for this is that in this limit a large positive term, the kinetic pressure contribution $k_B T\rho$, is essentially cancelled by a large negative term, the excesss pressure $P_{ex} = \langle \mathcal{W} \rangle / V$. (The excess pressure is negative since it is dominated by the tensile bonding potential between connected beads.) This requires increasingly good statistics as N becomes larger. Due to this cancellation the precise determination of the pressure in the dilute limit becomes even delicate and surprisingly time consuming when the configurations are sampled by means of slithering snake MC moves (Sec. 2.1). However, using this method and given sufficient numerical precision the pressure approaches (as it should) the asymptotic dilute limit indicated by the thin dashed lines. This is indeed different if the systems are computed by MD simulation with a too large time step δt as shown in the inset of Fig. 3.4. The bond oscillation time τ_b is indicated by the vertical arrow. If δt is too large the bonds are slightly stretched on average, i.e. they become too tensile which corresponds to a too negative virial. Unfortunately, the bonding potential is that strong, i.e. the time scale τ_b so small, that it gets inefficient to compute the pressure using MD with $\delta t \ll \tau_b/100 \simeq 0.0024$.[98]

Returning to the main panel of Fig. 3.4 it is seen that the pressure becomes rapidly N-independent with increasing chain length and density. Since the non-bonded interactions become now dominant, the above-mentioned numerical problems become also irrelevant, i.e. the differences between MD results with $\gamma = 0.5$ and $\delta t = 0.01$ and the MC ensembles are negligible. Note the data points given in the main panel of the figure and in Table 2.1 all refer to the best δt-independent and thermodynamic relevant values available.

Semidilute density regime. From the theoretical point of view more interesting is the intermediate semidilute density regime indicated by the bold dashed power-law slope. The universal exponent can be understood by an elegant crossover scaling argument given by de Gennes[59] where the pressure is written as $P = \rho/N \times f(\rho/\rho^*)$ with $\rho^* \approx N/R^d \approx N^{1-d\nu_0}/b_0^d$ being the crossover density and $f(x)$ a universal function.

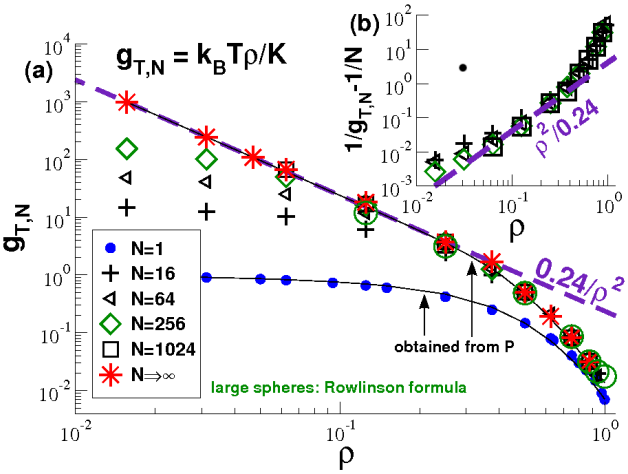

Figure 3.5: Determination of dimensionless compressibility $g_T(\rho) = \lim_{N\to\infty} g_{T,N}(\rho)$: **(a)** $g_{T,N}(\rho)$ obtained by various means for several chain lengths N. The thin lines correspond to a polynomial fit to $P(\rho)$ for $N = 1$ (lower thin line) and the largest chains available (upper thin line). The large spheres have been obtained using the Rowlinson formula, Eq. (3.13), for $N = 1024$. All other data correspond to the plateau of the total structure factor $S(q, N)$ for small wavevectors q. The bold dashed line indicates the power law expected for the semidilute regime, eq. (3.6). **(b)** Excess compressibility $1/g_{T,N} - 1/N$ yielding according to Eq. (3.12) the inverse compressibility for asymptotically long chains $1/g_T$.

Assuming P to be chain length independent for $x \gg 1$ this implies $f(x) \sim x^{1/(d\nu_0-1)}$ and, hence,

$$\beta P b_0^2 \approx (b_0/\xi(\rho))^d \approx (b_0^d\rho)^{d\nu_0/(d\nu_0-1)} \approx (b_0^2\rho)^3 \tag{3.9}$$

where we have used Eq. (3.6) to restate the well-known relation between pressure and blob size ξ.[59] The predicted exponent fits the data over about a decade in density where the blob size is sufficiently large. Additional non-universal physics related to the already mentioned LJ monomer interactions becomes relevant for densities around $\rho \approx 0.5$. Note that the axes of the panel are not expressed in fully dimensionless units which makes the comparison to real experiments difficult. Chosing as a (natural but arbitrary) length scale the effective segment size b_0 associated to the dilute radius of gyration, one may instead plot the rescaled pressure $y = \beta P b_0^d$ as a function of the reduced density $b_0^d\rho$. In the semidilute regime this corresponds to a power-law slope $y = a_P x^3$ with a power-law amplitude $a_P \approx 83.4$ (not shown). This dimensionless amplitude (or similar related values due to different choices of b_0) may be compared to real experiments or other computational models. As long as the blob size is sufficiently large, i.e. the density sufficiently small and the chains sufficiently large, molecular details should not alter this universal amplitude. (Persistence length effects should, e.g., change b_0 but not the amplitude a_P.) We also note that by matching of the dilute asymptote $\beta P = \rho/N$ with the semidilute pressure regime the prefactor of the crossover density ρ^* may be operationally defined as

$$\rho^* = a_P^{1-d\nu_0} \times N/R_g^d \approx 0.845/N^{1/2} \tag{3.10}$$

with R_g being the radius of gyration in the dilute limit. This implies $\rho^* \approx 0.02$ for our largest chains with $N = 2048$. Considering that the semidilute regime breaks down at $\rho \approx 0.5$ this limits the semidilute scaling to about an order of magnitude in density.

3.2.3 Compressibility

In the next paragraph we review and extend the thermodynamic definition of the bulk modulus of a polymer solution given in Sec. 2.2 and discuss its relation with the number of monomers in the semidilute blob. Later in this section we describe and compare three different methods allowing to measure this quantities precisely for our flexible polymer chains systems.

Definitions. Being an isotropic liquid a polymer solution is described in the hydrodynamic limit by only one elastic modulus, the bulk compression modulus

$$K \equiv 1/\kappa_T \equiv k_B T\rho/g_{T,N} = \rho\frac{\partial P}{\partial \rho}, \tag{3.11}$$

with κ_T being the standard isothermal compressibility[77] and $g_{T,N}$ the "dimensionless compressibility" for systems of finite chain length N. (The shear modulus G is by definition of a liquid given by $G = 0$.[1]) We use here the additional index N to distinguish $g_{T,N}$ from the dimensionless compressibility for asymptotically long chains $g_T \equiv \lim_{N\to\infty} g_{T,N}$. Due to the transitional entropy of the chains both quantities should be related by[33,59]

$$\frac{1}{g_{T,N}} = \frac{1}{N} + \frac{1}{g_T}, \tag{3.12}$$

i.e. $g_{T,N}$ and g_T are expected to differ strongly for small densities where g_T must be large. (Note that g_T corresponds to the excess contribution to the total free energy.) Our aim is to determine $g_{T,N}$ precisely comparing different techniques and to extrapolate then using Eq. (3.12) to g_T which should scale in the semidilute regime as the number of monomers per blob as stated by Eq. (3.6) in the Introduction.

Measurements. As mentioned in Sec. 2.2, the bulk compression modulus of a polymer solution can be computed numerically by fitting the pressure isotherms discussed in the previous section. The resulting curves for $N = 1$ and the largest chain lengths available are represented by the thin lines in the main panel of Fig. 3.5 where $g_{T,N}$ is traced as a function of density ρ. A disadvantage of this method is that $P(\rho, N)$ must be known for a large number of densities, especially for large ρ where the pressure increases strongly.

Alternatively, the compressibility for one specific density can be obtained from the plateau in the low-wavevector limit of the total structure factor $S(q, N)$ which is further discussed in Fig. 3.15 below. This method was used to obtain the bulk of the data presented in Fig. 3.5. Due to the large box sizes we have used (especially in the low-ρ limit) this method provides over the whole density range reliable numerical values only requiring the analysis of about 1000 more or less independent configurations which anyway had to be stored for the computation of various configurational properties.

Finally, a third method is available to compute the compressibility using the Rowlinson formula[78]

$$K = P + \frac{\langle \mathcal{X} \rangle}{V} - \frac{\beta}{V} \left\langle \delta^2 \mathcal{W} \right\rangle \tag{3.13}$$

with $\mathcal{W}$ being the already mentioned virial and $\mathcal{X}$ the so-called "hypervirial".[43] The hypervirial is defined by

$$\mathcal{X} = -\frac{1}{d^2} \sum_{i<j} r_{ij} \frac{\mathrm{d}w(r_{ij})}{\mathrm{d}r_{ij}} \tag{3.14}$$

with $r_{ij} = \sqrt{x_{ij}^2 + y_{ij}^2}$ being the distance between two interacting beads i and j and $w(r_{ij})$ the pair virial function defined in Eq. (2.5). Results obtained for $N = 1024$ using MC simulations are indicated by the large spheres in Fig. 3.5. While the computation of K using the Rowlinson formula is numerically trivial at high melt densities ($\rho > 0.5$), it becomes statistically delicate at lower densities where both K and P become small and a large positive hypervirial term $\langle \mathcal{X} \rangle / V$ essentially must cancel a large negative contribution due to the excess pressure fluctuation $\left\langle \delta^2 \mathcal{W} \right\rangle$. Since in addition to this the latter stress fluctuation contribution converges extremely slowly with time, the Rowlinson formula becomes frustratingly time consuming for smaller densities as discussed in Ref.[99].

Interpretation of data. In agreement with Eq. (3.11) and the scaling of the pressure discussed above the dimensionless compressibility $g_{T,N}$ is found to be strongly N-dependent for short chains and small densities where the translational entropy matters. This chain length dependence is, however, easily understood using Eq. (3.12) as explicitly checked by the scaling collapse shown in the inset. The scaling being successful for even rather small chains, this allows us to determine even from data obtained at small N the asymptotic chain length behavior g_T for all densities (indicated by stars). Consistent with Eq. (3.9) the dashed bold lines indicate the power-law asymptote

$$g_T \approx \frac{1}{3a_P(b_0^2\rho)^2} \approx 0.24/\rho^2 \tag{3.15}$$

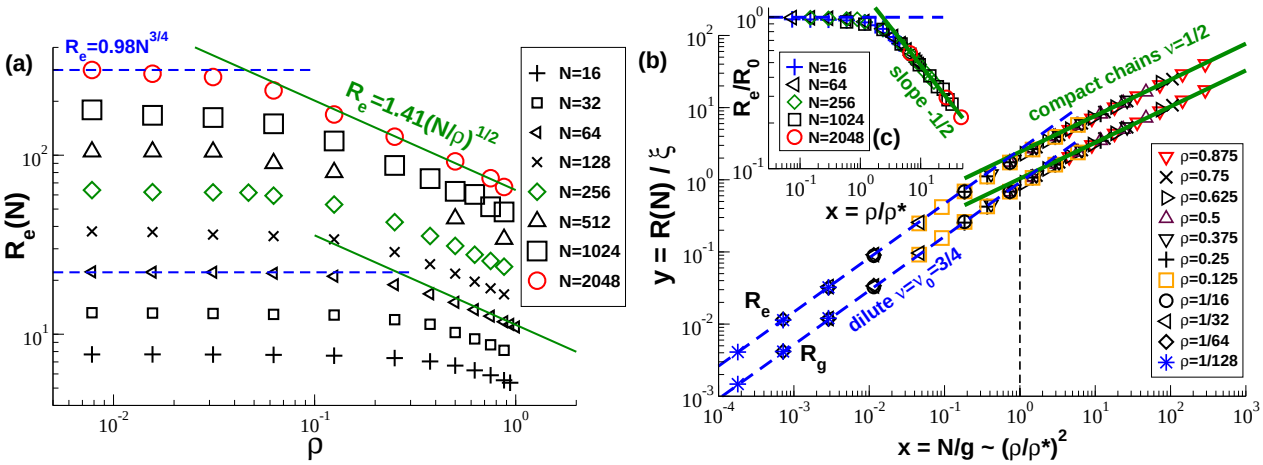

Figure 3.6: Average chain size R for a broad range of densities ρ and chain lengths N: **(a)** Root-mean-square chain end-to-end distance R_e as a function of density ρ. The dilute limit is characterized by an effective segment length $b_{e,0} = 0.98$ as shown by the dashed lines. The bold lines indicate the expected scaling $R_e \sim \rho^{-1/d}$ for high densities. **(b)** Successful scaling of R_e/ξ and R_g/ξ as functions of the reduced chain length N/g as expected from the standard density crossover scaling.[59] The exponent $\nu = \nu_0 \equiv 3/4$ for the dilute swollen chain limit is given by the dashed lines, the compact chain exponent $\nu = 1/d$ by the bold lines. **(c)** Replot of R_e focusing on the ρ-scaling for constant chain length N.

for the semidilute regime. Taking apart an arbitrary prefactor the number of monomers per blob g may thus be identified with the dimensionless compresssibility.

3.3 Conformational (real space) properties

3.3.1 Chain and subchain size

Asymptotic limits. That sufficiently long 2D polymer chains become indeed compact for all densities, as stated by Eq. (3.3), is shown in Fig. 3.6 presenting the overall chain size R as characterized by the root-mean square chain end-to-end distance R_e and the radius of gyration R_g.[79] As expected the typical chain size is found to increase with a power-law exponent $\nu = \nu_0 \equiv 3/4$ in the dilute limit (dashed lines) and with $\nu = 1/d$ for larger chains and densities in agreement with various numerical[51,69,72] and experimental studies.[16,17,22] The unscaled chain end-to-end distance R_e is traced as a function of density ρ in panel (a) confirming that the chain size decays according to Eq. (3.3) at high densities (bold line) while it becomes ρ-independent in the dilute limit where $R_e(N)/N^{\nu_0} \to b_{e,0} \approx 0.98$ for the largest chains probed. A similar plot exists for the chain radius of gyration.

Scaling with chain length. The scaling of the chain size for different densities as a function of chain length N is checked in panel (b) where the horizontal axis is rescaled with the number of monomers $g(\rho) \sim \rho^{-2}$ spanning the semidilute blob and the vertical axis by its size $\xi \sim \rho^{-3/2}$ in agreement with the standard density crossover scaling, Eq. (3.6). We fix the (slightly arbitrary) prefactors as

$$\begin{aligned} g &\equiv 0.09/(b_0^d\rho)^{1/(\nu_0 d-1)} \approx 5.43/\rho^2 \\ \xi &\equiv b_0 g^{\nu_0} \approx 1.35/\rho^{3/2} \end{aligned} \tag{3.16}$$

with $b_0 \equiv 0.37$ the dilute statistical segment length and trace $y = R(N)/\xi(\rho)$ as a function of $x = N/g(\rho)$. This choice allows to fix the intercept of the asymptotic power-law slopes for the radius of gyration at $(x, y) = (1, 1)$ as emphasized by the vertical dashed line.

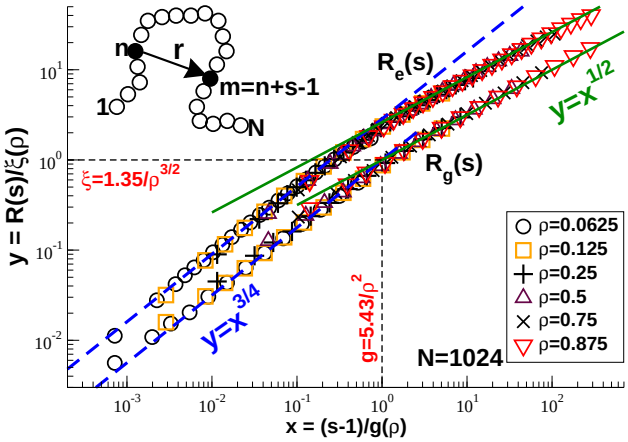

Figure 3.7: Root-mean-square subchain end-to-end distance $R_e(s)$ and radius of gyration $R_g(s)$ for subchains of $s = m - n + 1 \leq N$ monomers with $N = 1024$. Tracing $R_e(s)/\xi(\rho)$ and $R_g(s)/\xi(\rho)$ *vs.* $(s-1)/g(\rho)$ yields again a perfect data collapse for all densities.

Scaling with density. An equivalent data representation focusing on the chain size as a function of density taking as reference the dilute chain size $R_0 \equiv b_{e,0} N^{\nu_0}$ is shown in panel (c). We trace here R_e/R_0 as a function of the reduced density $x = \rho/\rho^*$ with $\rho^* = 0.845/N^{1/2}$ being the crossover density as defined by the presssure isotherm, Eq. (3.10). Within this prefactor choice for ρ^* the crossover for R_e occurs at about $x \approx 2$. For larger x the typical chain size decreases indeed as $R \sim 1/\sqrt{\rho}$ with increasing density (bold line) as expected for compact chains, Eq. (3.3). Below we refer to $N/g \approx (\rho/\rho^*)^2 \gg 1$ as the "compact chain limit" and to $g \to 0$, where the blob size becomes formally comparable or smaller than the monomer size, as the "melt limit".

Scaling of subchain size. To emphasize that it is not only the total chain which becomes compact but in a self-similar and hierarchical manner the chain conformation on all scales we present in Fig. 3.7 the scaling of the size of subchains of arc-length $s = m - n + 1 \leq N$ (see sketch). The subchain size is characterized (as before) by its root-mean-squared end-to-end distance $R_e(s)$ (upper data) and radius of gyration $R_g(s)$. To improve the statistics averages are taken over all monomer pairs (n, m) possible. Please note that averaging only over subchains at the curvilinear chain center $(n, m \approx N/2)$ slightly reduces chain end effects; however, the difference is negligible for the large chains we focus on. The limit $s = N$ corresponds obviously to the total chain size discussed above. As in panel (b) of Fig. 3.6 the reduced subchain size $y = R(s)/\xi(\rho)$ is plotted as a function of the reduced arc-length $x = (s-1)/g(\rho)$ using the same prefactor convention, Eq. (3.16). Data for one chain length, $N = 1024$, and a broad range of densities are presented. The data collapse is again perfect and the asymptotic power-law slopes for $x \ll 1$ (dashed lines) and $x \gg 1$ (bold lines) for the radius of gyration intercept at $(x, y) = (1, 1)$. It is in fact the subchain size radius of gyration $R_g(s)$ for $N = 1024$ and $N = 2048$ for the densities $\rho = 0.0625$ and $\rho = 0.125$ which has allowed the most precise determination of the prefactors indicated in Eq. (3.16). Note also that since $R_e(s)$ becomes compact more rapidly as $R_g(s)$, a blob size defined using $R_e(s)$ would be slightly smaller. The numerical prefactors depend thus somewhat on the property probed.

Success of scaling at high densities. Finally, we draw attention to the fact that the blob scaling of the chain and subchain size is even successful for our highest densities where the blob picture clearly breaks down for some other properties as discussed, e.g., in Sec. 3.2.2. This is due to the fact that $R(s)$ is set in this limit by the typical distance $d_{cm} \approx (s/\rho)^{1/d}$ between the chain or subchain center of masses and this irrespective of the physics (monomer size, persistence length, ...) on small scales. Since $\rho \approx g/\xi^d$ is imposed, a different choice of the blob size only leads to a shift of the data along the bold power-law slope $\nu = 1/d$.

Only for sufficiently low densities where (sub)chains smaller than the blob can be probed it is possible to test the blob scaling and to adjust the prefactors.

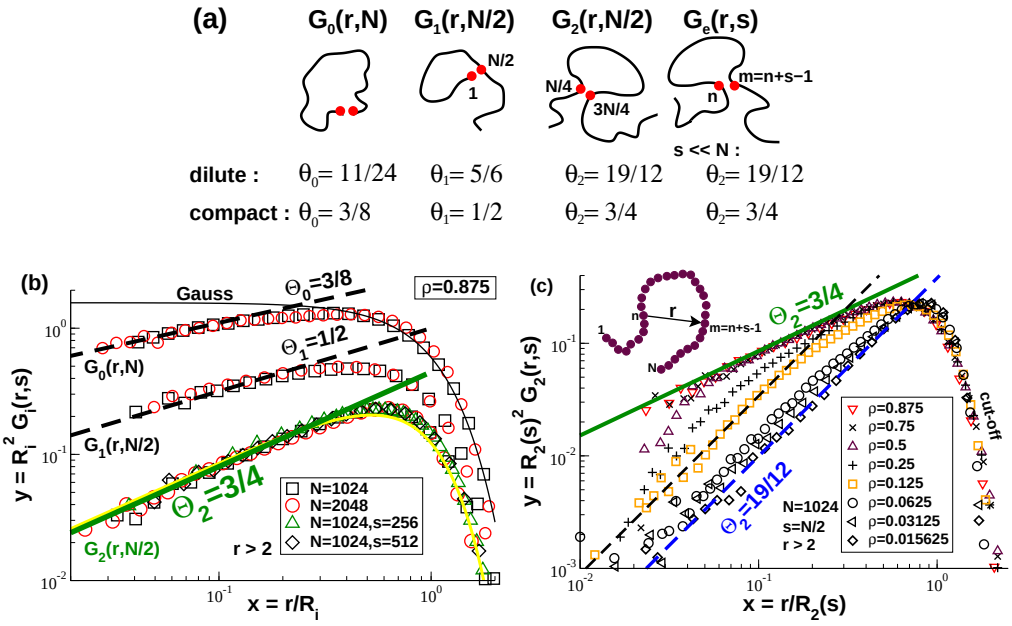

Figure 3.8: **(a)** Sketch of the intrachain distributions $G_i(r,s)$ and the corresponding contact exponents θ_i for dilute and compact chain limits.[65] **(b)** Scaling plots for one density $\rho = 0.875$: $G_0(r,N)$, $G_1(r,N/2)$ and $G_2(r,N/2)$ for $N = 1024$ (squares) and $N = 2048$ (spheres) and $G_e(r,s)$ for $N = 1024 \gg s$ with $s = 256$ (triangles) and $s = 512$ (diamonds). The distributions $G_0(r,N)$ and $G_1(r,N/2)$ are shifted upwards for clarity. All data for different N and s collapse on the respective master curves if $y = R_i^2 G_i(r,s)$ is plotted *vs.* the reduced distance $x = r/R_i$ with R_i^2 being the second moment of the corresponding distribution. The thin line indicates the distribution for Gaussian chains. The power laws $y \approx x^{\theta_i}$ observed for $x \ll 1$ confirm Duplantier's prediction. The thin solid line at the bottom shows Eq. (3.18) for $i = 2$. **(c)** Distribution $G_2(r, s = N/2)$ for various densities and $N = 1024$. The exponent θ_2 for $x \ll 1$ is given by $\theta_2 = \theta_{2,0} \equiv 19/12$ in the dilute limit and for distances probing the structure within the semidilute blobs (dashed lines).

3.3.2 Intrachain contact probability

Definitions. Being characterized by the same Flory exponent ν as their 3D counterparts does by no means imply that compact 2D chains are Gaussian.[65,66] This can be directly seen, e.g., from the different (properly normalized) probability distributions $G_i(r,s)$ of the intrachain vectors $\underline{r} = \underline{r}_m - \underline{r}_n$ between the monomers n and $m = n + s - 1$ presented in Fig. 3.8. As illustrated in panel (a),

- $G_0(r, s = N)$ characterizes the distribution of the total chain end-to-end vector ($n = 1$, $m = N$),
- $G_1(r, s = N/2)$ the distance between a chain end and a monomer in the middle of the chain ($n = 1$, $m = N/2$),
- $G_2(r, s = N/2)$ the distribution of an inner segment vector between the monomers $n = N/4$ and $m = 3N/4$,
- while $G_e(r,s)$ *averages* over all pairs of monomers $(n, m = n + s - 1)$ for $s \leq N$.[33]

Melt limit. Let us focus first on the large-ρ limit where the blob size becomes negligible.[45,46] As shown in panel (b) for one high density, $\rho = 0.875$, all data for different N and s collapse on three distinct master curves if the axes are made dimensionless using the measured second moment R_i^2 of the respective distribution. ($R_2(s)$ is the subchain size $R_e(s)$ discussed already in Sec. 3.3.1.) The only relevant length scale is thus the typical size of the subchain itself. The distributions are all non-monotonous and are thus *qualitatively* different from the Gaussian distribution $y = \exp(-x^2)/\pi$ (thin line) expected for uncorrelated ideal chains in $d = 2$. Please note that we have binned the data logarithmically and only distances $r > 2$ are presented to suppress local packing effects of the LJ beads which would superimpose and blur the expected scaling behavior for small distances. Confirming Duplantier's prediction[65] we find

$$R_i^d G_i(r,s) = x^{\theta_i} f_i(x) \tag{3.17}$$

with $x = r/R_i$ being the scaling variable. The indicated power-law slopes correspond (from the top to the bottom) to the contact exponents $\theta_0 = 3/8$, $\theta_1 = 1/2$ and $\theta_2 = 3/4$ describing the small-x limit where the universal functions $f_i(x)$ become constant. Especially the largest of these exponents, θ_2, is clearly visible. The contact probability for two monomers of a chain in a 2D melt is thus strongly suppressed compared to ideal chain statistics ($\theta_0 = \theta_1 = \theta_2 = 0$).

The rescaled distributions show exponential cut-offs for large distances. The Redner-des Cloizeaux formula[100] is a useful interpolating formula which supposes that

$$f_i(x) = c_i \exp(-k_i x^2). \tag{3.18}$$

The constants $k_i = 1 + \theta_i/2$ and $c_i = k_i^{k_i}/\pi\Gamma(k_i)$ with $\Gamma(z)$ being the Gamma function[86] are imposed by the normalization and the second moment of the distributions.[101] This formula is by no means rigorous but yields reasonable parameter free fits as it is shown by the thin solid line for $f_2(x)$.

Density variation. Density effects are investigated in panel (c) of Fig. 3.8 for the distribution $G_2(r, s = N/2)$ for one chain length $N = 1024$. (Qualitatively similar plots exists for the other distributions.) As in panel (b) the data points for $r > 2$ have been binned logarithmically. The axes are again rescaled with the measured second moment $R_2^2(s)$ of the given distribution. The scaling for very small ($\rho < 0.0625$) and very high densities ($\rho \geq 0.5$) is particulary simple. In these limits $R_2(s)$ is the only relevant length scale and the data are thus found to collapse on two respective master curves. The dashed and bold power-law slopes indicated in the figure correspond to the exponents $\theta_2 = \theta_{2,0} \equiv 19/12$ and $\theta_2 = 3/4$ predicted for both limits.[65] Obviously, the scaling of $G_2(r, N/2)$ becomes more intricate for semi-dilute densities where the blob size ξ sets an additional length scale.[48] For $s = N/2 \gg g(\rho) \gg 1$ one expects to observe two power-law asymptotes, one scaling as $G_2(r, N/2) \sim r^{19/12}$ if the conformational properties within the blob are probed ($r \ll \xi$) and one as $G_2(r, N/2) \sim r^{3/4}$ for $\xi \ll r \ll R(s)$. Although much larger blobs are certainly warranted to demonstrate this unambiguously, this expected behavior is qualitatively consistent with our data as may be seen for $\rho = 0.125$.

Size distribution of subchain of arc-length s. It is also instructif to compute the size distribution $G_e(r, s)$ of subchains of arc-length s where we average over all pairs of monomers n and $m = n + s - 1$. Obviously, $G_e(r, s) \approx G_0(r, N)$ for very large subchains $s \to N$ (not shown). As can be seen in panel (b) of Fig. 3.8, the rescaled distributions $G_e(r, s)$ and $G_2(r, N/2)$ become identical for sufficiently large chains (where chain-end effects can be ignored) if $N/2$ and s are either both much larger or much smaller than the blob size g. It is for this reason that the exponent θ_2 is central for asymptotically long chains. This will become obvious below in Sec. 3.3.5 and Sec. 3.4.1. The two exponents θ_0 and θ_1 are only relevant if the measured property specifically highlights chain end effects as in the example presented in the next paragraph.

Chain and subchain size revisited

Reminder. The log-log representation chosen in Fig. 3.7 masks deliberately small corrections to the leading power law due to chain end effects which exist in 2D as they do in 3D polymer solutions and

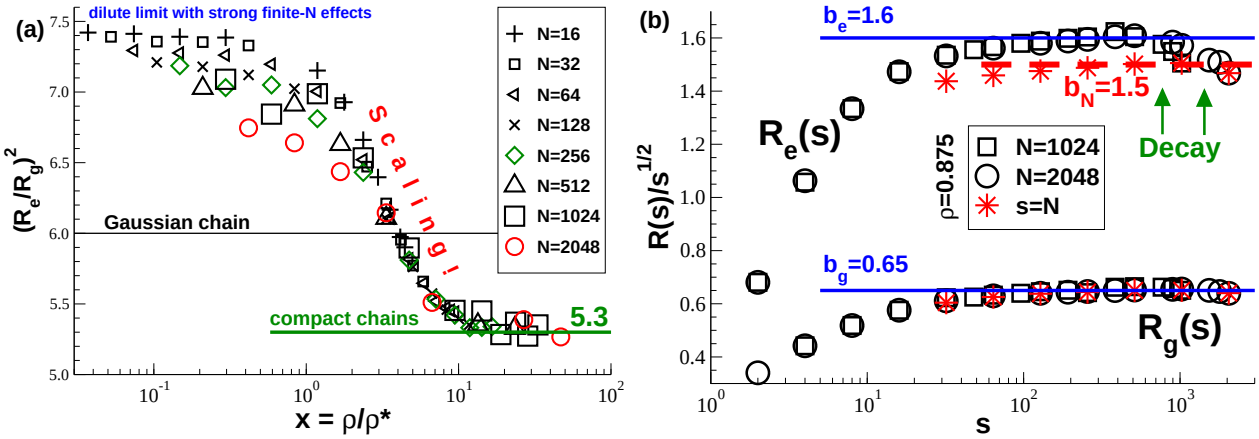

Figure 3.9: Corrections to the dominant power law of the (sub)chain size: **(a)** Scaling plot of $(R_e/R_g)^2$ for different chain lengths N as a function of reduced density $x = \rho/\rho^*$. In the dilute limit the ratio clearly exceeds the Gaussian value (thin line) but does not become $35/4 = 8.75$ as one would expect if the dilute Flory exponent $\nu = \nu_0 = 3/4$ would hold rigorously for all subchains, Eq. (2.12). More importantly, it is demonstrated that with increasing number of blobs the ratio approaches for all densities and chain lengths a universal limit ≈ 5.3 confirming older numerical studies.[50,51,69,72] **(b)** Focusing on the density $\rho = 0.875$ the reduced subchain size $R(s)/s^{1/2}$ is characterized either by the root-mean-square end-to-end distance $R_e(s)$ (top data) or by the radius of gyration $R_g(s)$ (bottom data). Interestingly, $R_e(s)/s^{1/2}$ decays for $s > N/2$ due to chain-end effects. The solid horizontal lines indicate the effective segment sizes $b_e = 1.6$ and $b_g = 0.65$ obtained for $100 \ll s \ll N$ from $R_e(s)/s^{1/2}$ and $R_g(s)/s^{1/2}$, respectively. The dashed line corresponds to an apparent effective segment size $b_N = 1.5$ from the end-to-end distances $R_e(N)$ of our longest chains.

melts.[33] As explained in details in Sec. 2.3, assuming that the typical size of all subchains is settled by the same ν exponent, the ratio $(R_e(N)/R_g(N))^2$ do not depend on the spatial dimension or the local monomer properties and can be rigorously calculated by $(R_e(s)/R_g(s))^2 = (2\nu+1)(2\nu+2)$ which yealds 6 for $\nu = 1/2$ and $35/4 = 8.75$ for $\nu = 3/4$.

Corrections to the assumed power-law behavior at the *lower* integration cut-off should not alter these values if s is sufficiently large.

Observed total chain ratio $(R_e(N)/R_g(N))^2$. The scaling of the ratio $(R_e/R_g)^2$ for the total chain, i.e. $s = N$, is put to the test in panel (a) of Fig. 3.9. Data for different chain length N is traced as a function of the reduced density $x = \rho/\rho^*$. Please note the strong finite-N effects in the dilute limit where the ratio becomes of course density independent. That the ratio becomes larger than the Gaussian value (thin line) in this limit is expected from Eq. (2.12). Interestingly, the corresponding value 8.75 is clearly too large and not compatible with our data which indicates that the chains are less swollen at the chain ends (as further discussed in Sec. 3.3.3). More importantly, it is seen that the scaling works nicely once the density and/or the chain length are sufficiently large ($x > 1$). The data decreases then systematically levelling off to a numerical plateau value 5.3 for $x > 3$ in conflict to a rigorous power-law with a compact chain Flory exponent $\nu = 1/2$. This confirms similar observations made in previous simulations using much shorter chains.[50,51,69,72]

This behavior can be understood by considering more systematically the subchain sizes as shown in panel (b) of Fig. 3.9 for one high density $\rho = 0.875$. Using log-linear coordinates we present here $R_e(s)/s^{1/2}$ and $R_g(s)/s^{1/2}$ *vs.* s and $R_e(N)/N^{1/2}$ and $R_g(N)/N^{1/2}$ *vs.* N (stars). The reduced radius of gyration (bottom data) becomes in fact rapidly constant and chain length independent. As emphasized by the bottom horizontal line we find

$$b_g \approx R_g(s)/s^{1/2} \approx R_g(N)/N^{1/2} \text{ for } s, N \gg 100 \tag{3.19}$$

with $b_g = 0.65$ for $\rho = 0.875$. Interestingly, we observe *non-monotonous* behavior for $R_e(s)/s^{1/2}$ with a decay for $s > N/2$. Due to this decay $R_e(N)/N^{1/2}$ (stars) is systematically *below* the corresponding internal chain distance $R_e(s)/s^{1/2}$. Fitting the total chain end-to-end distances yields an effective segment size[79]

$$b_N \approx R_e(N)/N^{1/2} \approx 1.5 \text{ for } 100 \ll N, \tag{3.20}$$

as shown by the dashed line. (The index $\star$ indicates that we refer to the total chain.) This value agrees of course with the ratio $(R_e/R_g)^2 = (b_N(\rho)/b_g(\rho))^2 \approx 5.3 < 6$ seen in panel (a). If on the other hand the effective segment size b_e is obtained from the internal distances this yields

$$b_e \approx R_e(s)/s^{1/2} \approx 1.6 \text{ for } 100 \ll s \ll N, \tag{3.21}$$

as indicated by the top solid line. Since in this s-regime Eq. (2.12) holds we obtain accordingly $(b_e(\rho)/b_g(\rho))^2 \approx 6$. The same holds for all densities where sufficiently long chains are available ($N \gg s \gg g$). Note that the integral over s' in Eq. (2.11) is dominated by subchains with $s' \approx s/2$ and that thus large subchains of order $s' \approx N$ are less relevant for the gyration radius of the total chain $R_g(s = N)$. Hence, the non-monotonous behavior observed for $R_e(s)$ should be barely detectible for the radius of gyration in agreement with Eq. (3.19).

That a naive fit of b_e from the total chain end-to-end distance $R_e(N)$ leads to a systematic *underestimation* of the effective segment size of asymptotically long chains is a well-known fact for 3D melts.[33] However, both estimations of b_e merge for 3D melts if sufficiently long chains are computed as may be seen from Eq. (86) and Fig. 23 of ref.[33] Apparently, this is not the case in 2D since if $R_e(s)$ or $R_e^2(s)/s$ are plotted as a function of $x = s/N$ (not shown) a nice scaling collapse of the data is obtained for large x and for $N \geq 256$, i.e.

$$\frac{R_e(s)}{b_e s^\nu} \approx \tilde{f}(x) \text{ with } \tilde{f}(x) = \begin{cases} 1 & \text{if } x \ll 1 \\ b_N/b_e & \text{if } x \to 1. \end{cases} \tag{3.22}$$

Hence, chain end effects do *not* scale away with $N \to \infty$ as they do in 3D.

A simple qualitative explanation for Eq. (3.22) is in fact readily given by considering an ideal chain of bond length b_e squeezed into a more or less spherical container of size $R_c \sim N^{1/2}$. For $s \ll N$ it is unlikely that the subchain interacts with the container walls and $R_e(s) \approx b_e s^{1/2}$. With $s \to N$ the chain will feel increasingly the confinement reflecting it back from the walls into the center of the container reducing thus the effective segment length b_N associated with the chain end-to-end distance. Since the scaling function $\tilde{f}(x)$ must be universal, it should be possible to express the ratio b_N/b_e — and thus the ratio $R_e(N)/R_g(N) = b_N/b_g$ — in terms of the dimension d and the exponents θ_0, θ_1 and θ_2. The *two* statistical segment sizes b_e and b_N should thus be related. At present we are still lacking a solid theoretical proof for the latter conjection.

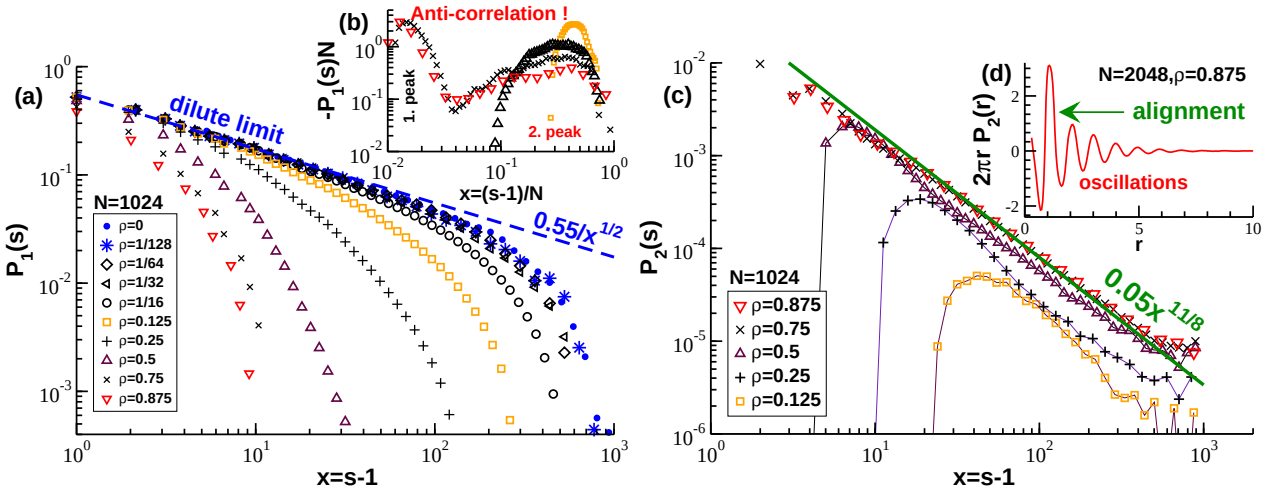

Figure 3.10: Intrachain angular bond correlations *vs.* arc-length s for chains of length $N = 1024$ and a broad range of densities: **(a)** As expected from Eq. (2.13) and the swollen chain statistics in the dilute limit the first Legendre polynomial $P_1(s)$ approaches with decreasing density $P_1(s) \approx +1/s^{1/2}$ (dashed line). **(b)** The bonds are anticorrelated for larger $s \gg g$. At higher densities there is a first peak at $s \approx 10N^0$ due to the local wrapping of the chains. A second peak is visible at $s \approx N/2$ as expected from the discussion in Sec. 3.3.2. **(c)** $P_2(s)$ probes the return probability $p_r(s)$ and approaches thus with increasing density a slope $P_2(s) \approx 1/s^{11/8}$ (bold line). **(d)** $2\pi r P_2(r)$ oscillates strongly with an exponentially decreasing amplitude. Being dominated by a nematic peak at the origin ($r \approx 1$) it acts as a δ-function.

3.3.3 Intrachain angular correlations

First Legendre polynomial. As explained in Sec. 2.3 the first Legendre polynomial $P_1(s) \equiv \langle \underline{e}_n \cdot \underline{e}_m \rangle$ has been shown to be of particular interest for characterizing the deviations from Gaussianity in dense 3D polymer solutions.[33] $P_1(s)$ is presented in panel (a) and panel (b) of Fig. 3.10 for different densities keeping the chain length constant ($N = 1024$).

As one expects from Eq. (2.13) and the swollen chain statistics in the dilute limit where $\nu = \nu_0 = 3/4$ the data approach with decreasing density the power law $P_1(s) \approx +1/s^{1/2}$ indicated by the dashed line. Please note the strong finite-N corrections to the asymptotic power law even for our single chain simulation indicated by the filled spheres ($\rho = 0$) due to the fact that chains are quite generally less swollen at their ends.[102] Using the exact relations Eq. (2.13) and Eq. (2.11) this is consistent with and explains in turns the strong finite-N effects for the ratio $(R_e(N)/R_g(N))^2$ shown in Fig. 3.9(a) for the dilute limit.[103]

The bonds remain of course aligned, $P_1(s) > 0$, if the structure within the blobs is probed ($s \ll g$) at finite densities. Interestingly, the bonds becomes *anti-correlated* for larger arc-lengths as may be better seen from panel (b) where we have plotted $-P_1(s)N$ as function of $x = (s-1)/N$. For larger densities two peaks are clearly visible. The first anti-correlation peak seen in panel (b) is due to the local backfolding of the chain contour caused by the packing of the monodisperse beads which can be directly seen from chain 1 drawn in Fig. 3.2(a). More importantly, there is a second peak for all densities and sufficiently long chains. Using Eq. (2.13) this peak corresponds exactly to the scaling expected from Eq. (3.22) with an associated universal function scaling as $-\partial_x^2(x\tilde{f}(x))$. Following the discussion at the end of Sec. 3.3.2 a peak at $s \approx N/2$ is expected due to the confinement of the chain which causes long segments to be reflected back. We stress however that altogether this is a rather small effect and essentially $P_1(s) \approx \partial_s^2 R_e^2(s) \approx 0$ for $s \gg g$. Hence, the first Legendre polynomial confirms that to leading order $2\nu \approx 1$ in the compact chain limit.

Second Legendre polynomial. More relevant for the focus of this chapter is the scaling observed for the second Legendre polynomial $P_2 \equiv \langle (\underline{e}_n \cdot \underline{e}_m)^2 \rangle - 1/2$ presented in panel (c) and (d) of Fig. 3.10. In

the latter panel (d) the second Legendre polynomial is plotted for one configuration with $N = 1024$ and $\rho = 0.875$ as a function of the distance r between the mid-points of both bonds. Averages are taken over all intrachain bond pairs with $[r, r + \delta r]$ using a bin of width $\delta r = 0.01$. The vertical axis is rescaled with the phase volume $2\pi r$. As can be seen, the orientational correlations oscillate with r and this with a rapidly decaying amplitude. (These oscillations are related to the oscillations of the pair correlation function at high densities and reflect the local packing and wrapping of chains composed of discrete spherical beads.) Due to the oscillations and (more importantly) the decay, only bond pairs at $r \approx 1$ matter if we compute $P_2(s)$, i.e. if we sum over all distances r at a fixed curvilinear distance s as shown in panel (c). $P_2(s)$ thus probes essentially the return probability $p_{\rm r}(s)$ of the chain after s curvilinear steps. Following Eq. (3.17) one thus expects

$$P_2(s) \approx w(\rho) \times p_{\rm r}(s) \approx w(\rho)/s^{1+\nu\theta_2}, \tag{3.23}$$

where $w(\rho)$ characterizes the s-independent local and non-universal alignment effect given that two bonds are close to each other. This is confirmed by our data which is seen to approach with increasing density a power law $P_2(s) \approx +1/s^{11/8}$ (bold line).

3.3.4 Chain shape

As obvious from Fig. 3.2 the compact chain conformations are neither perfectly spherical nor extremely elongated. Having discussed above the chain size we address now the chain shape as characterized by the average *asphericity* of the gyration tensor. (For definitions see Sec. 2.3.) In the compact chain limit the "aspect ratio" of the gyration tensor eigenvalues is found to approach

$$\langle\lambda_1\rangle : \langle\lambda_2\rangle \approx 4.5 : 1 \tag{3.24}$$

for our longest chains which corresponds to a reduced principal eigenvalue $\langle\lambda_1\rangle / R_{\rm g}^2 \approx 0.8$.[46] It should be noted that Gaussian chains and dilute good solvent chains in 2D are characterized[104] by an aspect ratio $\langle\lambda_1\rangle / \langle\lambda_2\rangle \approx 5.2$ and 6.3, respectively. (The latter value stems from our own MC simulations for dilute SAW up to $N = 8192$[103] which is slightly lower than the value given in the literature[104]). High-density chains are thus clearly less elongated.

Motivated by experimental work on DNA molecules investigated using fluorescence microscopy[105] the asphericity of the inertia tensor of 2D objects may be further characterized by computing the moments Δ_1 and Δ_2 defined in Sec. 2.3.[80,81,104,105] Obviously, $\Delta_1 = \Delta_2 = 1$ for rods and $\Delta_1 = \Delta_2 = 0$ for spheres. As indicated by the thin horizontal lines in Fig. 3.11, it is known for Gaussian chains in two dimensions that $\Delta_1 \approx 0.68$ and $\Delta_2 = 2(d+2)/(5d+4) \approx 0.57$.[80,104]

Our data for Δ_1 and Δ_2 is represented in Fig. 3.11 as a function of the reduced chain length N/g. This allows to collapse data for a broad range of densities on two respective master curves. In agreement with Yethiraj[72] the asphericity is found to decreases systematically with increasing chain length and density, i.e. the chains become more spherical the more we enter the compact chain regime. As one expects, plateau values are approached in the dilute limit and the compact chain limit indicated, respectively, by dashed and bold lines. The indicated values for the dilute limit $\Delta_1 \approx 0.72$ and $\Delta_2 \approx 0.62$ have been taken from our single chain MC simulations ($\rho = 0$)[103] which are again similar to previous numerical and experimental data.[81,104,105] Unfortunately, in the opposite limit the precise plateau values for asymptotically long chains are yet unknown and the presented lines with $\Delta_1 \approx 0.63$ and $\Delta_2 \approx 0.51$ are merely guides to the eye. (Yethiraj[72] indicates $\Delta_2 = 0.52$ for $N = 256$ which agrees reasonably with our estimation.) We emphasize that in any case these plateau values are *below* the corresponding predictions for Gaussian chains, i.e. the chains become clearly more spherical.

3.3.5 Interchain monomer pair distribution function

Predictions. As defined in Sec. 3.3.2 the contact exponent θ_2 characterizes the intrachain subchain size distribution $G_{\rm e}(r,s) \approx G_2(r,s)$ for small arc-lengths $s \ll N$ and distances $r \ll R$. It has been argued recently[48,66] that θ_2 should also be relevant for describing interchain monomer contacts. As illustrated in

Figure 3.11: Chain asphericity for different densities as a function of reduced chain length N/g in log-linear coordinates using the same symbols as in Fig. 3.3. The horizontal axis is rescaled using Eq. (3.16) for the number of monomers per blob $g(\rho)$. Since strong finite-N effects are again observed in the dilute limit, only the three largest chain lengths are given for $\rho < 0.0625$. The asphericity is characterized by the moments Δ_1 and Δ_2 of the eigenvalues λ_1 and λ_2 of the inertia tensor, Eq. (2.16). Both moments decay with increasing chain length and density, i.e. the chains become more spherical. The thin lines correspond to the prediction for Gaussian chains,[80,104] the dashed lines to the plateau values in the dilute limit[103] and the bold lines to suggested values for long compact chains.[46,72] Even longer chains and, more importantly, better statistics are required to seddle the latter limit.

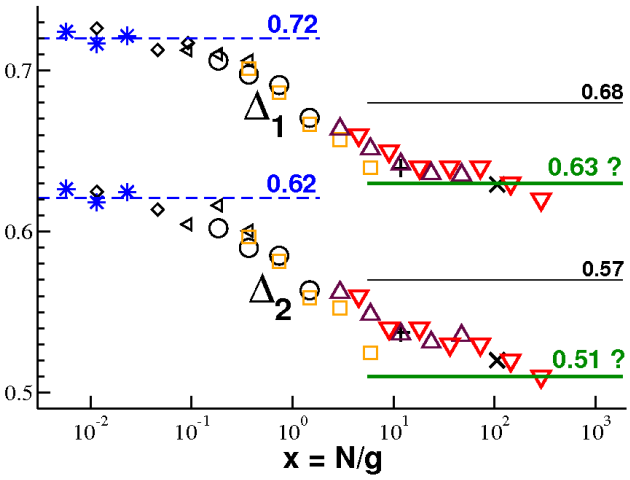

Fig. 1.5 this scaling argument states that it is irrelevant of whether the neighborhood at $r \ll R$ around the reference monomer is penetrated by a long loop of the same chain or by another chain with a center of mass at a typical distance R. The radial pair distribution function $g_{\rm int}(r)$ between monomers from different chains should thus scale as

$$g_{\rm int}(r)\rho \approx G_2(r, s \approx N) \times N \times \underline{R^d \rho / N} \tag{3.25}$$

where the second factor N stems from the fact that it is irrelevant which monomer of the second chain is probed.[106] (By normalization $g_{\rm int}(r) \to 1$ for $r \gg R$ for all densities.) Note that the underlined term characterizing the probability for having a second chain close to the reference chain drops out in the compact chain limit where Eq. (3.3) holds. It follows from Eq. (3.17) for $i = 2$ and Eq. (3.25) that

$$g_{\rm int}(r) \approx (r/R)^{\theta_2} \sim 1/N^{\nu\theta_2} \text{ for } r \ll R \tag{3.26}$$

as indicated in panel (b) by dashed and bold solid lines for, respectively, the dilute limit and the melt limit.

Numerical confirmation. To test these predictions we have computed $g_{\rm int}(r)$ for a broad range of densities.[48] Using double-logarithmic coordinates the data has been traced in panel (a) of Fig. 3.12 as a function of the reduced distance $x \equiv r/R_{\rm g}$. In agreement with Eq. (3.26) the same exponents θ_2 are observed for $x \ll 1$ as for the intrachain subchain size distribution $G(r, s) \approx G_2(r, s)$ for $s \ll N$: $\theta_2 = 19/12$ in the dilute limit (dashed line) and $\theta_2 = 3/4$ in the compact chain limit (solid line). Please note that the data representation is again motivated by the density limits where the chain size is the only relevant length scale, i.e. data collapse is not expected in the semi-dilute regime. The scaling with respect to chain length N for small distances r indicated in Eq. (3.26) is successfully verified by comparing different chain lengths N at the same density ρ as shown in panel (b) of Fig. 3.12 for $\rho = 0.875$. The distributions $g_{\rm int}(r)$ have been sampled here using linear r-bins to emphasize that, as one expects, the standard oscillations of the monomer-monomer pair-correlations are observed for small distances r at high densities. Interestingly, being caused by non-local correlations the predicted N-scaling $g_{\rm int}(r) \sim 1/N^{3/8}$ still holds in the high-ρ limit where $g \to 0$. Please note that the peak structure disappears rapidly with decreasing density (not shown).

3.3.6 Interchain binary monomer contacts

In order to characterize more systematically the density crossover from the dilute limit over the semidilute regime up to dense melts we focus now on $g_{\rm int}(r \approx a)$ with a being one fixed monomeric distance for all densities. For the data presented in Fig. 3.13 we have determined the typical number $n_{\rm int}$ of interchain

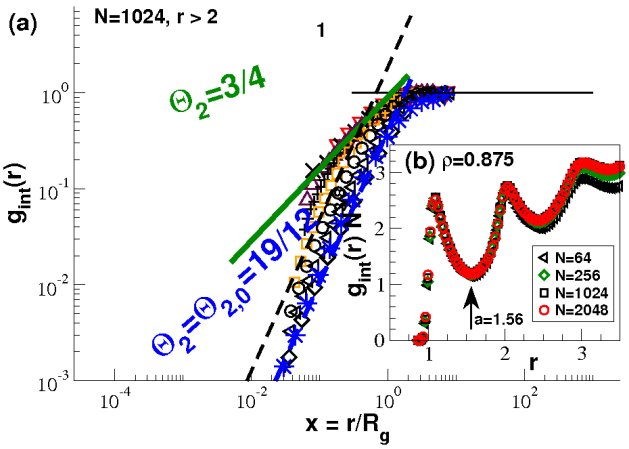

Figure 3.12: Connection between intrachain and interchain contact probability: **(a)** Numerical data for $N = 1024$ and $r > 2$ for different densities ρ using the same symbols as in Fig. 3.6. The logarithmically binned results are traced as a function of the reduced distance $x = r/R_g$. Due to the additional length scale $\xi(\rho)$ in the semidilute density regime, data collapse is only observed for very low dilute densities and high melt densities. **(b)** Scaling collapse of $g_{\rm int}(r)N^{3/8}$ for small distances r for the melt density $\rho = 0.875$ confirming the predicted scaling $g_{\rm int}(r) \sim 1/N^{\nu\theta_2}$ in this limit. The cut-off parameter $a = 1.56$ used for the determination of the typical interchain monomer contact number $n_{\rm int}$ is indicated by the arrow.

monomer contacts for a reference monomer by integrating $g_{\rm int}(r)\rho$ up to a cut-off $a = 1.56$. The raw data obtained for several densities is presented in panel (a) which is (of course) seen to scale with N as the interaction energy, $\beta e_{\rm int} \approx n_{\rm int}$, between monomers from different chains discussed in Fig. 3.3 above. (Values for $N = 1024$ are given in Table 2.1.) The specific value used for a is motivated by the first minimum of the pair distribution function which varies only weakly with ρ. It turns out that for not too high densities the scaling of $n_{\rm int}$ is robust under variation of a. The quality of the ρ-scaling (but not of the scaling with respect to N) depends somewhat on a for $\rho \geq 0.75$ where the blobs become too small and additional physics due to the discrete beads becomes relevant as one expects from our discussion of the thermodynamic properties (Sec. 3.2). The cut-off parameter a is essentially a useful tuning parameter allowing to improve the scaling collapse for the highest (experimentally less relevant) densities. It is satisfactory, however, that it is possible to improve the scaling with just one physically transparent parameter.

Using a similar representation as in Fig. 3.6 for the chain size, we present in panel (b) of Fig. 3.13 the rescaled number of interchain contacts $n_{\rm int}$ as a function of the reduced chain length N/g for different densities and in panel (c) as a function of the reduced density ρ/ρ^* for different chain lengths. The rescaling used for the vertical axes is readily obtained by matching at $N/g \approx (\rho/\rho^*)^2 \approx 1$ the power-law results implied by Eq. (3.26) for the dilute ($\nu\theta_2 = 19/16$) and compact ($\nu\theta_2 = 3/8$) limits. This implies for the latter limit (solid bold lines)

$$n_{\rm int} \approx \frac{\rho a^d}{g^{\nu_0\theta_{2,0}}} \times (N/g)^{-\nu\theta_2} \tag{3.27}$$

where the first factor corresponds to the fraction of monomers of a given blob interacting with monomers from other chains given that the blob is at the chain perimeter. The second term $(N/g)^{-\nu\theta_2} = (N/g)^{-3/8}$ stands for the fraction of blobs of a chain interacting with other chains. Eq. (3.27) implies the ρ-scaling observed in panel (b) of Fig. 3.3 for the interaction energy $e_{\rm int} \sim \rho^{21/8}$ in the semidilute regime. The scaling seen in Fig. 3.13 implies that in the compact chain limit the perimeter P scales as[107]

$$P/\xi \approx (N/g)^{1-\theta_2/d} \tag{3.28}$$

where the ρ-scaling only holds rigorously (without tuning parameter) in the semidilute regime. Since on the other hand $P/\xi \approx (R/\xi)^{d_{\rm p}} \approx (N/g)^{d_{\rm p}/d}$, this implies a fractal line dimension $d_{\rm p} = d - \theta_2 = 5/4$, generalizing thus the numerical result obtained for the melt limit[46] to the broader compact chain limit.

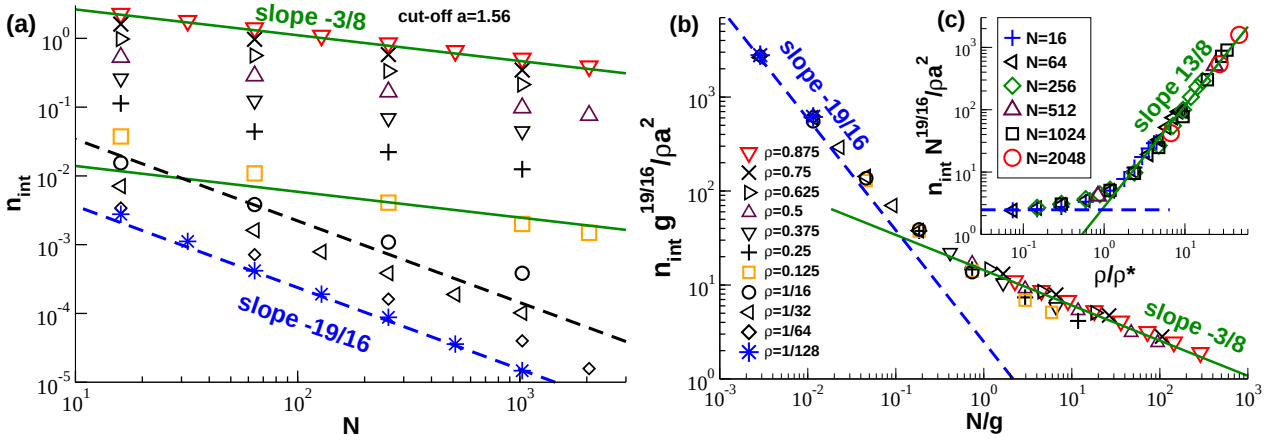

Figure 3.13: Average interchain monomer contact number $n_{\rm int}$ obtained from the interchain monomer pair-distribution function $g_{\rm int}(r)$ assuming a cut-off distance $a = 1.56$ and using the same symbols as in Fig. 3.6: **(a)** unscaled $n_{\rm int}(N)$ for different densities, **(b)** scaling plot with respect to reduced chain length N/g for different densities and **(c)** scaling plot with respect to reduced density ρ/ρ^* for different chain lengths. The dashed lines correspond to the exponent $\nu\theta_2 = 19/16$ for dilute chains, the full lines to $\nu\theta_2 = 3/8$ for the compact limit. The observed data collapse confirms Eqs. (3.26) and (3.27).

3.4 Reciprocal space properties

3.4.1 Intramolecular form factor $F(q)$

In Sec. 2.3.2 we reviewed already the "generalized Porod law"[82,84,85] and the theoretical predictions for the intramolecular form factor $F(q)$. These predictions are compared to our numerical results in Fig. 3.14 for different densities and chain lengths. The thin lines indicated correspond to the Gaussian chain behavior and the bold solid lines to our key prediction Eq. (3.8). Obviously, $F(q) \to N$ for $q \ll R_{\rm g}$ as may be seen from panel (a) presenting the unscaled form factor $F(q)$ for one chain length, $N = 1024$, and a broad range of densities. As indicated by the dashed lines we have in the intermediate wavevector regime of long dilute chains a power-law decay[103]

$$F(q) = F_0(q) = \frac{c_0}{(b_0 q)^{4/3}} \tag{3.29}$$

with a dimensionless amplitude $c_0 \approx 0.5$. The decay with q in the intermediate wavevector regimes increases systematically with increasing density. Interestingly, this decay becomes clearly stronger than the Gaussian chain power law (thin line). The Kratky representations of the form factor reveals non-monotonous behavior which increases with increasing density and chain length as shown, respectively, in panel (b) and (c). As shown in the latter panel (c) for one density with $N \gg g$, the form factor is found to become N-independent only in the limit of very large wavevectors. This is quite generally an important indicator for a (generalized) Porod scattering behavior as discussed in paragraph 2.3.2.

Motivated by the scaling expected for very large chains of blobs, the last panel (d) presents the rescaled form factor $(F(q)/N)Q^2$ as a function of the reduced wavevector $Q = qR_{\rm g}$. The filled symbols refer to data for $N = 2048$, all other symbols to $N = 1024$. At variance to the indicated Debye formula for Gaussian chains a strong nonmonotonous behavior is revealed by our data, which approaches with increasing ρ and N a power-law exponent $-\theta_2 = -3/4$ given by the bold solid line, Eq. (2.38). Please note that the power-law amplitude used has been determined in the preceeding paragraph. Our complete theoretical prediction Eq. (2.36) for asymptotically long chains using the Redner-des Cloizeaux approximation is given by the thin solid line. Without any adjustable parameter it allows to fit successfully the data starting from the Guinier regime for small wavevectors up to $Q \approx 10$ for our largest densities and chain lengths. Our numerical data presented in Fig. 3.14 agree thus with the theoretical prediction of compact chains of blobs of fractal

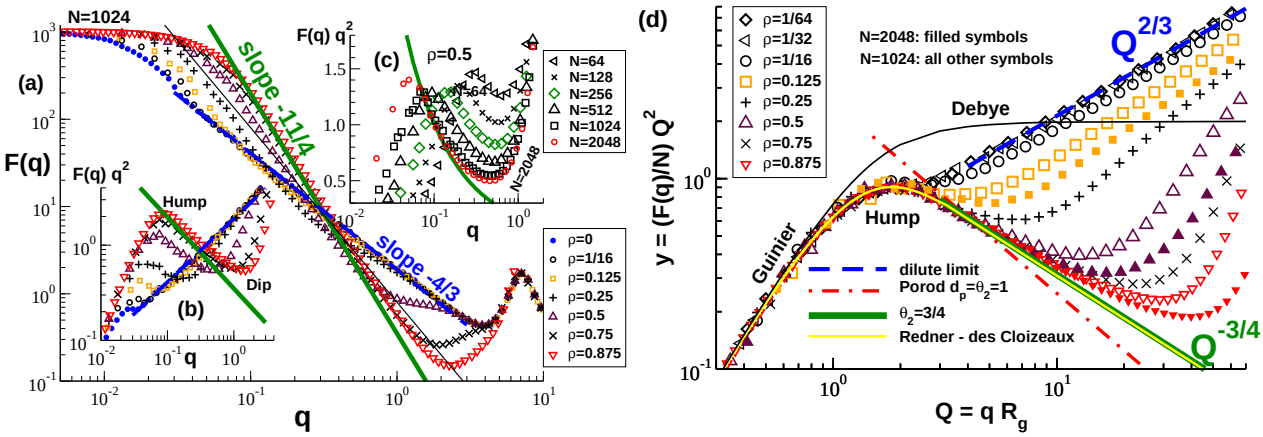

Figure 3.14: Various representations of the intramolecular form factor $F(q)$ for different densities ρ and chain lengths N: **(a)** $F(q)$ *vs.* wavevector q for $N = 1024$ and a broad range of densities. The dilute swollen chain limit with $F(q) \sim 1/q^{1/\nu_0}$ is represented by the dashed line, the Gaussian chain $F(q) \sim 1/q^2$ by the thin line and the power law for compact chains of fractal contour, Eq. (3.8), by the bold line. **(b)** The Kratky representation of the same data reveals with increasing density a more and more pronounced non-monotonous behavior. **(c)** The non-monotonous behavior becomes also more striking with increasing chain length as shown here for one intermediate density, $\rho = 0.5$. The form factor becomes only N-independent on the monomeric scale. **(d)** Kratky representation of $y = (F(q)/N)Q^2$ *vs.* reduced wavevector $Q = qR_g$. Filled symbols refer to $N = 2048$, all other symbols to $N = 1024$. The Debye formula is indicated by the top thin line, the Porod scattering for a compact 2D object with smooth perimeter by the dash-dotted line and the power-law exponent $-\theta_2 = -3/4$ by the bold solid line. Our prediction for asymptotically long chains, Eq. (2.36), allowing a fit starting from the Guinier regime for small wavevectors, is given by the thin solid line.

contour perimeter.[65,66] Obviously, much larger chains than computationally feasible at present are required to confirm numerically the predicted perimeter dimension only from the decay of the form factor.

3.4.2 Total monomer structure factor $S(q)$

As already discussed in Sec. 3.2.3, the isothermal compressibility of the solution may be obtained from the plateau of the structure factor in the low-q limit according to Eq. (3.7). The smallest possible wavevector is of course $2\pi/L_{\rm box}$ since the wavevector q must be commensurate with the simulation box of linear dimension $L_{\rm box}$. As can be seen in panel (a) of Fig. 3.15 our box sizes allow for a precise determination of $g_{\rm T,N}(\rho)$ for all densities $\rho \geq 0.0625$. Only chains of length $N = 1024$ are presented for clarity. Note that above $q > 3$ the monomer structure becomes important for all densities and, being interested in universal physics, we focus below on smaller wavevectors. For comparison, we have also included the structure factor $S(q) = F_0(q)$ for one single chain in a large box ($\rho = 0$). We remind that the "random phase approximation" (RPA)[33,59]

$$\frac{1}{S(q)} = \frac{1}{g_{\rm T}} + \frac{1}{F(q)} \tag{3.30}$$

is supposed to relate — at least for not too high densities — the total structure factor $S(q)$ to the dilute chain form factor $F(q) \approx F_0(q)$ for $q \gg 1/\xi$.[33,59] Note that $g_{\rm T}$ stands for the excess contribution to the dimensionless compressibility in agreement to Eq. (3.12) and to $1/F(q) \to 1/N$ in the low-q limit. By construction $S(q)$ is well fitted by the RPA for very small and large wavevectors as shown by the thin solid line for $\rho = 0.125$. Please note that even for low densities the crossover regime between both q-limits at $q \approx 1/\xi$ is, however, only inaccurately described. The monotonous decay of $S(q)$ implicit to Eq. (3.30) is

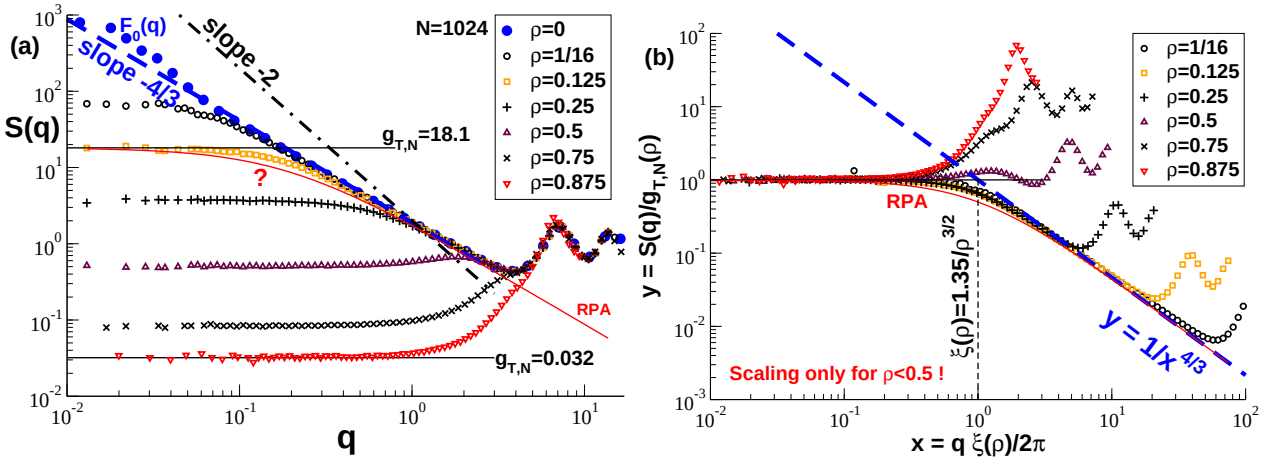

Figure 3.15: Total monomer structure factor $S(q)$ for $N = 1024$ for a broad range of densities ρ: **(a)** $S(q)$ as a function of wavevector q. In the dilute limit ($\rho \ll \rho^*$) $S(q)$ corresponds to the single chain form factor $F_0(q)$ indicated by filled spheres. The plateau values in the low-q limit at finite densities have been used for the determination of $g_{T,N}(\rho)$ as shown for $\rho = 0.125$ and $\rho = 0.5$ (thin horizonal lines). Local physics is observed for $q > 3$. At smaller wavevectors $S(q)$ is found to decay monotonously only for densities $\rho < 0.5$. At higher densities $S(q)$ increases with q at qualitative variance to the RPA formula, Eq. (3.30), indicated by the thin solid line. **(b)** Rescaled structure factor $y = S(q)/g_{T,N}(\rho)$ as a function of reduced wavevector $x = q\xi(\rho)/2\pi$. Assuming Eq. (3.16) for the blob size ξ, the asymptotic small-q (horizontal line) and large-q (bold dashed line) limits match at $x \approx 1$ as indicated by the vertical dashed line.

indeed observed for the semidilute densities with $\rho < 0.5$. For higher densities, where the blob picture breaks down due to monomer physics, $S(q)$ becomes essentially constant for all q up the monomeric scale.

The scaling of $S(q)$ in the semidilute regime is further investigated in panel (b) of Fig. 3.15 where $y = S(q)/g_{T,N}$ is traced as a function of $x = q\xi/2\pi$ with $\xi = b_0 g^{\nu_0}$ being set by the matching of the radius of gyration in the dilute and semidilute limits, Eq. (3.16). As indicated by the vertical dashed line the asymptotic slopes for small and large wavevectors are found to intercept at $x \approx 1$. Using Eq. (3.29) for the dilute chain form factor this matching implies $\xi = b_0 2\pi (g_T/c_0)^{\nu_0}$. The number of monomers per blob g thus may be obtained in the semidilute regime from the dimensionless compressibility g_T using $g \approx 23 g_T$ in agreement with Eq. (3.16). Our slightly arbitrary prefactor setting thus corresponds to a reasonable choice. It also suggests that experimental work should proceed in a similar manner by fixing ξ (or equivalently g) from the matching point of both q-limits of the total structure factor rather than by imposing an inappropriate Ornstein-Zernike fit to the intramolecular form factor.[17]

Chapter 4

Semiflexible Polymers

4.1 Introduction

In our work we have considered so far chains that are flexible down to the monomer scale. This is obviously an idealized limit since most of the experimentally relevant macromolecules display a finite rigidity.[16, 17, 22] Following previous computational work[39, 56, 108] we are currently investigating the scaling behavior of semiflexible 2D chain solutions, from the dilute limit[39] up to high densities, in order to detect how a finite persistence length may change the system behavior. This short chapter sketches our first conclusions from the analysis of the numerical simulation results obtained so far, paving the way for later, more detailed studies of semiflexibility effects in strictly two dimensional polymer systems.

Semiflexibility is readily included in our model by the stiffness potential $\mathcal{H}_{angle} = k_\theta(\theta - \theta_0)^2$ between adjacent bonds along the chain contour with θ being the angle between the bonds, θ_0 the angle in the ground state conformation and k_θ the energy difference between orthogonal and perfectly aligned bonds.[109] In this chapter we assume $\theta_0 \equiv 0$ i.e. the chains do not have any spontaneous curvature.

We present in Fig. 4.1 snapshots of chain conformations in simulated systems at four densities, increasing from left to right and five rigidities incremented from bottom to top. The configurations have been sampled gradually increasing k_θ starting with flexible systems ($k_\theta = 0$). While the chains remain compact and segregated at low densities and stiffnesses below the dashed line, they are seen in the opposite limit to align (at least) locally.

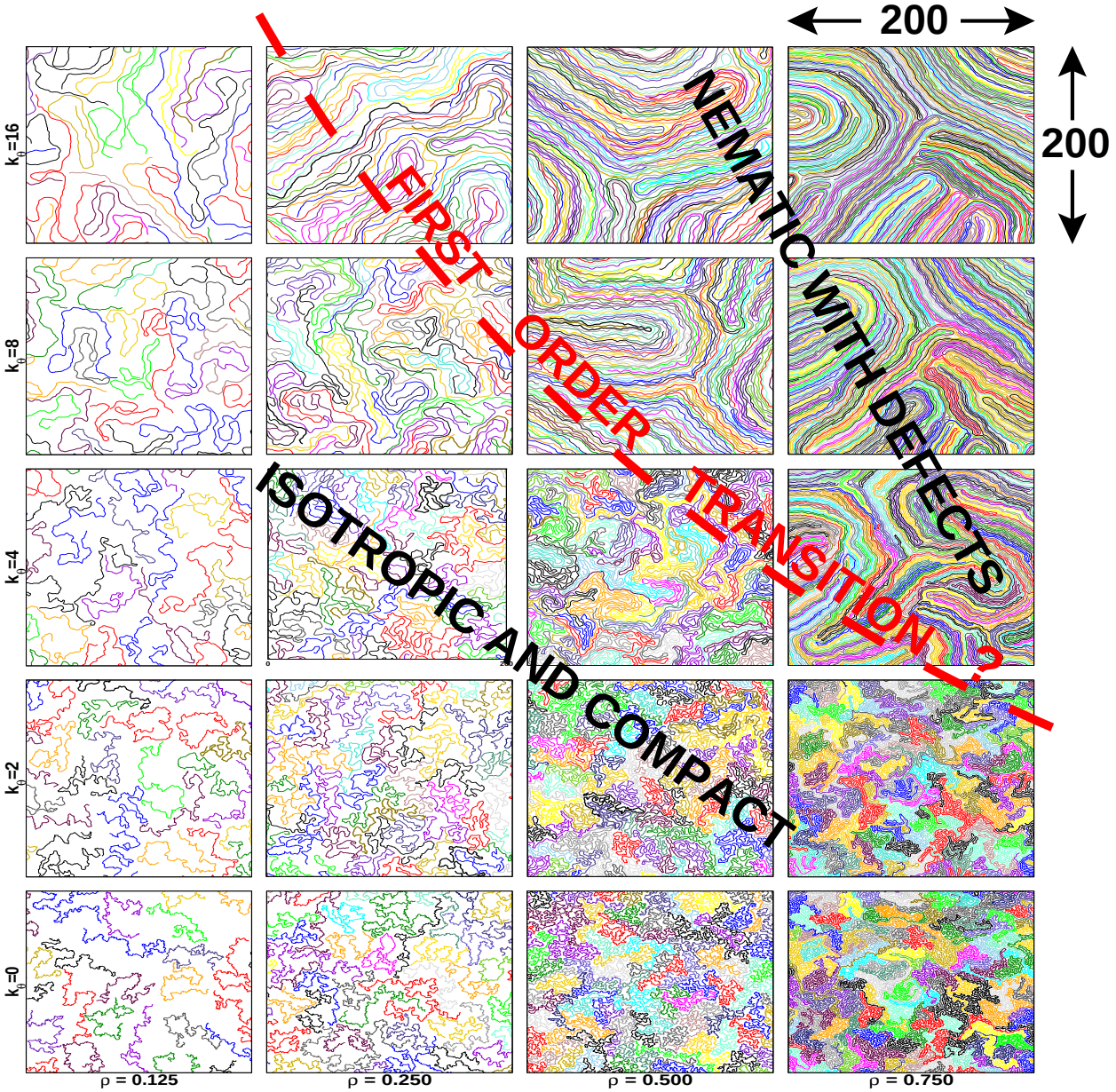

Figure 4.1: Snapshots of semiflexible 2D polymers of length $N = 256$ for four densities $\rho = 0.125$ ($M = 192$, $L_{\rm box} \approx 627$), $\rho = 0.250$ ($M = 192$, $L_{\rm box} \approx 627$), $\rho = 0.500$ ($M = 192$, $L_{\rm box} \approx 313$), and $\rho = 0.750$ ($M = 384$, $L_{\rm box} \approx 362$) and five bending penalties $k_\theta = 0$, 2, 4, 8 and 16 (from the bottom to the top). The configurations have been sampled gradually increasing k_θ starting with flexible and compact chain systems ($k_\theta = 0$). While the chains remain compact and segregated at low densities and stiffnesses below the dashed line, they are seen in the opposite limit to align (at least) locally forming bundle of chains with hairpins which are extremely difficult to equilibrate. With more computer time a regular long-ranged nematic phase (with few defects) is expected, however, as already verified using shorter chains.

4.2 Weak persistence length effects

The effect of this potential is best characterized first for the dilute limit, where the curvilinear persistence length $l_p \equiv l s_p$ can be extracted from the exponential decay of the bond-bond correlation function $P_1(s) \sim \exp(-s/s_p)$,[39, 103] the bond length l can be regarded as constant for all k_θ and ρ. As for the flexible systems, a blob size ξ and the number of units g in a blob can still be defined for small enough rigidities and densities. More precisely, renormalized flexible behavior is expected[59] as long as the persistence length remains smaller than the number of monomers in a blob, $s_p \leq g(k_\theta)$. We found indeed that for the experimentally mainly relevant low and moderate densities, the finite rigidity does not change qualitatively the scaling properties discussed in the previous chapters. In fact, since according to Eq. (3.6) the blob size decreases rapidly with stiffness, a finite rigidity speeds up the convergence to the predicted compact chain limit.

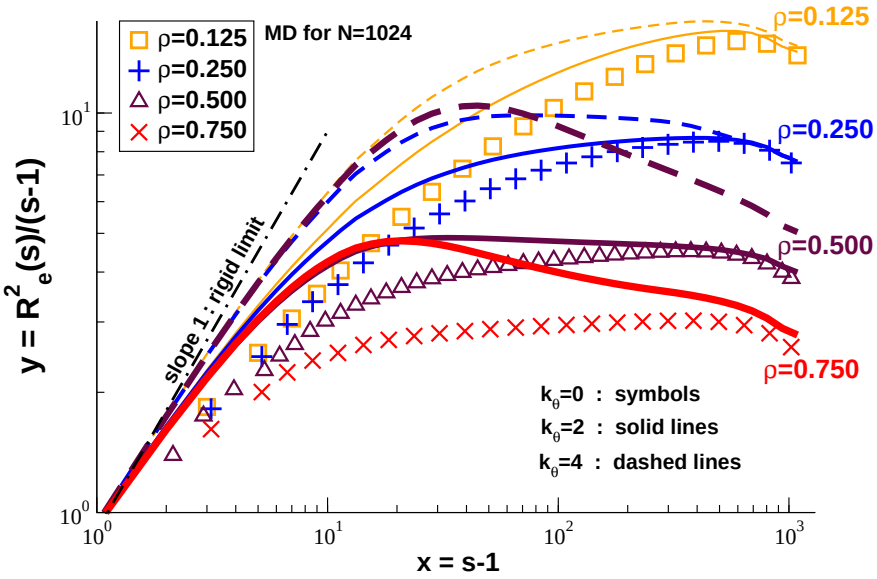

Figure 4.2: Rescaled subchain size distribution $y = R_e^2(s)/(s-1)$ for four densities and three stiffness penalties corresponding to systems below the dashed line in Fig. 4.1. The symbols refer to flexible systems ($k_\theta = 0$); the line width for $k_\theta = 2$ and 4 increases with density. The dash-dotted line corresponds to the asymptotic slope for perfectly rigid chains. Note that $y(s)$ becomes strongly non-monotonous with increasing k_θ. However, as long as the system remains isotropic, i.e. k_θ is not too large, the reduced chain lengths for a given density become similar for large arc-length s. Independent on the local rigidity the overall subchain size is thus ruled by the — persistence length independent — distance $d_{cm} \approx (s/\rho)^{1/d}$ between subchain center of masses.

As shown from the reduced subchain size $R_e^2(s)/(s-1)$ for different k_θ presented in Fig. 4.2, the subchain size depends in fact very little on the local persistence length for large arc-lengths $s \to N$. In this limit the chain and subchain size is essentially set by the persistence length independent distance $d_{cm} \approx (s/\rho)^{1/d}$ between subchains.

An independent confirmation that renormalized semi-dilute scaling holds for these 2D solutions, is provided by the properties of the pressure shown in Fig. 4.3. As the figure shows, the pressure depends on the third power of the density for a fair range of the chain rigidity, for small enough densities. The semidilute power law is mainly limited by the fact that the presented chainslength $N = 256$ is rather short and, hence, the dilute scaling $\beta\rho \sim \rho/N$ is seen for densities $\rho < 0.1$. Larger chaind and smaller densities at finite persistence length are required in order to check the scaling of the blob size with ℓ_p stated above.

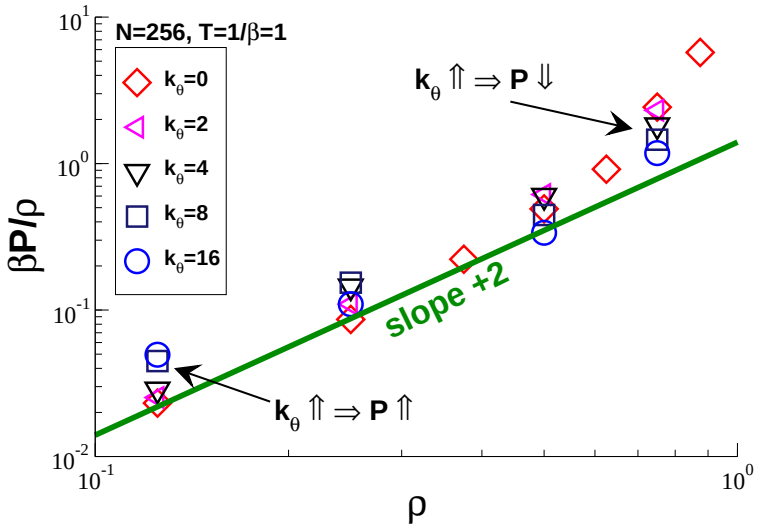

Figure 4.3: Total pressure βP as a function of density ρ for $N = 256$ and several stiffness energy penalties k_θ as indicated. Small deviations from the, globally holding, standard scaling behavior for flexible chains $P \propto \rho^3$ can be seen when increasing density and rigidity. In agreement with previous computational findings[26] the pressure $P(k_\theta)$ is found to increase with k_θ for low densities but *decreases* for high densities due to the (albeit incomplete and only local) isotropic-nematic ordering transition.

4.3 Isotropic-nematic transition

The chain solution cannot any longer be viewed as a semidilute solution of flexible chains with a renormalized monomer size when the persistence length, estimated by extrapolation to finite densities using the conformational properties of the dilute limit, exceeds strongly the blob size. In this limit a transition to an ordered nematic state with increasing persistence length and density is observed as can be seen from the snapshots of Fig. 4.1.

Theoretical studies, focusing on semiflexible polymer chains of a fully occupied Flory lattice model, confined to a volume of fixed shape,[41,42] suggest that this transition is continuous, but Monte Carlo simulations of multichain systems at a fixed finite density[56] point to first order changes. We have not so far precisely determined the order of the transition nor its precise location on the [k,ρ] diagram of state. Notwithstanding, the analysis of the numerical simulations that we performed so far, suggests a first order nature of the transition as discussed below.

The data presented in Fig. 4.1 and Fig. 4.2 stems from systems where we start with our compact and segregated chain conformations of flexible chains ($k_\theta = 0$) and increase gradually the bending penalty. Additionally, a second set of data has been obtained starting with aligned rods at high k_θ decreasing then gradually the stiffness. (This data set is limited up to now to short chains of length $N \leq 256$.) While for systems below the dashed line in Fig. 4.1 the same chain conformations are readily reached with both dynamical pathways for all chain lengths available, this becomes computationally challenging around and above the dashed line, i.e. strong *hysteresis effects* have been clearly observed. Due to the sluggish hairpin-like defects seen in the snapshots the hysteresis might be of course a merely dynamical issue. However, for all systems for which both dynamical pathways yield the same configurational properties, i.e. where we are sure to have reached equilibrium, a sharp transition between isotropic and nematic state has been observed for the standard nematic order parameter S,[79] the reduced system size $R_e(N)/N$ or the second Legendre polynomial $P_2(r)$ of intra- and interchain bonds as a function of distance r between bonds (not shown). As shall be discussed elsewhere,[110] these results strongly point to a proper first order transition[68] confirming thus the pioneering work by Baumgärtner and Yoon.[56]

Chapter 5

Athermal Fibers

5.1 Introduction

In this chapter, we move away from phenomena governed by thermal disorder and consider rather how quenched disorder, captured in frozen spontaneous shapes of individual chains or membranes, influences the collective properties of assemblies of corrugated fibers or sheets. As reviewed below, one can find in Nature and in man-made materials, many of such systems, well aligned or isotropically distributed, embedded in two or in three dimensions, see Fig. 5.1. Here we will adapt the simulation methods and data analysis tools employed in the precedent chapters, to study, for simplicity, the case where shape-quenched fibers lay in strictly two-dimensions.

Figure 5.1: Several natural and man-made systems of waving fibers and surfaces, where the imprinted non-straight or non-flat shape of individual components play a role in the final global aspect and on the global mechanical or sensorial properties. For the top left packs of paper soft tissues, for instance, a current trend in paper-making companies is to advertise progress on the packing capacity while retaining tissue fluffiness, for reduced environmental transportation costs.[111]

Disordered stacks of waving fibers: here, there, everywhere.

Beyond its interest as a raw product for the textile industry, natural wool has been for many years studied as an archetype for fluffy fibrous materials. Synthetic substitutes for wool where sought for, with the ambition of reproducing the material mechanical and insulating qualities. Extensions of such dense fiber packings for the building industry include for instance the so-called glass wool insulator. The basic constituent of such materials is a fiber or strand, of lateral dimension much smaller than length, often with a non straight, waving shape. Deformation of wads of wool can be easily obtained due to the predominance of fiber bending, which is much easier to achieve than fiber stretching or compression. For isotropic packings of straight fibers, such as needles, matches or toothpicks, bending couples to fiber contact density to determine the global compression behavior.[27] For isotropic 3D or 2D arrangements of non-straight strands, such as in natural wool, glass wool, paper and felt, the waviness of the shapes is not essential to achieve finite compressibility, but it plays a renormalizing role[112] of the bending stiffness. However, in natural or composite materials of almost aligned fibers, as for instance in hair tresses or ponytails, fluffiness can only be found in bundles of strands with non-straight spontaneous shapes – see Fig. 5.2. In these systems, the waviness spontaneous shape of the fibers allow for a finite compressibility of the fiber bundles, that would otherwise behave as a dense solid material.[113] Here below, we will explore by numerical simulations how the statistical properties of the distribution of spontaneous shapes determine bundle compressibility.

Figure 5.2: A random choice of systems with almost aligned fibers of wavy shapes. From left to right, top to bottom: a socket lock for wire ropes, that need to be properly broomed in a cone-like shape; a decorative fluffy puf of wool; a vegetal broom, with fiber details shown; a cotton-grass, eriophorum angustifolium; a ponytail and, on the bottom, several bow string silencers from different animal or vegetal fiber pufs.

State of the Art

In an attempt to explain the compressibility of wool, van Wyk[114] discussed back in the forties several available pressure-volume relations, and realized that the deformation of wool stacks was controlled mostly, under a given external load, by the bending modes of the fiber strands. Work on the compressibility of fibrous masses made from isotropically distributed fiber strands has since followed the steps of the seminal work in.[114] Recently, Kabla and Mahadevan[115] performed extension stretching experiments on felt, a material exhibiting strain stiffening and high Poisson ratios, and showed that theses properties are related to the mechanical behavior of individual fibers with quenched non-zero curvatures.

When the fibers are almost aligned, the quenched disordered shapes are key to allow for a finite compressibility of the fiber bundles or fluffs, which would otherwise display, if perfectly aligned, the high compression values of the constituent materials. This was first discussed by Beckrich *et al.*[31] which computed within a self-consistent mean-field treatment in two dimensions the compression modulus of the fiber stacks, and used this equation of state to predict the shapes of brooms and other fluffy cones made from fibers. Very recently, Goldstein *et al.*[30] studied the cylindrically symmetric 3D shape of hair ponytails and showed that they could be understood by similar arguments, albeit with a yet unexplained equation of state for the bundle internal compressibility.

Implementation of simulations for 2D non-straight fibers

As in the precedent chapters, we consider here two dimensional chains described by the Hamiltonian Eq. (1.1), with the additional feature that the fibers ground state is *not* a straight line. Instead, the spontaneous equilibrium shape of a single fiber is described by a set of non-vanishing reference angles $\{\theta_0\}$ between any three consecutive monomers, as depicted in Fig. 5.3. The angles are chosen such that the local fiber gradients remain much smaller than unity, so that fiber shapes can also be described mathematically by a single-valued function $\zeta_0(x)$.

Contrary to the precedent chapters where molecular dynamics simulation methods were used to sample the configurations as a function of time, in the present chapter, where the velocities of the coarse-grained beads can be neglected, we use the Steepest Descent (SD) method[63] to find the equilibrium, time-independent conformations of the interacting chains. This quasi-static energy-minimization method consists of iteratively adjusting the monomers coordinates by moving along the direction of the total force. Of course the energy minimization process that explores a multi-dimensional coordinate space bring the energy to the closest *local* minimum, not necessarily to the absolute energy minimum and systems can be trapped in metastable states. As a consequence, contrary to thermalized flexible polymer systems where the typical behavior at a given density does not depend on the initial state, in the case of frozen systems the conformational and mechanical properties at a given density strongly depend on the initial configuration and on the pathway used to achieve the final deformation.

As stated above, here we restrict ourself to systems of quasi-parallel fiber stacks. Aiming to understand the role of spontaneous curvature in determining the compressibility, we choose, in all the simulations reported in this chapter, to proceed by a gradual deformation of pre-aligned fibers disposed initially in their fundamental state. In practice, we build the shapes of the isolated fibers from a given mathematical function $\zeta_0(x)$ along which we place N monomers sequentially, at the equilibrium distance $l_\mathrm{b} = 0.967$ of the monomer-monomer bond interactions, setting at the same time the corresponding values of θ_0. At the end of this process, we have a fiber of N monomers in an equilibrium shape identical to the function $\zeta_0(x)$. At each step of the simulation a small affine deformation, perpendicular to the fibers principal axis, is imposed followed by an energy minimization. (See Sec. 2.1 for numerical details). The last configuration obtained at each step is used for different analysis purposes. In particular, we report in this chapter the evolution of the pressure tensor component Pyy corresponding to the axis of deformation, as a function of D - the average distance between fibers. For simplicity we drop the index yy and note P. The method used for calculating the different components of the pressure tensor is described in Sec. 2.2.

From a technical point of view, several minor modifications of our simulation tool LAMMPS were introduced in order to handle the calculation of the chains angular energy to the case of rigid fibers in 2D. These modifications, allowing to distinguish 'left handed' and 'right handed' configurations which are strictly equivalent in the three-dimensional case or for zero spontaneous curvature, are described in Appendix 6.2.

Types of spontaneous curvature disorder

We describe here three categories of typical shapes implemented by three families of functions $\zeta_0(x)$. The simulation results obtained for systems displaying these three types of disorder as well as the corresponding analytical discussions will be given in the following sections.

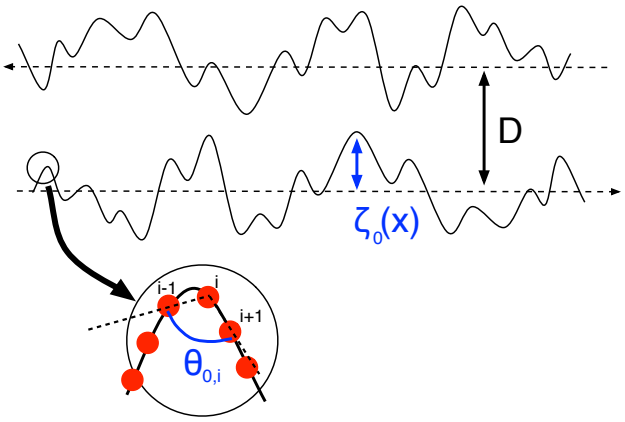

Figure 5.3: Sketch of the spontaneous shapes of two neighboring fibers. The fibers start to interact when the average distance between fibers D becomes comparable with twice the larger amplitude of the spontaneous shapes.

First, in order to calibrate our simulation method against predictions from continuous elasticity theory, we test simple systems corresponding to single fibers with sinusoidal shapes, confined between parallel walls. In practice, for consistency with the more complicated systems where periodic boundary conditions are imposed, instead of simulating single chains between walls we simulate periodic systems consisting of pairs of chains with identical sinusoidal shapes and opposite phases $\zeta_0^{(1)}(x) = D_0/2\cos(2\pi x/\lambda)$ and $\zeta_0^{(2)}(x) = D_0/2\cos(2\pi x/\lambda + \pi)$. The opposite phases coupled with chains small roughness due to the shapes of individual monomers insure that chains are not trivially sliding. In the following we will refer to this type of systems as the "single-mode fiber systems".

The second simulated system class introduces some disorder on fibers wavelengths and phases. Here we simulate a large number of parallel sinusoidal fibers $\zeta_0^{(i)}(x) = D_0/2\cos(2\pi x/\lambda_i + \psi_i)$ with identical fiber amplitudes D_0, wavelengths λ_i chosen from the Gaussian distribution for λ

$$\mathcal{P}(\lambda) = \frac{1}{\sqrt{2\pi\sigma^2}} e^{-\frac{(\lambda-\lambda_0)^2}{2\sigma^2}} \quad , \tag{5.1}$$

and a random translation phase shift ψ_i homogeneously distributed in phase space $\psi_i \in [0, 2\pi]$. We refer to this kind of disorder as systems with "wavelength disorder".

A more general system class, allowing to represent a wide range of fiber shapes is obtained by constructing $\zeta_0(x)$ as a superposition of a large number of modes, $\zeta_0(x) = \sum_i \zeta_{0,q_i}\phi_{q_i}(x)$, where the amplitudes ζ_{0,q_i} are picked from a Gaussian probability distribution :

$$\mathcal{P}(\zeta_{0,q}) = \frac{1}{\sqrt{2\pi\langle\zeta_{0,q_i}^2\rangle}} \exp\left[-\frac{\zeta_{0,q_i}^2}{2\langle\zeta_{0,q_i}^2\rangle}\right], \tag{5.2}$$

where we impose :

$$\langle\zeta_{0,q}^2\rangle = C/(kq^\alpha). \tag{5.3}$$

This class of disordered spontaneous shapes is referred to as the "q-dependent disorder case" or "smooth disorder". We note that the relation (5.3) is a generalization of the thermaly-inspired relation $\langle\zeta_{0,q}^2\rangle \propto k_B T/(kq^4)$ corresponding to the typical disorder characterizing the small fluctuations of a thermally activated semiflexible rod. Here, by playing on the value of the exponent α in (5.3), the thermal-like q-dependent disorder is generalized and we can continuously control the local waviness of the chains as illustrated in Fig. 5.4.

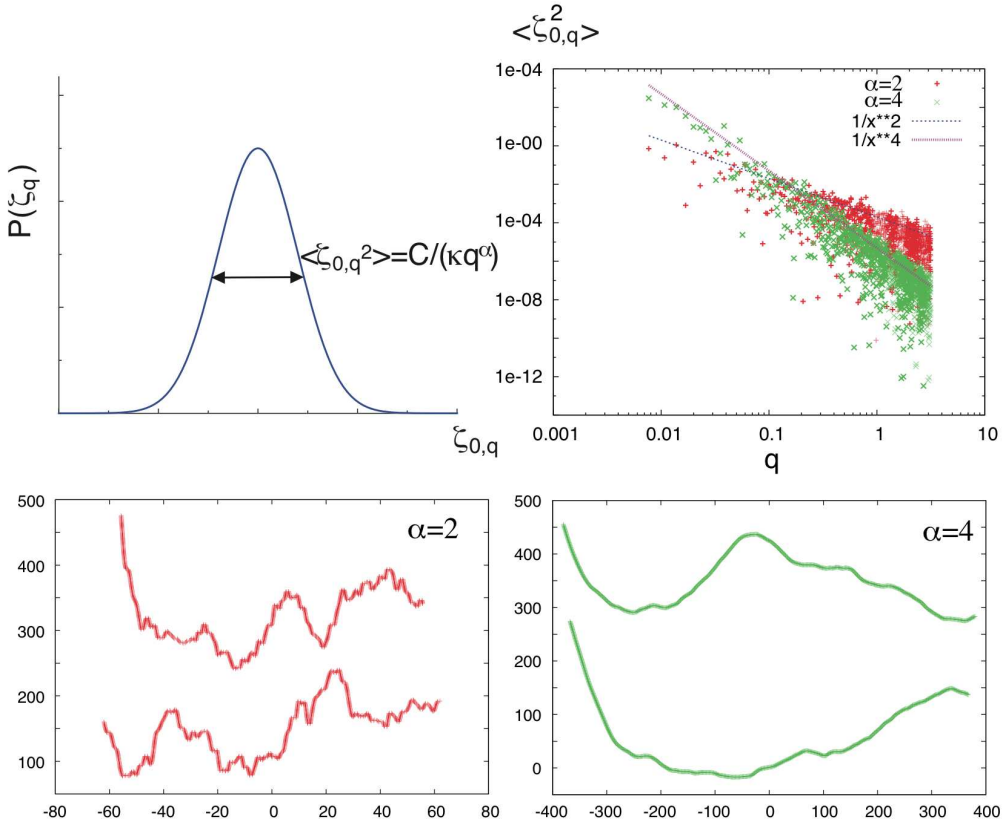

Figure 5.4: Implementation of spontaneous shapes for the third disorder class discussed in this chapter ("smooth disorder"). Top figures : the Gaussian distribution (left) determining the probability of an amplitude $\zeta_{0,q}$) for a given mode q and the amplitudes (right) extracted from this distribution as a function of q. Below, fibers shapes obtained for $\alpha = 2$ and $\alpha = 4$. In general, increasing the value of α decreases the chains roughness at small scales.

The functions used for the mode-superpositions are the eigenfunctions of the square Laplacian operator that describes curvature elasticity[116] :

$$\phi_{q_i}(x) = \frac{\cosh(\psi_i) - \cos(\psi_i)}{\sinh(\psi_i) - \sin(\psi_i)} \left[\sinh\left(\psi_i \frac{x}{Na}\right) + \sin\left(\psi_i \frac{x}{Na}\right)\right] - \left[\cosh\left(\psi_i \frac{x}{Na}\right) + \cos\left(\psi_i \frac{x}{Na}\right)\right] \ , \qquad (5.4)$$

where the numerical coefficients ψ_i are determined from the relation $\cos(\psi_i)\cosh(\psi_i) = 1$. The solutions obey approximately $\psi_i \equiv q_i Na \simeq (i + 1/2)\pi$ with $i \in \mathbb{N}$. The N wave vectors $q_i Na$ were thus picked uniformly from the set $q_i Na = (i + 1/2)\pi$, with $i = 1....N$. The shape mean square amplitude is a factor of both α and C/k with:

$$\langle \zeta_0^2 \rangle = \sum_q \langle \zeta_{0,q}^2 \rangle \propto \frac{C}{\kappa} \frac{N^{\alpha-2}}{(\alpha - 1)}. \qquad (5.5)$$

Below, we will use values of the root-mean-square amplitude ζ_0 of a fiber in the continuous distribution model as a way of monitoring the vertical average extension of the fibers. This is most conveniently obtained by measuring the gyration tensor of the fibers and by extracting its smallest eigenvalue. The values are rather well described by the analytical expression 5.5, as reported on Fig. 5.5. These values are also close to the onset of the compression curves that will be studied below, as for instance on Fig. 5.9.

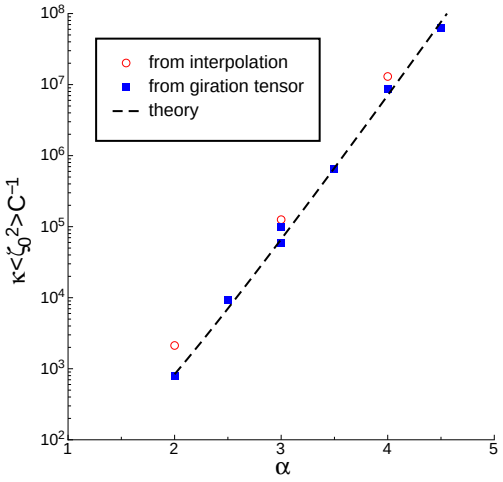

Figure 5.5: Normalized mean-square amplitudes $\kappa\langle\zeta_0^2\rangle/C$ as a function of the disorder exponent α and comparison with the analytical expression 5.5.

Relation continuous/discrete models

In the following sections we present our simulation results and compare them to analytical predictions based on continuous elasticity theory. In our analytic description chains are seen as infinitely thin continuous lines that, in analogy to the three terms in the discrete Hamiltonian used for simulations Eq. (1.1), interact via stretching, bending and excluded volume potentials. Contrary to the numerical approach that takes into account the detailed local interactions between (coarsed-grained) monomers, the analytic approach aims to capture the system's behavior using a minimal, tractable model based on several well chosen simplification assumptions.

In this sense we first assume here that the stretching term in the analytic Hamiltonian can be neglected since, in the fiber systems we treat, chains bending is much easier to achieve then chains stretching. The energy of a single chain can thus be described by the curvature Hamiltonian[116]

$$\mathcal{H}_{bending} = \frac{\kappa}{2}\int_0^L dx\,[\zeta''(x) - \zeta_0''(x)]^2\,, \tag{5.6}$$

where κ replaces the bending modulus k_θ from the simulation model and L is the chain projection on the x axis. $\zeta''(x)$ and $\zeta_0''(x)$, the second derivatives of the functions representing the chain's shapes, correspond to the chain curvature in the Monge approximation,[117] the index 0 denoting the shape or the curvature of the chain in its ground-state as discussed above.

More challenging is the choice of the analytic description for the interchain excluded volume interactions. While the simulation model directly takes into account this contribution by the local LJ potential, in order to resolve this multi-body problem analytically, in particular when chains spontaneous shape display some complex disorder, new statistical tools have to be developed.

In the two first parts of the following (single mode and single mode with wavelength disorder chains), we will assume a single chain deformation, taking into account the interaction with other chains as punctual forces. In the last part where we introduce a q-dependent disorder, we will use a self-consistent approximation in the spirit of Helfrich work on thermally activated systems.

5.2 Results

5.2.1 Single-mode

In this section we focus on the simple case of a stack of identical fibers with sinusoidal spontaneous shapes. This system will play the role of a reference system for our study. In addition, since it is possible to analytically derive the compression law of such a system,[116] it will also allow us to check the range of validity of our simulation method.

Analytical description

Introducing the spontaneous shape $\zeta_0(x) = \frac{D_0}{2}\cos\left(\frac{2\pi}{\lambda}x\right)$ in the bending Hamiltonian 5.6 leads after a simple functional minimization to the differential equation :

$$\frac{\partial^4 \zeta}{\partial x^4} = \frac{\partial^4 \zeta_0}{\partial x^4} \tag{5.7}$$

Using the boundary conditions $\zeta(0) = 0$, $\zeta(\lambda/2) = D - D_0$ and $\zeta'(0) = \zeta'(\lambda/2) = 0$ we obtain the shape of the fiber between $x \in [0, \lambda/2]$ for a compression D:

$$\zeta(x) - \zeta_0(x) = 12(D - D_0)\frac{x^2}{\lambda^2}\left(1 - \frac{4}{3}\frac{x}{\lambda}\right). \tag{5.8}$$

It is then possible to calculate the elastic energy of the fiber and the corresponding pressure :

$$E = \frac{96\kappa D_0^2}{\lambda^3}\left(\frac{D - D_0}{D_0}\right)^2 \tag{5.9}$$

$$P = \frac{1}{\lambda}\frac{\partial E}{\partial D} = \frac{192\kappa D_0}{\lambda^4}\frac{(D_0 - D)}{D_0}. \tag{5.10}$$

This is of course equivalent to the energy and the pressure of an harmonic spring with an effective spring constant :

$$\kappa_{eff} \equiv \frac{96\kappa D_0^2}{\lambda^3}. \tag{5.11}$$

Numerical results

In Fig. 5.6 we present the evolution of the pressure as function of density for different single-mode systems. We observe a very good agreement between numerical data and theory, without any fitting parameters. The small deviations from the analytical curve at low densities and for small effective bending modulus (small κ or large λ) can be explained by the limited accuracy of the Monge approximation and of the convergence of the minimization process in these regimes.

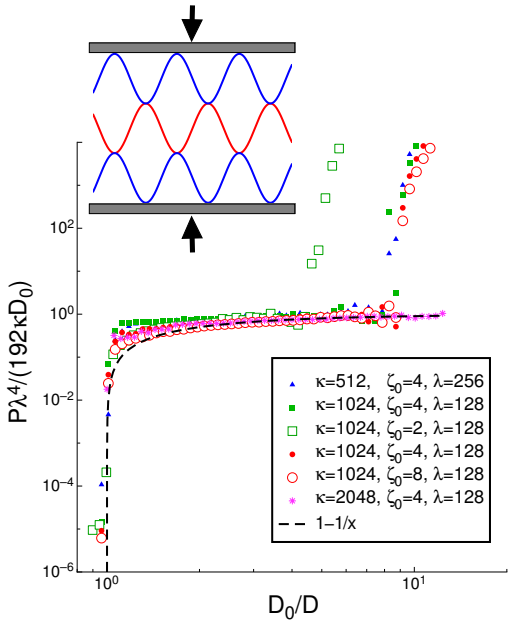

Figure 5.6: Pressure component $P \equiv Pyy$ perpendicular to the aligned fibers as a function of the typical distance D between fibers. We trace the normalized pressure $P\lambda^4/(192\kappa D_0)$ vs. reduced density D_0/D for single-mode fiber stacks for various values of amplitude ζ_0, bending modulus κ and wavelength λ. The theoretical function $1 - D/D_0$ is also plotted for comparison.

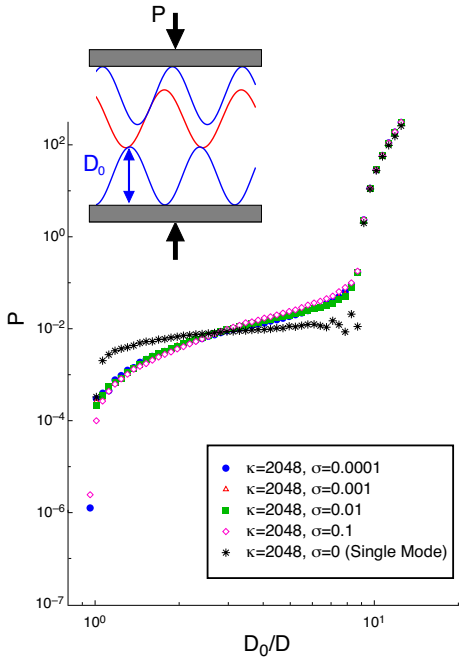

Figure 5.7: Pressure P vs. normalized density D_0/D for sinusoidal fibers of amplitude ζ_0 with wavelength λ following a Gaussian distribution of mean value λ_0 and variance σ. All the simulations presented here have the the same bending modulus $\kappa = 2048$, $\lambda_0 = 128$ and amplitude $\zeta_0 = 4$, with variance σ ranging from 0.001 to 0.1.

5.2.2 Single-mode with wavelength disorder

Having tested the validity of our simulation model on the simple single-mode systems, we now introduce disorder in the fiber stacks by taking sinusoidal spontaneous shapes with the same amplitude ζ_0 for all the fibers, but with different wavelengths λ following a Gaussian distribution of mean value λ_0 and variance σ.

Numerical results

We present on Fig. 5.7 for sinusoidal fibers of amplitude ζ_0 with wavelength λ following a Gaussian distribution of mean value λ_0 and variance σ. All the simulations presented here have the the same bending modulus $\kappa = 2048$ and amplitude $\zeta_0 = 4$, with variance σ ranging from 0.001 to 0.1. Interestingly, we observe that introducing some disorder on wave length completely modifies the compression law, even for very narrow probability distribution. Surprisingly, the compression law seems to be very weekly dependent on the distribution probability variance.

Phenomenological approach and discussion

We propose here a semi-quantitative approach to solve this problems. We consider a fiber with a sinusoidal spontaneous shape of wavelength λ and amplitude D_0. We assume that this fiber is deformed by a force $\mathbf{F}$ applied at a point M_0 and which is exerted by another fiber. This problem can be solved analytically just as in Sec. 5.2.1. To obtain the deformed shape of the fiber we have to solve the differential equation :

$$\frac{\partial^4 \zeta}{\partial x^4} = \frac{\partial^4 \zeta_0}{\partial x^4} \tag{5.12}$$

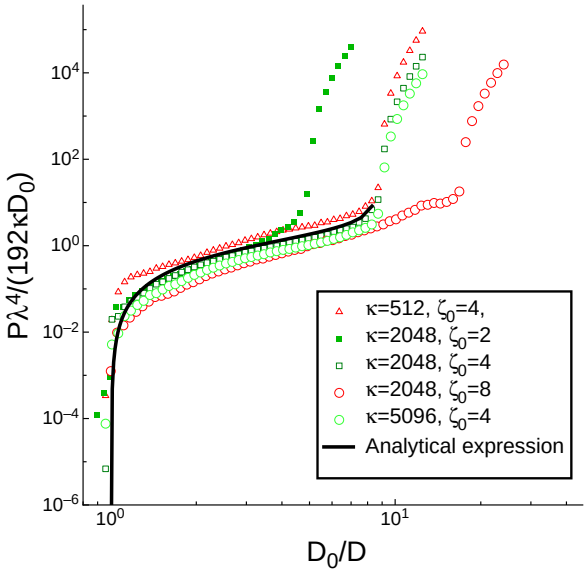

Figure 5.8: Normalized pressure $P\lambda^4/(192\kappa D_0)$ vs. normalized density D_0/D for sinusoidal fibers of amplitude ζ_0 with wavelength λ following a Gaussian distribution of mean value λ_0 and variance σ. All the simulations presented here have the the same bending modulus $\kappa = 2048$ and amplitude $\zeta_0 = 4$, with variance σ ranging from 0.001 to 0.1. Solid line corresponds to the analytical expression of Eq. (5.15).

with the appropriate boundary conditions. We obtain the shape of the fiber for a compression D and we can calculate the elastic energy of the fiber and the corresponding the pressure :

$$E(x_0) = \frac{96\kappa\lambda^3\left(D_0\left(1+\cos\left(\frac{2\pi x_0}{\lambda}\right)\right)-D\right)^2}{(\lambda-2x_0)^4(\lambda+4x_0)^2} \tag{5.13}$$

$$P(x_0) = \frac{192\kappa\left(D_0\left(1+\cos\left(\frac{2\pi x_0}{\lambda}\right)\right)-D\right)}{\lambda^4(1-2x_0/\lambda)^4(1+4x_0/\lambda)^2}. \tag{5.14}$$

We define now the dimensionless variable $u = x_0/\lambda$. Integrating the pressure over all the accessible position for x_0 we obtain the total pressure P as :

$$\frac{P\lambda^4}{192\kappa D_0} = 2\int_0^{u_{max}} \frac{(1+\cos(2\pi u)-D/D_0)}{(1-2u)^4(1+4u)^2}du. \tag{5.15}$$

with $2\pi u_{max} = \arccos(D/D_0 - 1)$. We report simulation data for various parameters (κ, λ and ζ_0) on Fig. 5.8 where we normalize the pressure by $P\lambda^4/(192\kappa D_0)$. Except for small bending modulus ($\kappa < 128$) and large amplitudes ($\zeta_0 > 8$) - limits already discussed in the previous section - all the data seem to be very well described by the expression 5.15.

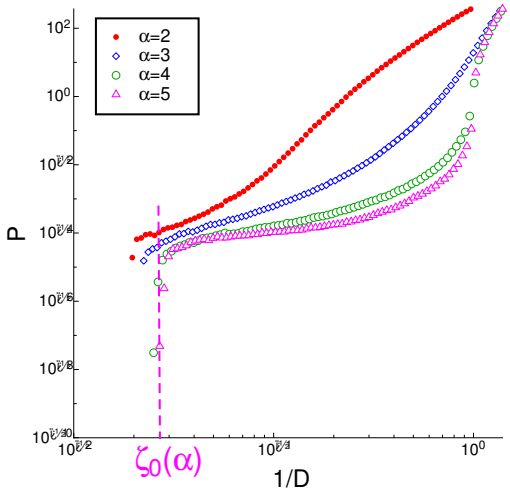

Figure 5.9: Influence of the shape disorder on the normal pressure of the fiber bundles. The mean amplitudes of the Fourier modes of the fibers' ground state are imposed by increasing the value of α. We use this results to determine the value $\zeta_0(\alpha)$ where the pressure begin to increase.

5.2.3 Smooth distribution

In the previous paragraphs we validated our model and determined a relevant range of parameters, clearly showing also the influence of wavelength disorder on the compression laws of fiber stacks. We will now deal with systems with a more complex spontaneous shape. We choose to focus on systems with almost continuous distributions of wavelengths where the mean square amplitude of each mode depends on the wavenumber as a power law:

$$\langle \zeta_{0,q}^2 \rangle = \frac{C}{N\kappa q^\alpha}. \tag{5.16}$$

This kind of amplitude distribution covers a large spectrum of fibers forms as illustrated in Fig. 5.4. By choosing a small value of α we obtain very rough fibers, while increasing the value of α yields progressively smoother fibers. It is also an interesting system for a direct comparison with thermally activated systems. The compression behavior of this class of systems, plotted in Fig. 5.9, shows a strong dependence on the value of the exponent α i.e. on the relative weight of the different modes in the shape of the individual fibers. In the following we will try to explain this results analytically.

Mean-Field Calculation

If one assumes that different fibers interact through a two body potential V, then the total interaction energy E_{int} can be written as:

$$E_{\text{int}} = \sum_{n,m=1}^{\mathcal{N}} \int_0^L dx \int_0^L dx' \; V\left[\zeta_m(x) + mD - (\zeta_n(x') + nD)\right]. \tag{5.17}$$

In the spirit of Helfrich treatment of thermally activated fluid membranes and fibers,[118–120] we follow a simple mean-field approximation. We assume that forces between first-neighbors dominate the interaction energy, an exact assumption for excluded volume potentials and a good approximation for other short range forces such as those given by screened electrostatic potentials. Then the sum of the bending (5.6) and

interaction (5.17) terms can be written as the effective energy :

$$E_{\text{eff}} = \frac{\kappa}{2}\sum_{n=1}^{\mathcal{N}}\int_0^L dx\left[\zeta_n''(x)-\zeta_{0,n}''(x)\right]^2 + \frac{B}{2}\sum_{n=1}^{\mathcal{N}}\int_0^L dx\left[\zeta_{n+1}(x)-\zeta_n(x)\right]^2 \ . \tag{5.18}$$

By functional minimization, we can deduce fiber's shape in reciprocal space as:

$$\zeta_{qQ} = \frac{\kappa q^4}{\kappa q^4 + B(Q)}\zeta_{0,qQ} \tag{5.19}$$

By introducing this relation in the energy density obtained by the *Helfrich inspired* model:

$$e = \frac{1}{2(2\pi)^3}\int d\vec{q}dQ\left[\kappa q^4(\zeta_{qQ}-\zeta_{0,qQ})^2 + B(Q)\zeta_{qQ}^2\right] \ . \tag{5.20}$$

and integrating over Q, we obtain a general, *quenched disorder dependent*, expression for the mean energy density:

$$\langle e\rangle = \frac{C}{N\pi\kappa}\frac{B}{D}\int_{\frac{\pi}{2L}\sim 0}^{+\infty} dq\left\langle {\zeta_{0,q}}^2\right\rangle\left(\frac{\kappa q^4}{4B+\kappa q^4}\right)^{\frac{3}{2}} \ . \tag{5.21}$$

Supposing now a quenched disorder of the form $\left\langle {\zeta_{0,q}}^2\right\rangle = \frac{C}{N\kappa q^\alpha}$ and using $q_1 \equiv (\frac{\kappa}{4B})^{1/4}q$ we get:

$$\begin{aligned}\langle e\rangle &= \frac{C}{N\pi\kappa}\frac{B}{D}\left(\frac{4B}{\kappa}\right)^{\frac{1}{4}}\left(\frac{4B}{\kappa}\right)^{\frac{-\alpha}{4}}\int_0^{+\infty} dq_1 q_1^{-\alpha}\left(\frac{q_1^4}{1+q_1^4}\right)^{\frac{3}{2}} \\ \langle e\rangle &\propto \frac{C}{D}B^{\frac{5-\alpha}{4}}\kappa^{\frac{\alpha-5}{4}}\end{aligned} \tag{5.22}$$

An auto-coherent calculation allows to extract the compression modulus:

$$B = d\frac{\partial^2\langle e\rangle}{\partial D^2} \propto \frac{C}{D^2}B^{\frac{5-\alpha}{4}}\kappa^{\frac{\alpha-5}{4}} \tag{5.23}$$

$$B = \left(\frac{C}{D^2}\kappa^{\frac{\alpha-5}{4}}\right)^{\frac{4}{\alpha-1}} \tag{5.24}$$

and calculate the pressure:

$$P \propto BD \propto (C)^{\frac{4}{\alpha-1}}\kappa^{\frac{\alpha-5}{\alpha-1}}D^{\frac{\alpha-9}{\alpha-1}} \tag{5.25}$$

This results suggests that it is possible to tune the elastic response of a fiber bundle by playing on the relative weight of the different modes in the shape of the individual fibers. It is possible to generalize this mean field calculation to d-dimensional systems (with athermal membranes of dimension $d-1$). We obtain for the pressure:

$$P \propto (C)^{\frac{4}{\alpha+1-d}}\kappa^{\frac{\alpha-3-d}{\alpha+1-d}}D^{\frac{\alpha-7-d}{\alpha+1-d}}. \tag{5.26}$$

For *thermal-like* quenched disorder ($\alpha = 4$) we have $P \propto C^{4/3}\kappa^{-1/3}D^{-5/3}$ in the two-dimensional case (fibers) and $P \propto C^2\kappa^{-1}D^{-3}$ in the three dimensional case (membranes), just as for real thermalized systems.

Scaling Arguments

Interestingly, these compression-law predictions can also be derived by *thermally-inspired* scaling arguments: Helfrich pressure for fluctuating rods can be obtained by supposing that the fluctuating rods confined to a distance D can be seen as a sequence of 'blobs' of size $\lambda * D$ with typical energy of k_BT. The relation between λ and D can be calculated by:

$$\kappa q^4 D^2\lambda = k_BT \Rightarrow D^2 = \frac{k_BT}{\kappa q^3} \Rightarrow \lambda = \left(\frac{\kappa D^2}{k_BT}\right)^{\frac{1}{3}}. \tag{5.27}$$

α	β
2	7
3	3
4	5/3
5	1
6	3/5

Figure 5.10: Predicted exponents β for pressure-density power laws $D^{-\beta}$ calculated theoretically for different values of α in 2D.

As consequence, the pressure scales as:

$$P \propto \frac{E}{\lambda D} = \frac{\kappa q^4 D^2 \lambda}{\lambda D} = \frac{C^{\frac{4}{3}}}{\kappa^{\frac{1}{3}} D^{\frac{5}{3}}} \tag{5.28}$$

In analogy, in the athermal case, if we impose the relation $\left\langle {\zeta_{0,q}}^2 \right\rangle = \frac{k_B T}{\kappa q^\alpha}$, we get:

$$\kappa q^\alpha D^2 \lambda = k_B T \Rightarrow D^2 = \frac{k_B T}{\kappa q^{\alpha-1}} \Rightarrow \lambda = (\frac{\kappa D^2}{k_B T})^{\frac{1}{\alpha-1}}, \tag{5.29}$$

and we expect for the pressure:

$$P \propto \frac{E}{\lambda D} = \frac{\kappa q^4 D^2 \lambda}{\lambda D} = \frac{\kappa D}{\lambda^4} = \frac{\kappa D}{(\frac{\kappa \zeta_q^2}{k_B T})^{\frac{4}{\alpha-1}}} = (k_B T)^{\frac{4}{\alpha-1}} \kappa^{\frac{\alpha-5}{\alpha-1}} D^{\frac{\alpha-9}{\alpha-1}}. \tag{5.30}$$

which is exactly the same as Eq.(5.25) using $k_B T = C$.

Discussion

We plot on Fig. 5.11 the normalized pressure following theoretical expression Eq. (5.25) as a function of density. For the values of $\alpha > 2$, we clearly observe 3 different regimes on the compression curves.

For the large density limit, where fibers are in close contact, we observe that the data collapses well on the same master curve, similarly to those of a single mode fiber. In that limit of compact fibers, spontaneous shape disorder is irrelevant.

For an intermediate density, the compression law seems to be well described by the self-consistent equation (5.26), as shown on Fig. 5.11 where lines corresponds to the best fitting by A/D^β with only A as fitting parameter. Such an agreement is quite remarkable. It clearly appears that the validity range of these power law increases with increasing α. We should stress the low validity range of the predicted pressure power law for the case of $\alpha = 2$. It will be interesting to extend our simulation effort for this case of stronger disorder for larger fiber sizes.

Finally, for the low density limit, where distance between fibers is of the order of the fibers mean-square amplitude, we observe a deviation of the simulation data to the power law behavior. Obviously, mean-field theory is not effective in this limit, because the number of fibers of mean amplitude larger than ζ_0^2 vanishes, contrary to the thermal case. We can qualitatively understand this regime. The force rises sharply from zero as the fiber-fiber contacts progressively build up, with essentially single-mode compression behavior. This is shown by Fig. 5.11 where dotted lines correspond to the single mode expression 5.10 with an effective wavelength λ_{eff}. Values of λ_{eff} are reported on Fig. 5.11. They are all of the same order of magnitude, smaller than the maximum value of λ ($\lambda_{max} = 820$) but closer to the second mode wavelength ($\lambda = 585$).

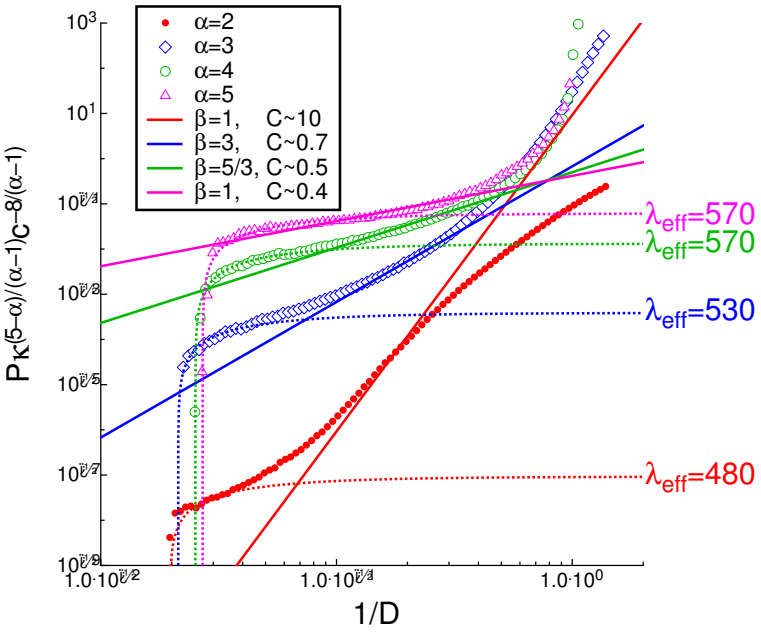

Figure 5.11: Normalized pressure following expression Eq.(5.25) as a function of $1/D$. The solid lines represent the power law predicted by the theory without any fitting (only the constant values). The dotted lines correspond to the single mode expression 5.10 with an effective wavelength λ_{eff}.

5.3 Conclusions

In this chapter we studied the mechanical behavior of corrugated fiber stacks. Contrary to compact straight fiber arrangements, that exhibit a high compression modulus, the shape waviness imprinted on the fibers brings to the stack compression behavior a fluffiness that is also controlled by the chains bending modes, in a manner reminiscent of many fibrous three dimensional materials.

After having shown that our simulation tool reproduces well fiber mechanical behavior expected from continuous elasticity theory, and that simple disorder such as phase and wavelength disorder at fixed amplitude is enough to induce a non-trivial compression behavior of the stack, we have studied more realistic distributions for fiber disorder, with fiber spontaneous shapes reconstituted from a superimposition of modes with q-dependent amplitudes. The results show that the compression law for fiber stacks displays three typical regions. At inter-fiber distances comparable to the monomer size, the fibers are all well aligned in a compact manner, and the compression forces are very high. At very large distances, of the order of the fibers mean-square amplitude, the force rises sharply from zero as the fiber-fiber contacts progressively build up, with essentially single-mode compression behavior. In between these two limits, the stack displays a fluffy compression behavior, with deformation forces controlled by the fiber bending energy. For fibers of moderate corrugation the compression forces compare favorably with a mean-field theory based on an analogy with thermalized polymers and membranes.

Chapter 6

Conclusions

6.1 Summary

In this PhD manuscript we have presented our results on polymer and fiber chains in strictly two-dimensions.

The motivation for this work was discussed in Chapter 1. There, we argued that present trends in nanosciences require a better understanding of polymers confined in very thins layers, where often chains do not self-intersect. We have pointed also to the interesting role that rigidity plays in dense two-dimensional polymers, both in thermal macromolecular materials and in macroscopic disordered fiber systems.

In Chapter 2, we reviewed our methods for numerical simulation and data analysis. A detailed description of our coarse-grained bead-spring model as well as the methods used for conformation sampling was made. Strategies for extracting the relevant physical quantities from the simulation data were also summarized.

In Chapter 3 we have investigated the density crossover scaling of various thermodynamic and conformational properties of thermalized and flexible polymer chains. We have focused on properties related to the θ_2 contact exponent.[65] It has been shown that the latter exponent not only characterizes (by definition) the intrachain subchain size distribution $G_e(r,s)$ for arc-lengths s with $1 \ll s \ll N$, but also the interchain pair distribution function $g_{\rm int}(r) \sim r^{\theta_2}$, as shown in Fig. 3.12, and the monomer contact number $n_{\rm int} \sim e_{\rm int} \sim 1/N^{\nu\theta_2}$ (Figs. 3.3 and 3.13). The scaling with chain length N established for dense melts[45,46,66] is found to remain valid for all densities if the data is renormalized in terms of chains of blobs of $g \sim 1/\rho^2$ monomers.[48] The corresponding semidilute crossover scaling with respect to density ρ has been confirmed to be consistent with our data over about one order of magnitude, e.g. the pressure is found to scale as $P \sim \rho^3$ (Fig. 3.4) as expected.[59]Obviously, for large densities where g becomes too small, deviations from the predicted ρ-scaling show up for various properties due the additional non-universal monomer physics. This additional monomer physics at high densities has been seen to be particulary marked for the various thermodynamic properties discussed (Figs. 3.4, 3.5 and 3.15). As expected from the generalized Porod scattering of compact objects of fractal perimeter dimension d_p summarized in Sec. 2.3.2, the intramolecular form factor $F(q)$ measuring the composition fluctuations at the fractal perimeters of the compact blob chains approaches with increasing density and chain length a power-law asymptote.

Much more briefly, we have investigated in Chapter 4 the influence of a finite bending rigidity. The key point we made is simply that persistence lengths effects do not change the general scaling in terms of compact chains of blobs of fractal contour as long as the persistence length remains *smaller* than the semidilute blob size ($s_p \ll g \ll N$), i.e. our theoretical and computational results made in Chapter 3 are robust especially for the experimentally more relevant low volume fractions. With increasing rigidity the chains are seen to align locally (Fig. 4.1). These bundles of chains remain compact on large scales, however, at least if the bending rigidity is introduced starting with compact configurations of flexible chains. The characterization of the transition between the isotropic phase of compact and segregated chains at low densities and bending rigidities to the ordered nematic phase in the opposite limit is the topic of a still on-going theoretical and numerical investigation beyond the scope of my PhD thesis.

Chapter 5 was devoted to the study of macroscopic fiber stacks where, contrary to the polymer materials discussed in Chapter 3 and 4, temperature does not play any role. In these systems, where disorder is introduced by the non-straight shapes of the individual fibers, new methods are required to compute chain equilibrium conformation and stack mechanical properties. Using the athermal limit of our bead-spring model, and adapting the computational tools for athermal energy minimization, we have explored the effect of different classes of spontaneous curvature distributions on the system properties. After having validated in Sec. 5.1 our tools against standard continuous mechanical theories for sinusoidal fibers, for which explicit predictions can be made, we have shown in Sec. 5.2 that the compression behavior of phase disordered fibers with even a narrow distribution of wavelength values is drastically different from single fiber compression. More realistic distributions for fiber disorder were studied in Sec. 5.3, with fiber spontaneous shapes reconstituted from a superimposition of modes with q-dependent amplitudes. The results compare favorably with a mean-field theory based on an analogy with thermalized polymers and membranes.

6.2 Perspectives

Critical temperature of demixing of polymer blends

Interestingly, the scaling of the intermolecular contact probability $n_{\rm int}$ tested numerically in Sec. 3.3.6 is consistent with recent Monte Carlo simulations of symmetrical polymer mixtures using a version of the bond-fluctuation model in strictly two dimensions.[73,74] These simulations show that the compatibility of the chains is strongly *enhanced* compared to 3D blends. We remind that for the latter systems the scaling of the critical temperature of unmixing $T_{\rm c}$ is well described by the Flory-Huggins mean-field prediction,[59] i.e.

$$k_{\rm B}T_{\rm c} \sim 1/\chi_{\rm c} \sim N \tag{6.1}$$

where $\chi_{\rm c}$ stands for the critical Flory demixing parameter. The compatibility of the blend decreases thus very strongly with chain length.[87,121] More generally, $k_{\rm B}T_{\rm c}$ should be set by the typical interaction energy $Ne_{\rm int}$ between different chains. As we have shown in Sec. 3.2.1 for homopolymer solutions $Ne_{\rm int} \sim Nn_{\rm int} \sim \rho^{21/8}N^{5/8}$ holds over several orders of magnitude in density and chain length. The same scaling is expected to hold close to the critical point of a polymer mixture. According to Eq. (3.27) and using Eq. (3.6) it follows thus that

$$k_{\rm B}T_{\rm c} \approx Nn_{\rm int} \approx g^{2-\nu_0\theta_{2,0}-\nu_0 d} \times (N/g)^{1-\nu\theta_2} \tag{6.2}$$

$$\sim \rho^{21/8}N^{5/8} \tag{6.3}$$

in the compact chain limit. The power-law exponent $5/8 = 0.625$ predicted in Eq. (6.3) for the N-dependence of strictly 2D self-avoiding walks agrees well with the value 0.65 obtained by fitting $T_{\rm c}$ for all computed chain lengths.[73] (For the three longest chains computed a somewhat lower value 0.5 ± 0.1 has been reported.) The corresponding strong power-law increase $T_{\rm c} \sim \rho^{21/8}$ with density has to our knowledge not been probed yet. As predicted theoretically in Ref.[66] and as checked numerically in Ref. [74], it is crucial here that the chains of the blend do not overlap or intersect as it may occur in thin films of finite width where the number of monomers of a chain in contact with monomers from other chains becomes proportional to N apart from the logarithmic corrections implied by Eq. (3.4). Interestingly, for 3D good solvent polymer solutions it follows from Eq. (6.2) that

$$k_{\rm B}T_{\rm c} \approx g^{-0.243} \times (N/g) \sim \rho^{1.626}N \tag{6.4}$$

where we have used that $\nu_0 \approx 0.588$ and $\theta_{2,0} \approx 0.815$ in the dilute limit[122] and $\nu = 1/2$ and $\theta_2 = 0$ for large densities ($N \gg g$). The increase of $T_{\rm c}$ with density is thus predicted to be much weaker in 3D compared to strictly 2D layers. Since the predicted density dependence for semidilute good solvent solutions, eqs. (6.3,6.4), deviates strongly from the standard mean-field prediction ($T_{\rm c} \sim \rho^2$),[1,59] this suggests urgently a verification by computer simulation and real experiments.

Spontaneous shape effects in experimentally-inspired systems

The last decade has seen an important effort to understand granular media, its static and dynamic properties being determined by how disorder in grain shape and packing couples to the organization of the chains of force in the granular beds. Studies in fiber systems are much more scarce, and our attempt is one of the first to carry out a parallel effort to understand packings of non-straight macroscopic fibers. Other groups have recently presented new experimental data on fiber bundles organized as ponytails, and a recent session was devoted to this field at the APS 2012 March meeting. The challenges posed by these experimental systems require further theoretical and numerical efforts. We have mainly focused on two-dimensional well aligned systems undergoing uniaxial compression. In two dimensions, other limits remain still to be explored, as for instance that of shorter isotropically distributed wavy fibers. In this limit we foresee a key role of strong bending deformations, and a limited influence of shape disorder of the individual chains. In three dimensions, torsion will also play a role for fibers, and the confinement by near neighbors will be less pronounced, as discovered by Beckrich *et al.*[31] An interesting extension of our work in three dimensions would consist of treating organized piles of corrugated sheets, a type of organization found in many natural and synthetic materials such as plants,tissue piles, cardboard stacks and many more. For all these systems, one might also consider, in both two and three dimensions, the role of external forces such has gravity, that can be easily accounted for by our simulation methods. We believe that we have set the foundations for further precise comparison between simulations and experiments. In particular, a great value would certainly be found in carrying out numerical simulations on systems representing types of disorder actually determined from experimental systems, in order to test the predictive power of the simulations against say, the actual mechanical properties measured in experiments.

Bibliography

[1] M. Rubinstein and R.H. Colby. *Polymer Physics*. Oxford University Press, Oxford, 2003.

[2] A. Silberberg. The adsorption of flexible macromolecules. *The Journal of Physical Chemistry*, 66(10):1872–1883, 1962.

[3] Masatami Takeda and Ryuichi Endo. Viscosity of dilute polyvinyl chloride solution. *The Journal of Physical Chemistry*, 60(9):1202–1204, 1956.

[4] S. Wu. *Polymer Interfaces and Adhesion*. Marcel Dekker: New York, 1982.

[5] I.C. Sanchez. *Physics of Polymer Surfaces and Interfaces*. Butterworth-Heinemann: Boston, 1992.

[6] A. Karim and S.K. Kumar. *Polymer Surfaces, Interfaces, and Thin Films*. World Scientific: Singapore, 2000.

[7] F. Garbassi, M. Morra, and E. Ochiello. *From Physics to Technology*. Wiley: Chichester, U.K., 2000.

[8] D. D. Lasic and F. J. Martin. *Stealth Liposomes*. CRC Press, 1995.

[9] *Molecular Biology of the Cell*. American Society for Cell Biology, 2012.

[10] E. Meyer, R.M Overney, K. Dransfeld, and T. Gyalog. *Nanoscience: Friction and Rheology on the Nanometer Scale*. World Scientific, Singapore, 1998.

[11] A.N. Semenov and A. Johner. Theoretical notes on dense polymers in two dimensions. *The European Physical Journal E: Soft Matter and Biological Physics*, 12:469–480, 2003. 10.1140/epje/e2004-00019-2.

[12] B. Maier and J. O. Rädler. *Phys. Rev. Lett.*, 82:1911, 1999.

[13] X. Wang and V. J. Foltz. *J. Chem. Phys.*, 121:8158–8162, 2004.

[14] B. Frank, A.P. Gast, T.P. Russel, H.R. Brown, and C.J. Hawker. Polymer mobility in thin films. *Macromolecules*, 29:6531–6534, 1996.

[15] R.L. Jones, S.K. Kumar, D.L. Ho, R.M. Briber, and T.P. Russel. Chain conformation in ultrathin polymer films. *Nature*, 400:146–149, 1999.

[16] B. Maier and J. O. Rädler. *Phys. Rev. Lett.*, 82:1911, 1999.

[17] B. Maier and J. O. Rädler. *Macromolecules*, 33:7185, 2000.

[18] S. Granick, S.K. Kumar, E.J. Amis, and *et al.* Macromolecules at surfaces: Research challenges and opportunities from tribology to biology. *J. Polym. Sci. B*, 41:2755–2793, 2003.

[19] K. Shin, H. Xiang, S.I. Moon, T. Kim, T.J. MacCarthy, and T.P Russel. Curving and frustrating flatland. *Science*, 306:76, 2004.

[20] P.A. O'Connell and G.B. McKenna. Rheological measurements of the thermoviscoelastic response of ultrathin polymer films. *Science*, 307:1760–1763, 2005.

[21] G. T. Gavranovic, J. M. Deutsch, and G. G. Fuller. Two-dimensional melts: Polymer chains at the air-water interface. *Macromolecules*, 38:6672–6678, 2005.

[22] F.C. Sun, A.V. Dobrynin, D.S. Shirvanyants, H.J. Lee, K. Matyjaszewski, G.J. Rubinstein, M. Rubinstein, and S.S. Sheiko. *Phys. Rev. Lett.*, 99:137801, 2007.

[23] K. Shin, S. Obukhov, J.-T. Chen, J. Huh, Y. Hwang, S. Mok, P. Dobriyal, P. Thiyagarjan, and T.P. Russell. Enhanced mobility of confined polymers. *Nature Materials*, 6:961, 2007.

[24] Kenshiro Shuto, Yushi Oishi, Tisato Kajiyama, and Charles C. Han. Aggregation structure of two-dimensional ultrathin polystyrene film prepared by the water casting method. *Macromolecules*, 26(24):6589–6594, 1993.

[25] Kenshiro Shuto, Yushi Oishi, Tisato Kajiyama, and Charles C. Han. Preparation of 2-dimensional ultra thin polystyrene film by water casting method. *Polymer Journal*, 25(3):291–300, 1993.

[26] Marjolein Dijkstra and Daan Frenkel. Simulation study of a two-dimensional system of semiflexible polymers. *Phys. Rev. E*, 50:349–357, Jul 1994.

[27] P. Philipse. The random contact equation and its implications for (colloidal) rods in packings, suspensions, and anisotropic powders. *Langmuir*, 12:1127–1133, 1996.

[28] Jennifer Galanis, Daniel Harries, Dan L Sackett, Wolfgang Losert, and Ralph Nossal. Spontaneous patterning of confined granular rods. *Physical Review Letters*, 96(2):4, 2006.

[29] A first conference on this topic has been held at the 2012 APS March meeting. Session H52: Extreme Mechanics - Rods.

[30] Raymond E. Goldstein, Patrick B. Warren, and Robin C. Ball. Shape of a ponytail and the statistical physics of hair fiber bundles. *Phys. Rev. Lett.*, 108:078101, Feb 2012.

[31] P. Beckrich, G. Weick, C.M. Marques, and T. Charitat. Compression modulus of macroscopic fiber bundles. *Europhysics Letters*, 64:647–653, 2003.

[32] P. M. Chaikin and T. C. Lubensky. *Principles of condensed matter physics*. Cambridge University Press, 1995.

[33] J.P. Wittmer, A. Cavallo, H. Xu, J. Zabel, P. Polińska, N. Schulmann, H. Meyer, J. Farago, A. Johner, S.P. Obukhov, and J. Baschnagel. Scale-free static and dynamical correlations in melts of monodisperse and flory distributed homopolymers: A review of recent bond-fluctuation model studies. *J. Stat. Phys.*, 145:1017–1126, 2011.

[34] P. J. Flory. The configuration of real polymer chains. *J. Chem. Phys.*, 17:303, 1949.

[35] P.G. de Gennes. *Scaling Concepts in Polymer Physics*. Cornell University Press, Ithaca,NY, 1979.

[36] B. Duplantier. Exact contact critical exponents of a self-avoiding polymer chain in two dimensions. *Phys. Rev. B*, 35:5290–5293, 1987.

[37] Bertrand Duplantier. Two-dimensional polymers and conformal invariance. *Physica A: Statistical and Theoretical Physics*, 163(1):158 – 182, 1990.

[38] D. W. Schaefer, J. F. Joanny, and P. Pincus. Dynamics of semiflexible polymers in solution. *Macromolecules*, 13(5):1280–1289, 1980.

[39] H.-P. Hsu, W. Paul, and K. Binder. Breakdown of the Kratky-Porod wormlike chain model for semiflexible polymers in two dimensions. *EPL*, 95:68004, 2011.

[40] P. J. Flory. Statistical thermodynamics of semi-flexible chain molecules. *Proceedings of the Royal Society of London. Series A. Mathematical and Physical Sciences*, 234(1196):60–73, 1956.

[41] J.L. Jacobsen and J. Kondev. Continuous melting of compact polymers. *Phys. Rev. Lett.*, 92:210601, 2004.

[42] J.L. Jacobsen and J. Kondev. Conformal field theory of the flory model of polymer melting. *Phys. Rev. E*, 69:066108, 2004.

[43] M.P. Allen and D.J. Tildesley. *Computer Simulation of Liquids*. Oxford University Press, Oxford, 1994.

[44] D. Frenkel and B. Smit. *Understanding Molecular Simulation – From Algorithms to Applications*. Academic Press: San Diego, 2002.

[45] H. Meyer, T. Kreer, M. Aichele, A. Cavallo, A. Johner, J. Baschnagel, and J. P. Wittmer. Perimeter length and form factor in two-dimensional polymer melts. *Phys. Rev. E*, 79:050802(R), 2009.

[46] H. Meyer, J. P. Wittmer, T. Kreer, A. Johner, and J. Baschnagel. Static properties of polymer melts in two dimensions. *J. Chem. Phys.*, 132:184904, 2010.

[47] H. Meyer, N. Schulmann, J. E. Zabel, and J. P. Wittmer. The structure factor of dense two-dimensional polymer solutions. *Comp. Phys. Comm.*, 182:1949, 2011.

[48] N. Schulmann, H. Meyer, J. P. Wittmer, A. Johner, and J. Baschnagel. Interchain monomer contact probability in two-dimensional polymer solutions. *Macromolecules*, 45:1646, 2012.

[49] J. P. Wittmer, H. Meyer, A. Johner, T. Kreer, and J. Baschnagel. Algebraic displacement correlation in two-dimensional polymer melts. *Phys. Rev. Lett.*, 105:037802, 2010.

[50] A. Baumgärtner. *Polymer*, 23:334, 1982.

[51] I. Carmesin and K. Kremer. *J. Phys. France*, 51:915, 1990.

[52] B. Ostrovsky, M.A. Smith, and Y. Bar-Yam. Simulations of polymer interpenetration in 2d melts. *Int. J. Modern Physics C*, 8:931–939, 1997.

[53] A. Yethiraj. Computer simulation study of two-dimensional polymer solutions. *Macromolecules*, 36:5854, 2003.

[54] H. Meyer, J.P. Wittmer, N. Schulmann, T. Kreer, A. Johner, and J. Baschnagel. Static properties of two-dimensional polymer solutions: Density crossover scaling. *J. Chem. Phys.*, 2010. in preparation.

[55] A. Cavallo, M. Müller, J. P. Wittmer, A. Johner, and K. Binder. Single chain structure in thin polymer films: corrections to Flory's and Silberberg's hypotheses. *J. Phys.: Condens. Matter*, 17:S1697–S1709, 2005.

[56] A. Baumgärtner and D. Yoon. *J. Chem. Phys.*, 79:521, 1983.

[57] Andrzej Kolinski, Jeffrey Skolnick, and Robert Yaris. Monte Carlo study of local orientational order in a semiflexible polymer melt model. *Macromolecules*, 19(10):2550–2560, 1986.

[58] A. L. Rodriguez, H. P. Wittmann, and K. Binder. Orientational ordering in two-dimensional polymer solutions: Monte Carlo simulations of a bond-fluctuation model. *Macromolecules*, 23(19):4327–4335, 1990.

[59] P. G. de Gennes. *Scaling Concepts in Polymer Physics*. Cornell University Press, Ithaca, New York, 1979.

[60] G. S. Grest and K. Kremer. *Phys. Rev. A*, 33:3628, 1986.

[61] K. Kremer and G.S. Grest. *J. Chem. Phys.*, 92:5057–5086, 1990.

[62] M.P. Allen and D.J. Tildesley. *Computer Simulation of Liquids*. Oxford Science Publication, 1987.

[63] Magnus R. Hestenes and Eduard Stiefel. Methods of Conjugate Gradients for Solving Linear Systems. *Journal of Research of the National Bureau of Standards*, 49(6):409–436, December 1952.

[64] Andrzej Kolinski, Jeffrey Skolnick, and Robert Yaris. Order-disorder transitions in tetrahedral lattice polymer systems. *Macromolecules*, 19(10):2560–2567, 1986.

[65] B. Duplantier. Statistical mechanics of polymer networks of any topology. *J. Stat. Phys.*, 54:581, 1989.

[66] A. N. Semenov and A. Johner. Theoretical notes on dense polymers in two dimensions. *Eur. Phys. J. E*, 12:469, 2003.

[67] S. J. Plimpton. Fast parallel algorithms for short-range molecular dynamics. *J. Comp. Phys.*, 117:1–19, 1995.

[68] D. P. Landau and K. Binder. *A Guide to Monte Carlo Simulations in Statistical Physics*. Cambridge University Press, Cambridge, 2000.

[69] P. H. Nelson, T. A. Hatton, and G.C. Rutledge. General reptation and scaling of 2d athermal polymers on close-packed lattices. *J. Chem. Phys.*, 107:1269, 1997.

[70] P. Polanowski and T. Pakula. Studies of polymer conformation and dynamics in two dimensions using simulations based on the dynamic lattice liquid (dll) model. *J. Chem. Phys.*, 117:4022–4029, 2002.

[71] N. K. Balabaev, A. A. Darinskii, I. M. Neelov, N. V. Lukasheva, and I. Emri. Molecular dynamics simulation of a two-dimensional polymer melt. *Polymer Science Series A*, 44:781–790, 2002.

[72] A. Yethiraj. Computer simulation study of two-dimensional polymer solutions. *Macromolecules*, 36:5854, 2003.

[73] A. Cavallo, M. Müller, and K. Binder. Anomalous scaling of the critical temperature of unmixing with chain length for two-dimensional polymer blends. *Europhys. Lett.*, 61:214–220, 2003.

[74] A. Cavallo, M. Müller, and K. Binder. Unmixing of polymer blends confined in ultrathin films: Crossover between two-dimensional and three-dimensional behavior. *J. Phys. Chem. B*, 109:6544, 2005.

[75] Junfang Zhang and B. D. Todd. Pressure tensor and heat flux vector for inhomogeneous nonequilibrium fluids under the influence of three-body forces. *Phys. Rev. E*, 69:031111, 2004.

[76] B. Schnell, J. Baschnagel, H. Meyer, C. Fond, and J.P. Wittmer. Simulated glass-forming polymer melts: Glass transition temperature and elastic constants of the glassy state. *Eur. Phys. J. E*, 2011. accepted.

[77] D. Chandler. *Introduction to Modern Statistical Mechanics*. Oxford University Press, New York, 1987.

[78] J. S. Rowlinson. *Liquids and liquid mixtures*. Butterworths Scientific Publications, London, 1959.

[79] M. Doi and S. F. Edwards. *The Theory of Polymer Dynamics*. Clarendon Press, Oxford, 1986.

[80] J. Rudnick and G. Gaspari. *J. Phys. A*, 19:L191, 1986.

[81] J. A. Aronovitz and D. R. Nelson. *J. Phys. (Paris)*, 47:1445–1456, 1986.

[82] J.S. Higgins and H.C. Benoît. *Polymers and Neutron Scattering*. Oxford University Press, Oxford, 1996.

[83] B.B. Mandelbrot. *The Fractal Geometry of Nature*. W.H. Freeman, San Francisco, California, 1982.

[84] H. D. Bale and P. W. Schmidt. Small-angle x-ray-scattering investigation of submicroscopic porosity with fractal properties. *Phys. Rev. Lett.*, 53:596, 1984.

[85] P. Z. Wong and A. J. Bray. Porod scattering from fractal surfaces. *Phys. Rev. Lett.*, 60:1344, 1988.

[86] Milton Abramowitz and Irene A. Stegun. *Handbook of Mathematical Functions*. Dover, New York, 1964.

[87] K. Binder. Phase transitions in polymer blends and block copolymer melts: Some recent developments. *Adv. Polym. Sci.*, 112:181, 1994.

[88] D.C. Morse and J.K. Chung. On the chain length dependence of local correlations in polymer melts and a perturbation theory of symmetric polymer blends. *J. Chem. Phys.*, 130:224901, 2009.

[89] F. Brochard and P.-G. de Gennes. Conformation of molten polymers inside small pores. *J. de Phys. Lett.*, 40:L399, 1979.

[90] E.S. Nikomarov and S.P. Obukhov. Extended description of a solution of linear polymers based on a polymer-magnet analogy. *Sov. Phys. JETP*, 53:328–335, 1981.

[91] B. Duplantier. Exact contact critical exponents of a self-avoiding polymer chain in two dimensions. *Phys. Rev. B*, 35:5290–5293, 1987.

[92] N.K. Lee, J. Farago, H. Meyer, J.P. Wittmer, J. Baschnagel, S.P. Obukhov, and A. Johner. Non-ideality of polymer melts confined to nanotubes. *EPL*, 96:48002, 2011.

[93] E. Eisenriegler. *Polymers near surfaces*. World Scientific, Singapore, 1993.

[94] J. L. Jacobsen, N. Read, and H. Saleur. Dense loops, supersymmetry, and goldstone phases in two dimensions. *Phys. Rev. Lett.*, 90:090601, 2003.

[95] Y. Ikhlef, J.L. Jacobsen, and H. Saleur. Non-intersection exponents of fully packed trails on the square lattice. *J. Stat. Mech. - Theory and Experiment*, 05:P05005, 2007.

[96] A. Cavallo, M. Müller, J. P. Wittmer, A. Johner, and K. Binder. Single chain structure in thin polymer films: corrections to Flory's and Silberberg's hypotheses. *J. Phys.: Condens. Matter*, 17:S1697–S1709, 2005.

[97] H. Meyer, T. Kreer, A. Cavallo, J. P. Wittmer, and J. Baschnagel. On the dynamics and disentanglement in thin and two-dimensional polymer films. *Eur. Phys. J. Special Topics*, 141:167, 2007.

[98] We have checked whether the numerical problem disappears if instead of the harmonic bonding potential the original FENE bonding potential[60,61] is used in the dilute limit. We remind that the FENE bonding potential is strongly anharmonic (which improves the ergodicity if the thermostat is weak) and much flatter around its energy minimum. Perhaps for these reasons using the FENE potential the pressure appears to converge more rapidly with decreasing δt to $\beta P = \rho/N$, however, the standard choice $\delta t = 0.01$ yields still incorrect values.

[99] N. Schulmann, H. Xu, H. Meyer, P. Polińska, H. Meyer, J. Baschnagel, and J. .P. Wittmer. Strictly two-dimensional self-avoiding walks: Thermodynamic properties revisited. *J. Chem. Phys.*, 2013. in preparation.

[100] J. des Cloizeaux and G. Jannink. *Polymers in Solution : their Modelling and Structure*. Clarendon Press, Oxford, 1990.

[101] R. Everaers, I. Graham, and M. Zuckermann. End-to-end distance distributions and asymptotic behaviour of self-avoiding walks in two and three dimensions. *J. Phys. A*, 28:1271–1288, 1995.

[102] L. Schäfer and K. Elsner. Calculation of the persistence length of a flexible polymer chain with short-range self-repulsion. *Eur. Phys. J. E*, 13:225–237, 2004.

[103] N. Schulmann, H. Meyer, J. Baschnagel, A. Johner, and J. .P. Wittmer. Strictly two-dimensional self-avoiding walks: Dilute limit revisited. *Polymer Science Series C*, 2013. in preparation.

[104] M. Bishop and C. J. Satiel. *J. Chem. Phys.*, 85:6728–6731, 1986.

[105] B. Maier and J. O. Rädler. *Macromolecules*, 34:5723, 2001.

[106] The scaling relation Eq. (3.25) between the intrachain size distribution and the interchain pair correlation function is also of relevance, e.g., for semidilute polymer solutions in $d = 3$ dimensions.[123] A difference is here, however, that for $d = 3$ only the dilute limit and distances $r \ll \xi$ probing the structure within the blob are characterized by a critical exponent θ_2, while for $r \gg \xi$ the intrachain and related interchain correlations are perturbative ($\theta_2 = 0$), i.e. correspond to analytic deviations with respect to the Gaussian chain model.[33]

[107] The fraction of blobs on the perimeter of the compact chains can be computed directly by partitioning the chains in curvilinear subchains of length $g \approx 1/\rho^2$ and counting the number of subchains with at least one monomer in contact with a monomer from another chain. This fraction is found to decay as $(N/g)^{-3/8}$ (not shown).

[108] A. Yethiraj, B. J. Sung, and F. Lado. Integral equation theory for two-dimensional polymer melts. *J. Chem. Phys.*, 122:094910, 2005.

[109] J. P. Wittmer, W. Paul, and K. Binder. Rouse and reptation dynamics at finite temperatures: A Monte Carlo simulation. *Macromolecules*, 25:7211–7216, 1992.

[110] N. Schulmann, H. Meyer, T. Charitat, and J. .P. Wittmer. Strictly two-dimensional self-avoiding walks: Persistence length effects in dense solutions. 2013. in preparation.

[111] Technical webpage of Kimberly Clarck: http://www.kcpreducetoday.com/uk/products/featured-products.

[112] J.L. Jones and C.M. Marques. Rigid polymer network models. *J. Phys. France*, 51(11):1113–1127, 1990.

[113] M. Baudequin, G. Ryschenkow, and S. Roux. Non-linear elastic behaviour of light fibrous materials. *European Physical Journal B*, 12:157–162, 1999.

[114] C. M. van Wyk. *Text. Inst.,*, 37:T285, 1946.

[115] A Kabla and L Mahadevan. Nonlinear mechanics of soft fibrous networks. *Journal of The Royal Society Interface*, 4(12):99–106, 2007.

[116] L. D. Landau and E. M. Lifshitz. *Theory of Elasticity.* Pergamon Press, New York, 1981.

[117] P. Beckrich, G. Weick, C.M. Marques, and T. Charitat. Compression modulus of macroscopic fiber bundles. *Europhysics Letters*, 64:647–653, 2003.

[118] W. Helfrich. Steric interaction of fluid membranes in multilayer systems. *Zeitschrift für Naturforschung*, 33:305–315, 1978.

[119] W. Helfrich and W. Harbich. Adhesion and cohesion of tubular vesicles. *Chem. Scr.*, 25:32:36, 1985.

[120] J.V. Selinger and R.F. Bruinsma. Hexagonal and nematic phases of chains. *Physics Review Letters*, 43:2910–2921, 1991.

[121] H.P. Deutsch and K. Binder. The mean field to Ising crossover in the critical behavior of polymer mixtures: a finite size scaling analysis of Monte Carlo simulations. *J. Phys. II France*, 3:1049, 1993.

[122] H.-P. Hsu, W. Nadler, and P. Grassberger. *Macromolecules*, 37:4658, 2004.

[123] M. Müller, K. Binder, and L. Schäfer. Intra- and interchain correlations in semidilute polymer solutions: Monte Carlo simulations and renormalization group results. *Macromolecules*, 33:4568, 2000.

Appendix A : Implementation of spontaneous curvature for rigid chains

In our model chain stiffness is modeled by an angular potential $\mathcal{H}_{ang} = k_\theta(\theta - \theta_0)^2$ and the spontaneous curvature of the chains is implemented by the ensemble of the reference angles $\{\theta_{0,i}\}$. It is important to note that the 2D projection of the 3D torsional degree of freedom (usually taken into account through the angle ϕ) yields two possible values for one value of θ and it is necessary to differentiate 'left handed' and 'right handed' angles. Hence, when comparing the values of the reference and actual angles in the 2D case, the usual calculation of θ using the cosine function may lead to ambiguity. In order to calculate the angles in a single valued manner we implemented in the C++ LAMMPS code a combined calculation based on both cosine and sinus functions as shown in the code below. Our modifications are indicated by emphasized font.

```
double AngleHarmonic::single(int type, int i1, int i2, int i3)


  double **x = atom->x;


  double delx1 = x[i1][0] - x[i2][0];
  double dely1 = x[i1][1] - x[i2][1];
  double delz1 = x[i1][2] - x[i2][2];
  domain->minimum_image(delx1,dely1,delz1);
  double r1 = sqrt(delx1*delx1 + dely1*dely1 + delz1*delz1);



  double delx2 = x[i3][0] - x[i2][0];
  double dely2 = x[i3][1] - x[i2][1];
  double delz2 = x[i3][2] - x[i2][2];
  domain->minimum_image(delx2,dely2,delz2);
  double r2 = sqrt(delx2*delx2 + dely2*dely2 + delz2*delz2);



  double tk;
  double dtheta;
```

```
double c = delx1*delx2 + dely1*dely2 + delz1*delz2;
c /= r1*r2;
if (c > 1.0) c = 1.0;
if (c < -1.0) c = -1.0;



double s = delx1*dely2-delx2*dely1;
s /= r1*r2;
if (s > 1.0) s = 1.0;
if (s < -1.0) s = -1.0;
s = 1.0/s;

if (s>0)
     dtheta = acos(c)- theta0[type];
else
     dtheta = -acos(c)+2*PI- theta0[type];



tk = k[type] * dtheta;
return tk*dtheta;
```

Appendix B : Spontaneous curvature distributions

In our simulations, thermalized semiflexible polymers are always supposed to have a linear ground state while athermal fibers present different shape distributions. For every disorder class we chose a base and a typical amplitude distribution for the different modes. The ground state shape of a specific chain was then designed by fixing the modes and the amplitudes using the appropriate distribution and by superposing the different modes. (Reference angles were then fixed supposing equidistant monomers distances.)

The following Fortran90 code illustrates the implementation of several disorder types:

```
!%%%%%%%%%%%%%%%%%%%%%%%%%%%%%%%%%%%%%%%%%%%%%%%%%%%%%%%%%%%%%%%%%%%%%%%%%%%%%%%%%%%
!                   Determination of modes and amplitudes
!%%%%%%%%%%%%%%%%%%%%%%%%%%%%%%%%%%%%%%%%%%%%%%%%%%%%%%%%%%%%%%%%%%%%%%%%%%%%%%%%%%%
         select case (disorder_type)

                  case ("lines")
                           nrq(iM)=1
                           q(1)=0
                           A(1)=0

                  case ("one_mode")
                           nrq(iM)=1
                           mysign=-mysign
                           q(1)=alfa*qmin*mysign
                           A(1)=Aq0

                  case ("one_mode_qdis")
                           nrq(iM)=1
                           do iq=1,nrq(iM)
                                    mysign=-mysign
                                    qmean=mysign*alfa*qmin
                                    sigma=beta*alfa*qmin
                                    call gauss_rand(qmean,sigma,q(iq))
                                    A(iq)=Aq0
                           end do

                  case ("alpha")
                           nrq(iM)=N
                           do iq=1,nrq(iM)
                                    q(iq)=qmin+(iq-1)*(qmax-qmin)/(real(N)-1)
                                    sigma=Aq0*(KbT/k/N)**0.5/(q(iq))**(alfa/2)
                                    mu=0.
                                    call gauss_rand(mu,sigma,A(iq))
                           end do

                   case ("alpha2")
```

```
                           nrq(iM)=N
                           do iq=1,nrq(iM)
                                    mysign=-mysign
                                    call scaled_rand(qmin,qmax,q(iq))
                                    A(iq)=mysign*Aq0*(KbT/k/N)**0.5/(q(iq))**(alfa/2)
                           end do

                 case ("alpha_few_modes")
                           nrq(iM)=beta
                           do iq=1,nrq(iM)
                                    q(iq)=qmin*iq
                                    sigma=Aq0*(KbT/k/N)**0.5/(q(iq))**(alfa/2)
                                    mu=0.
                                    call gauss_rand(mu,sigma,A(iq))
                           end do

                  case default
                           write(*,*) "please specify disorder type. "

         end select


!%%%%%%%%%%%%%%%%%%%%%%%%%%%%%%%%%%%%%%%%%%%%%%%%%%%%%%%%%%%%%%%%%%%%%%%%%%%%%%%%%%
!                      Mode superposition -> function F
!%%%%%%%%%%%%%%%%%%%%%%%%%%%%%%%%%%%%%%%%%%%%%%%%%%%%%%%%%%%%%%%%%%%%%%%%%%%%%%%%%%

F=0
select case (base_type)

         case ("sin_sum")
                  do iq=1,nrq(iM)
                           F=F+A(iq)*sin(q(iq)*x1+fi)!(2*Pi*q(iq)*x/L)
                  end do

         case ("eigen_sum")
                  do iq=1,nrq(iM)
                           al=q(iq)*N
                           b=al*x1/N
                           ea=exp(-al)
                           eb=exp(-b)
                           e2a=ea*ea
                           eba=exp(b-al)
                           fq=eba*(ea+sin(al)-cos(al))/(1-e2a-2*sin(al)*ea)
                           fq=fq+0.5*(1+e2a-2*cos(al)*ea)/(1-e2a-2*sin(al)*ea)
                              *(-eb+2*sin(b))
                           fq=fq-0.5*(eb+2*cos(b))
                           F=F+A(iq)*fq
                  end do

end select
```

Nava SCHULMANN

TITRE de la thèse

Résumé

Cette thèse de doctorat est consacrée à l'étude analytique et numérique de systèmes de polymères et de fibres à deux dimensions. Des systèmes de polymères confinés en films ultra-minces présentent un très grand intérêt technologique et expérimentale et posent de nombreux défis théoriques en raison de leur fort comportement non-champ moyen qui se manifeste par divers exposants critiques non triviaux. Nous nous concentrons sur la limite strictement 2D où le croisement des chaînes est interdit et nous étudions, en fonction de la densité et de la rigidité des chaînes, les propriétés élastiques et conformationnelles de trois classes de systèmes: polymères flexibles et semi-flexibles à température finie et polymères macroscopiques athermiques (fibres) à courbure spontanée imposée. Pour les polymères flexibles, il est démontré que bien que les polymères auto-évitants denses adoptent des configurations compactes avec un exposant de Flory $\nu = 1/2$, ils ne se comportent pas comme des chaînes gaussiennes. En particulier un exposant de contact non-nul $\theta 2 = 3/4$ implique une dimension fractale de périmètre $d_p = 5/4$. Par conséquence, en accord avec la loi généralisée de Porod, le facteur de structure intramoléculaire $F(q)$ révèle un comportement non-gaussien et la température de démixion des mélanges de polymères 2D devrait être réduite. Nous étudions également les effets de la rigidité des chaînes sur les systèmes de polymères à 2D et constatons que le comportement universel n'est pas modifié lorsque la longueur de persistance est beaucoup plus petite que la longueur de confinement. La nature de la transition de phase nématique à haute rigidité, qui est dans le cas 2D l'objet d'un débat de longue date, est également explorée. Des résultats préliminaires semblent indiquer une transition du premier ordre. Enfin, motivés par un travail théorique récent sur les modules élastiques de faisceaux de fibres, nous étudions les effets de la courbure spontanée sur l'élasticité d'ensembles de fibres. Nous montrons que en jouant sur le désordre des amplitudes des modes de Fourier de l'état fondamental il est possible de régler le module de compression, en accord qualitatif avec la théorie.

Mots clés: Physique Statistique, Physique des Polymères, dynamiques, Fibres, élasticité non-linéaire

Résumé en anglais

This PhD thesis is devoted to a theoretical study of polymer and 'polymer like' systems in strictly two dimensions. Polymer systems in reduced dimensions are of high experimental and technological interest and present theoretical challenges due to their strong non-mean-field-like behavior manifested by various non-trivial universal power law exponents. We focus on the strictly 2D limit where chain crossing is forbidden and study as function of density and of chain rigidity conformational and elastic properties of three system classes: flexible and semiflexible polymers at finite temperature and macroscopic athermal polymers (fibers) with imposed quenched curvature. For flexible polymers it is shown that although dense self-avoiding polymers are segregated with Flory exponent $\nu = 1/2$, they do not behave as Gaussian chains. In particular a non-zero contact exponent $\theta 2 = 3/4$ implies a fractal perimeter dimension of $d_p = 5/4$. As a consequence and in agreement with the generalized Porod law, the intramolecular structure factor $F(q)$ reveals a non-Gaussian behavior and the demixing temperature of 2D polymer blends is expected to be reduced. We also investigate the effects of chain rigidity on 2D polymer systems and found that universal behavior is not changed when the persistence length is not too large compared to the semidilute blob size. The nature of the nematic phase transition at higher rigidities, which is in the 2D case the subject of a long standing debate, is also briefly explored. Preliminary results seem to indicate a first order transition. Finally, motivated by recent theoretical work on elastic moduli of fiber bundles, we study the effects of spontaneous curvature at zero temperature. We show that by playing on the disorder of the Fourier mode amplitudes of the ground state, it is possible to tune the compression modulus, in qualitative agreement with theory.

Key words: Statistical Mechanic, Polymer physic, dynamics, Fibers, non-linear elasticity